Distribution Agreement

In presenting this thesis or dissertation as a partial fulfillment of the requirements for an advanced degree from Emory University, I hereby grant to Emory University and its agents the non-exclusive license to archive, make accessible, and display my thesis or dissertation in whole or in part in all forms of media, now or hereafter known, including display on the world wide web. I understand that I may select some access restrictions as part of the online submission of this thesis or dissertation. I retain all ownership rights to the copyright of the thesis or dissertation. I also retain the right to use in future works (such as articles or books) all or part of this thesis or dissertation.

Signature:

_____ _____

Guanxiong Chen Date

Non-equilibrium states of current-driven phonons and frustrated magnetic systems at nanoscale

By

Guanxiong Chen
Doctor of Philosophy

Department of Physics

Sergei Urazhdin, Ph.D.
Advisor

Ajit Srivastava, Ph.D.
Committee Member

Daniel Weissman, Ph.D.
Committee Member

Hayk Harutyunyan, Ph.D.
Committee Member

Sidong Lei, Ph.D.
Committee Member

Accepted:

Kimberly Jacob Arriola, Ph.D.
Dean of the James T. Laney School of Graduate Studies

Date

Non-equilibrium states of current-driven phonons and frustrated magnetic systems at nanoscale

By

Guanxiong Chen
B.S., Nankai Unversity, Tianjin, 2016

Advisor: Sergei Urazhdin, Ph.D.

An abstract of
A dissertation submitted to the Faculty of the
James T. Laney School of Graduate Studies of Emory University
in partial fulfillment of the requirements for the degree of
Doctor of Philosophy
in Department of Physics
2021

Abstract

This dissertation includes a variety of research projects focusing on nonequilibrium phenomena at the nanoscale. To be specific, two main systems are investigated. The first one is the highly nonthermal phonon system in current driven nanostructures. Our research demonstrates that at cryogenic temperature the current-driven phonon distribution in a variety of metallic microstructures is qualitatively different from that expected for Joule heating, as manifested by a weakly-singular linear dependence of resistance on current. In other words, the phonons generated by electron scattering events are far from equilibrium and may not be adequately described by a temperature as implied by the Joule's heating law. Our result suggests the possibility of further optimum of thermal dissipation in nanodevices beyond the limits set by the Joule heating law. As a follow up, we perform nonlocal electronic measurements utilizing an electrically biased metallic nanowire as a phonon source, and a separate nanowire serving as the phonon detector, to investigate the thermalization process of the nonequilibrium phonons. Analysis of the dependence on the thickness of the spacer separating the nanowires shows that these non-equilibrium phonons relax via strongly anharmonic processes that cannot be described in terms of the usual few-phonon scattering. Our findings provide insight into the mechanisms of current-driven phonon generation, transport, and relaxation at nanoscale in a vertically stacked device, which will likely facilitate new approaches to efficient Joule heat dissipation in 3D integrated circuits (IC).

The second system is ferromagnet /antiferromagnet (F/AF) structure experiencing random interfacial coupling. Here, we utilize magnetoelectronic measurements to analyze the effective exchange fields at permalloy/CoO interface. Our results cannot be explained in terms of quasi-uniform effective exchange fields but are in agreement with the random-field hypothesis of Malozemoff[Phys. Rev. B 35, 3679 (1987)]. The approach developed here also opens a new route for the quantitative analysis of effective exchange fields and anisotropies in magnetic heterostructures for memory, sensing and computing applications. For example, we demonstrate that ideal memristors—devices whose resistance is proportional to the charge that flows through them—can be realized using spin torque-driven viscous magnetization dynamics. The latter can be accomplished in the spin liquid state of thin-film F/AF heterostructures with frustrated exchange, where the memristive response is tunable by proximity to the glass transition, while current-induced Joule heating facilitates non-volatile operation and second-order memristive functionality beneficial for neuromorphic applications.

Non-equilibrium states of current-driven phonons and frustrated magnetic systems at nanoscale

By

Guanxiong Chen
B.S., Nankai Unversity, Tianjin, 2016

Advisor: Sergei Urazhdin, Ph.D.

A dissertation submitted to the Faculty of the
James T. Laney School of Graduate Studies of Emory University
in partial fulfillment of the requirements for the degree of
Doctor of Philosophy
in Department of Physics
2021

Acknowledgments

First of all, I would like to thank my advisor Dr. Sergei Urazhdin for great mentoring and supporting during my graduate research. He is always enthusiastic and willing to help. Without his stimulation and insightful guidance, I wouldn't be able to overcome the academic challenges in my graduate program. Also I would like to thank all my committee members Dr. Hayk Harutyunyan, Dr. Ajit Srivastava, Dr. Sidong Lei and Dr. Daniel Weissman for their valuable advice for both research and career planning during my time of PhD.

With wonderful time doing research in Sergei's lab, I would like to thank all lab members for their help and guidance. I would like to thank Dr. Rongxing Cao, Dr. Andrei Zholud and Dr. Ryan Freeman for their warm welcome, patient training of experiment technique and helpful brain storm in journal club. I remember in my first two years in the lab, I was overwhelmed by the technical terms and it was hard for me to follow the discussion in group meeting. Luckily, Ryan and Andrei can always notice I am puzzled and call out for a pause. Their schematic cartoons for physical process in our group meetings were really helpful for the beginning of my research career.

I woudld also like to acknowledge the help from Dr. Xin Lu, Dr. Sudipta Dubey, Dr Manoj Manjare, Dr. Feng Wang, Dr. Robert Lemasters, Dr. Guoce Yang, Chentao Li and Weijie Li in Dr. Hayk Harutyunyan and Dr. Ajit Srivastava's lab. Since we share the lab for nano fabrication and material growth, we are kind of "semi-lab mates". I really enjoy the time when we help and support each other in the experiment. My PhD would have been impossible without the influence of all of these people, and the others that I've ashamedly forgotten to acknowledge here.

Contents

List of Figures

Chapter 1

Introduction

This thesis focuses on several seemingly disparate topics: i) studies of generation of nonequilibrium phonon generation by electric current in nanostructures described in chapter 2, ii) studies of propagation and relaxation mechanisms of high energy phonons described in chapter 3, iii) studies of frustrated magnetism in thin-film ferromagnet/antiferromagnet bilayers described in chapter 4, and iv) demonstration of the possibility to achieve ideal memristive functionality using viscous magnetization dynamics in magnetically frustrated nanostructures based on ferromagnet/antiferromagnet bilayers, in chapter 5. Despite significant differences among materials and phenomena studied in this work, all of these studies are united by the overarching theme of non-equilibrium phenomena at nanoscale that transcend the conventional concepts developed in the studies of weakly perturbed or equilibrium systems at macroscales. The underlying idea is that at nanoscale, matter can be strongly perturbed without beyond damaged or irreversibly changed. The outcome of the studies of such strong perturbed systems is a unique insight into the interactions that stabilize (or destabilize) dynamical and static states of matter, and the approaches to controlling them. In our studies of current-generated phonons at nanoscale, we have found that large current densities easily achievable at nanoscale

but not in macroscopic systems result in a highly non-equilibrium phonon distribution, qualitatively different from the usual expectations from the Joule heating. This has provided microscopic insight into electron-phonon scattering. By analyzing the propagation and relaxation of these phonons in nanostructures, we determined that the phonon relaxation mechanism is qualitatively different from the usually expected few-phonon scattering, but rather is a non-perturbative process that cannot be described with existing theories of phonon relaxation. Our studies of thin-film ferromagnet/antiferromagnet bilayer benefited from the possibility to produce, at nanoscale, astronomically large effective magnetic fields of the order of 1000 Tesla (the largest magnetic fields achieved at the High Magnetic Field Lab in Tallahassee, FL is about 100 Tesla for a fraction of a second). These huge effective fields were produced possible by the Heisenberg exchange interaction across the interface between two thin magnetic films, which allowed us to analyze the resulting large changes in the magnetic properties of these materials, and explore the possible applications for these changes. In particular, we showed that the viscous magnetization dynamics stemming from the hierarchical energy landscape produced by magnetic frustration in ferromagnet/antiferromagnet bilayers can be utilized to develop an ideal memristor – a nanodevice particular useful for artificial neuromorphic systems. The next Section provides the background on different material systems we utilized in our studies, the relevant phenomena, and the approaches used in the studies.

1.1 Phonon and lattice vibration

Since the following two chapters will be about the observation and detection of highly nonequilibrium phonon system in current driven nano-devices, it would be useful to first review the background knowledge of lattice vibration and phonon. From the view of classical mechanics, the lattice vibration can be approximated as a "small"

vibration problem. The word "small" indicates that during the vibration, the atom only slightly deviates from its equilibrium position and the restoring force(energy) can be expressed as an series expansion around the energy minimum position. However, it is worthy to note that the idea of series expansion is not always applicable. For instance, highly nonlinear potential widely exists in nature, where due to the existence of bistable states, the series expansion won't converge. We would return to the discussion of the role of highly nonlinear potential in phonon relaxation process in the chapter about "Transport and relaxation of current-generated nonequilibrium phonons from nonlocal electronic measurements".

Assuming that there are N atoms in the crystal and their equilibrium positions are $\overrightarrow{R_n}$. When the atoms deviates from their equilibrium position by $\overrightarrow{\mu_n(t)}$, the atom position can be expressed as $\overrightarrow{R_n} + \overrightarrow{\mu_n(t)}$. In this case, since for N atoms, there are 3N components for their displacement and the potential energy of the system can be expanded as:

$$V = V_0 + \sum_{i=1}^{3N} (\frac{\partial V}{\partial \mu_i})_0 * \mu_i + \frac{1}{2} \sum_{i,j=1}^{3N} \frac{(\partial^2 V)}{\partial \mu_i \partial \mu_j} \mu_i \mu_j + ... \tag{1.1}$$

Since we are expanding around equilibrium position, $(\frac{\partial V}{\partial \mu_i})_0 = 0$. Setting $V_0 = 0$, the potential of the restoring force of the system can be written as $\frac{1}{2} \sum_{i,j=1}^{3N} \frac{(\partial^2 V)}{\partial \mu_i \partial \mu_j} \mu_i \mu_j$. Here, the harmonic approximation is used, i.e., the potential is only expanded to quadratic term. In this case, there is no interaction between the normal modes (phonons). It is worthy to stress here that in some cases, the harmonic approximation is not enough to explain the observation and higher order term need to be included. For example, in the problem of heat transfer in crystal. The form of diffusive heat transport $j = -\kappa \frac{dT}{dx}$, indicates the heat transfer, instead of free propagation of lattice vibration (phonons), is similar to the form of heat transfer in gas, where the energy transfer is mediated by the collision between gas molecules. In this case, the

mechanism behind diffusive heat transfer is the interaction between phonons, which redistributes phonon energy, so higher order terms, which descries phonon scattering events, much be included to provide a microscopic explanation for the diffusive heat transfer in crystal.

Back to the harmonic approximation, the kinetic energy of the N atom system is

$$T = \frac{1}{2}\sum_{i=1}^{3N} m\dot{\mu_i}^2 \tag{1.2}$$

As usually done in classical mechanics [11], we can use normal coordinates to avoid the cross term like $\mu_i\mu_j$ in the energy term. The normal coordinates are connected with the original coordinates by $\sqrt{m}\mu_i = \sum_{i=1}^{3N} a_{ij}Q_i$. By using the proper normal coordinates the V and T can be expressed as $T = \frac{1}{2}\sum_{i=1}^{3N} m\dot{Q_i}^2$ and $V = \frac{1}{2}\sum_{i=1}^{3N} {\omega_i}^2{Q_i}^2$. In this case, the Lagrangian L=T-V and the normal momentum is $p_i = \frac{\partial L}{\partial \dot{Q_i}}$. Ftom the normal equation, the vibration can be characterized with

$$\ddot{Q_i} + {\omega_i}^2 Q_i = 0,\ i = 1, 2, ...3N \tag{1.3}$$

Since in the normal coordinate system, these variables are independent, the solution is $Q_i = Asin(\omega_i t + \delta)$. Since the oscillation of Q is related to the real oscillation of atoms via the normal transformation. For one the oscillation of Q_j, it means an collective oscillation mode of the whole system ($mu_i = \frac{a_{ij}}{\sqrt{m_i}} Asin(\omega_j t + \delta)$). As demonstrated above, the key to solve the harmonic oscillation of lattice is to find the correct orthogonal transformation (the normal modes).

1.2 Phonon modes in 1D spring chain

The simplest model of lattice vibration is a 1D spring chain [12]. In this system, objects with the same mass (m) are connected by identical springs with spring constant

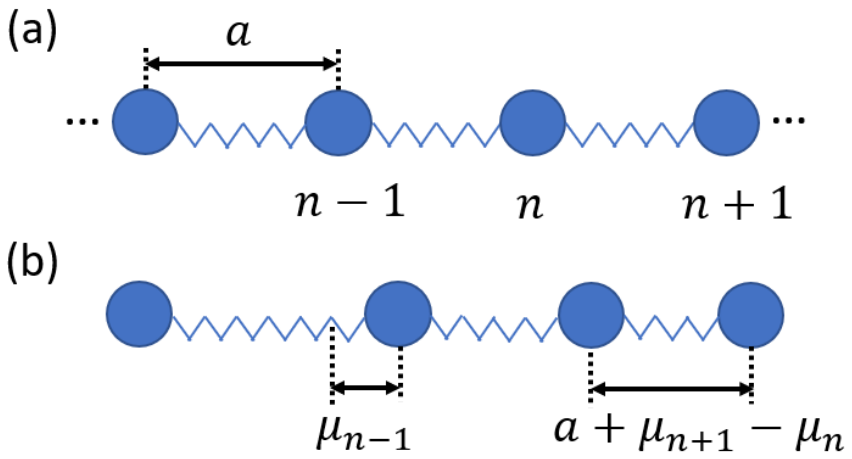

Figure 1.1: Schematic plot of the 1D spring chain

(β) [Fig. 1.1(a)]. When there is a displacement of one oscillator around position a as shown in Fig. 1.1(b), its potential can be expressed as $v(\delta) = \frac{1}{2}\beta * \delta^2$, so the restoring force is $F = -\frac{\partial V}{\partial \delta} = -\beta\delta$. Since the system is relatively simple, here we can just solve it by writing Newton's equation of the chain and "guess" a trial solution, which is equivalent to the general method based on using orthogonal transformation discussed in the last section. For the equation of motion of the n th atom in the chain, it only interacts with its two neighbors n-1 and n+1. The relevant displacement of the n-1 atom is $\delta = \mu_n - \mu_{n-1}$, so the forced exerted on the nth atom is $-\beta(\nu_n - \mu_{n-1})$. For the n+1 atom on its right hand side, the relative displacement is $\delta = \mu_n - \mu_{n-1}$ and the force exerted on the n th atom is $-\beta(\mu_{n+1} - \mu_n)$. Combining the forces together, the equation of motion of the n th atom can be expressed as:

$$m\ddot{\mu_n} = \beta(\mu_{n+1} - \mu_n) - \beta(\mu_n - \mu_{n-1}) \tag{1.4}$$

Since for every atom there is a similar equation of motion, there are N such equations. Thus, the dynamics of the 1D spring chain is determined by the N differential equations. With the help of numerical method, given the initial condition, which is the displacement and speed of each atom at t=0, even for a long chain ($N = 300$)

the dynamics of the system can be calculated pretty fast with computer. However, to provide further physical insight, it is worthy to solve it analytically.

1.3 Dispersion of 1D chain

Instead of using the method about orthogonal transformation mentioned in the last section, here we can "guess" the solution has the following form $\mu_{nq} = Ae^{i(\omega t - naq)}$ and ω, A, q are parameter. It is worthy to note that the since Eq. (1.4) is a linear homogeneous equation, a complex solution can be used. By importing the trial solution into the Eq. (1.4), the expression turns out to be

$$\omega^2 = \frac{2\beta}{m} sin^2(\frac{aq}{2}) \tag{1.5}$$

, which is independent on the position of the atom (n). Thus, $\mu_{nq} = Ae^{i(\omega t - naq)}$ is a solution of Eq. (1.4) once the condition in Eq. (1.5) is satisfied. Here, Eq. (1.5) describes the dispersion of wave in the spring chain. The main difference between q in Eq. (1.5) and the wave vector in a continuous medium is that changing q to $q + \frac{2\pi N}{a}$ (N is integer), doesn't influence the oscillation of any atom in the chain. For simplicity, q is usually limited in $-\pi/a < q < \pi/a$, which is named the Brillouin zone of the chain and q value out of the Brillouin zone can't provide any new oscillation mode.

Since the Eq. (1.4) is only applicable to the atoms with two neighbors, which is not applicable to the two atoms at the end of the chain. One possible solution is to specially write Newton's equation for the terminal atoms. However, it would both break the periodic symmetry of the chain and will lead to wave reflection at the end. Another method is to connect the two ends of the 1D chain and make the system a loop, so the wave could keep propagating without reflection. It is called periodic boundary condition, which is widely used in numerical simulation of physical systems

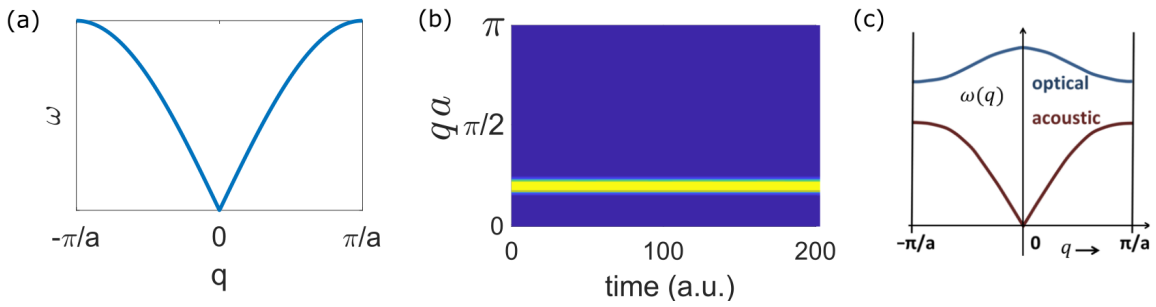

Figure 1.2: (a) The dispersion of 1D spring chain with identical mass (b) The propagation of wave packet in 1D spring chain in wave vector space. (c) Phonon dispersion of a 1D spring chain with alternating mass. Figure recreated from Wikipedia.

when we want to avoid extra complexity at "real physical boundary". With such periodic boundary condition, it means that for a chain with length N, when the index of atom increase by N, the oscillation $\mu_{nq} = Ae^{i(\omega t - naq)}$ should be the same, which means $e^{-iNaq} = 1$, i.e., q can only choose some discrete values. $(q = \frac{2\pi}{Na} * integer)$. As the range of q is $-\pi/a < q < \pi/a$, with step $\frac{2\pi}{Na}$, there are N oscillation modes available. Considering the degree of freedom of the 1D chain is also N, it indicates with $q = \frac{2\pi}{Na} * integer$, $\omega^2 = \frac{2\beta}{m} sin^2(\frac{aq}{2})$, the motion of the chain is fully characterized by $\mu_{nq} = Ae^{i(\omega t - naq)}$.

Here we plot the dispersion of the 1D chain. As shown in Figure 1.2(a), the dispersion is nonlinear. Here a solid line is used, because for real crystal the atom number N is large and the the wave vector q is approximately continuous.

To give the reader an idea of the simulation of 1D chain that will be used in the following chapter, here we simply simulate the propagation of a wave packet in such 1D chain. The reason, why we would like to simulate a wave packet instead of a plane wave is that the wave packets is a spacially local object, making it visual for the study of scattering events. Moreover, as a wave packet has a finite width in Fourier space (since it is not monochromatic), compared with plane wave, which is a delta function in Fourier space, it is easier to be identified in Fourier analysis. For a chain with N=300, a wave packet is build by setting the initial condition of atom with

the product between a plane wave with wave length 10 and a Gaussian function with width 10. Here, the dispersion is used to determine ω, when initializing the system. As shown in Figure 1.2(b), in Fourier space, we can see that the wave packet keep propagating. By making the width of the wave packet wider (narrower), the wave in Fourier space can be narrower (wider).

Before ending this section, it is worthy to mention that our analysis need to be modified for crystal with multiple atoms in one unit cell. For these crystals, the simplest model is a 1D chain but with mass alternating between m_1 and m_2, in this case as shown in Figure 1.2(c), an extra phonon branch appears. In this case, the upper one is named optical modes, because its frequency is high and is accessible by infrared photons. The lower branch is called acoustic phonon. Generally speaking, optical modes represent the relative oscillation between atoms within one unit cell and the acoustic modes account for the collective oscillation of the unit cells.

1.4 How do phonons propagate: ballistically or diffusively?

As discussed in the previous section, due to the similarity between Fourier's heat transfer law in crystal and the heat transfer in gas, we conclude that heat transfers in crystal diffusively mediates by phonon scattering events, which exchange their energy like atoms in gas. However, with the advancement in nanofabrication and cryogenic technique, the size of electronic devices is approaching phonon mean free path (MFP), i.e., phonons, instead of scattering with each other to main a local quasi-equilibrium distribution (the Bose-Einstein distribution), freely propagates [13, 14, 15]. In this case, if we calculate the heat conductance via $q = -\kappa \nabla T$, the κ would varies with the sample size, which indicates the breakdown of diffusive heat transport. The ballistic heat transfer is of great significance in semiconductor process, since the non-diffusive

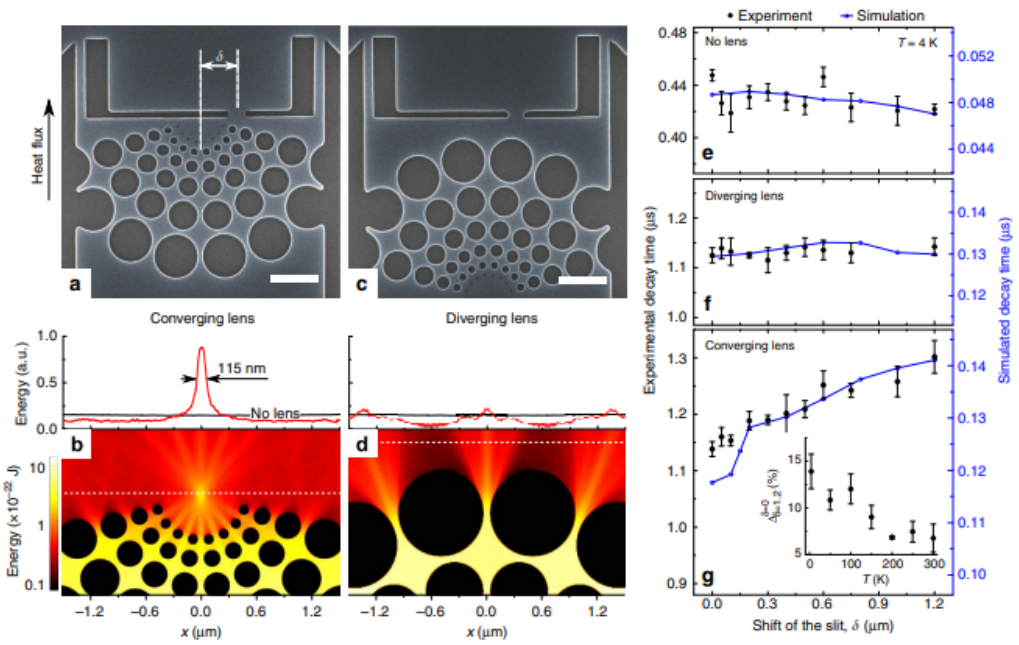

Figure 1.3: SEM image of the Al pad with converging (a) and diverging (c) lens. (b) (d) Heat distribution predicted by simulation. (e) (f) (g) The experimental and simulated decay time of the device measured with micro time-domain thermoreflectance [1].

heat transfer can lead to hot spots in devices, where the effective temperature is higher than prediction from diffusive model. Thus, ballistic phonon propagation is widely investigated and multiple theory frameworks, such as the Lattice Boltzmann Method (LBM), which directly solves the Boltzmann equation in a network of discrete points, have been developed [16, 17, 18].

The existence of ballistic phonon transport also provides, the opportunity to "guide" or even focus the heat flow [1], which is not possible in diffusive heat transfer region, where the energy transfer is dominated by random phonon scattering process. For material with long phonon MFP, there have been proof of principle experiments about heat focus and guiding. As shown in Figure 1.3, the heat (phonons) can be focus with a designed pattern on an Aluminum pad, which presages complete control over directionality of ballistic heat fluxes in nanostructures.

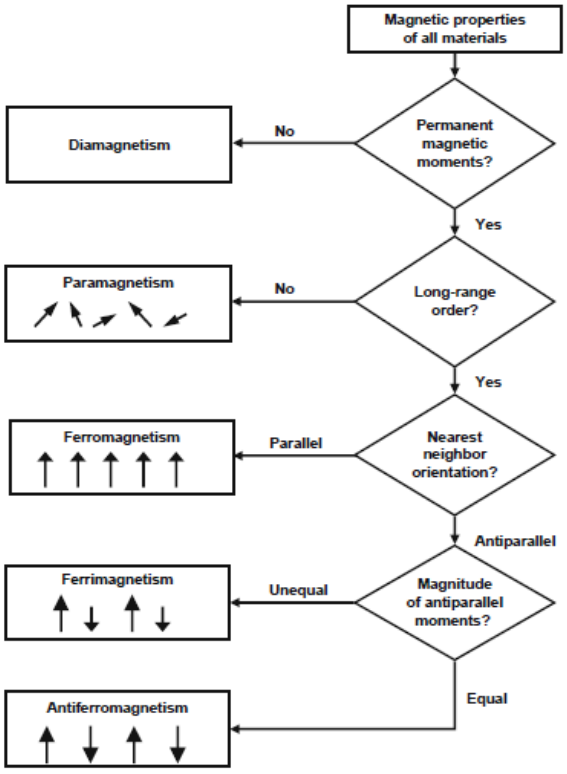

Figure 1.4: The classifications of magnetic materials. The anti-ferromagnetism can be viewed as a special case of ferrimagnetism. Table from [2].

1.5 Magnetic order of materials

For the previous sections, we focus on the basic knowledge of lattice vibration, which is relevant to the two chapters about the "Nonequilibrium phonon distribution in current-driven nano- and micro-structures " and "Propagation and relaxation of the highly nonequilibrium phonon". Since chapter 4 and 5 will be about the nonequilibrium (glassy) behavior of magnetization in ferromagnetic/antiferromagnetic hetero structure and its potential application in neuromorphic devices, it would be useful introduce some basic concepts about magnetic order in materials.

Depending on the magnetic order, material can be are classified as paramagnet, diamagnet, ferromagnet, ferrimagnet and antiferromagnet. Although these terminology may sound awkward, practically we simply need to answer a few questions to identify the magnetic order of an unknown material [2]. Before we proceed, it would

be convenient to introduce the idea of magnetic susceptibility, which is defined as

$$M = M_0 + \bar{\chi} H \tag{1.6}$$

Here M is the net magnetic moment per unit volume, also named magnetization. H is the external field and M_0 is the spontaneous magnetization (the magnetization when external field is zero). $\bar{\chi}$ is the magnetic susceptibility of magnetic material. Since both M and H are vectors, in the most general case $\bar{\chi}$ is a 3×3 matrix [19]. However, in many materials $\bar{\chi}$ is isotropic, so $\bar{\chi}$ can be considered as a scalar.

Then we can classify a material following the sequence shown in Figure 1.4. Materials with no permanent magnetic moments are called diamagnet and the direction of induced magnetization in a diamagnet is opposite to the direction of external field. A classical explanation for the existence of diamagnetism can be provided based on Lenz's Law. When external magnetic field is applied, due to Lenz's Law, the electronic orbital motions are modified to generate an opposite magnetic field, so the net increase of magnetic flux can be reduced. The diamagnetic response is pretty generic, however, due to its small magnitude in materials that contain permanent magnetic moments, its contribution is usually overshadowed by the permanent magnetic moments.

It is interesting to note that living biologics is usually a diamagnet. As show in the Figure 1.5, since a living frog is in diamagnetic state, it can be elevated by a strong magnetic field ($\sim 10T$), which is around 10^3 stronger than the field of a refrigerator magnet.

If a material has permanent magnetic moment and no long range order, its named a paramagnetic. For a paramagnet, when external field is zero, due to the random orientation of its magnetic moments, the net magnetization is zero. However, when external magnetic field is applied, the inner moments are aligned with the external

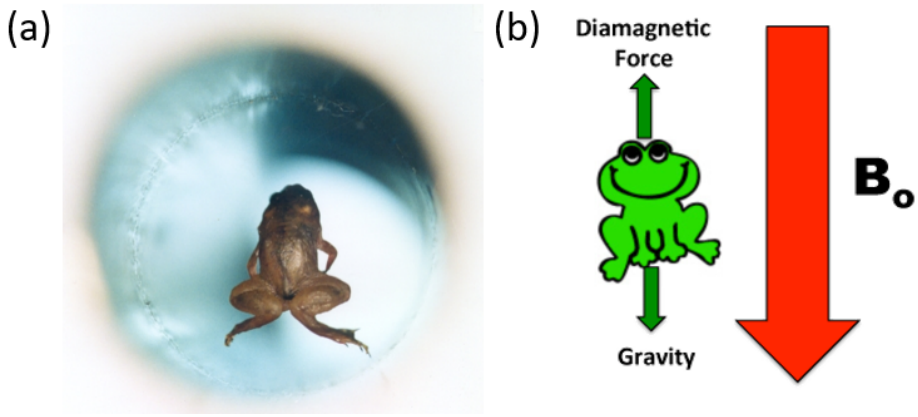

Figure 1.5: (a) The picture of a frog levitated by magnetic field (b) The gravity is canceled by the diamagnetic force in this experiment. (Pictures from https://mriquestions.com/how-to-levitate-a-frog.html)

field (H), manifesting themselves as a positive induced magnetization, i.e. $\chi > 0$.

The material with long range order and parallel nearest neighbor is ferromagnet. Due to the Heisenberg exchange, they can persist finie magnetization with zero external field. In daily life, when a material is called magnet, it is usually a ferromagnet. As it has a constant magnetization, which can be rotated by external field, ferromagnet has been the central part of magnetic storage technique and widely investigated by the society.

In some materials, some quantum mechanical coupling such as RKKY or super exchange, can lead to the anti-parallel configuration between nearest magnetic moments. If the magnetic moments of the nearest neighbors perfectly cancel each other, it is called antiferromagnet. For materials, where the anti-parallel magnetic moments doesn't perfectly cancel each other, they are classified as ferrimagnetic material.

Since in our research, ferromagnet is the key active material, we would briefly introduce the idea of magnetic texture, magnetic dynamics and magnetoelectronic measurement techniques about ferromagnetic material.

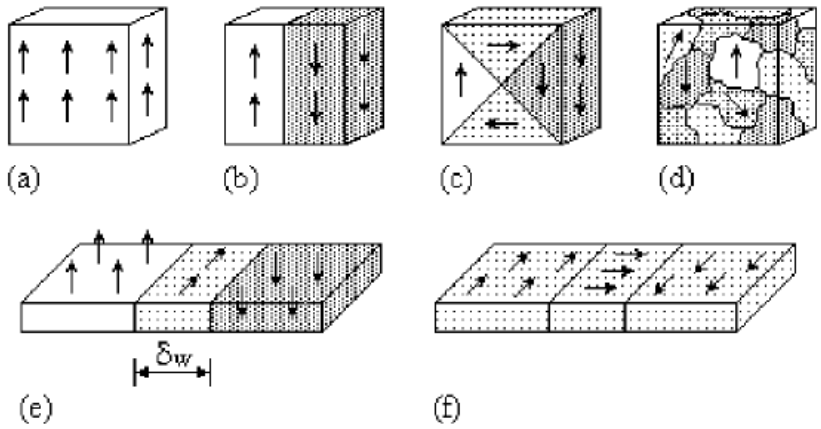

Figure 1.6: Micromagnetic spin configurations (a) single domain state (b)two domain state, usually appears in small particle with strong uniaxial anisotropy. (c) (d) Multidomain states (e) Bloch domain wall in thin film with strong perpendicular anisotropy (f) Neel domain wall in thin magnetic film with in-plane anisotropy. [3]

1.6 Magnetic texture in ferromagnetic material

In this section, we will focus on the distribution of magnetization in ferromagnet. The understanding of magnetic texture (domain) structure, is of great importance for practical application of ferromagnetic material. For example, in hard disk drive (HDD), data is stored as magnetic domains. Further understanding of the physics behind magnetic domains and their interactions could help us minimize the domain size and stabilize the domain structure, which could increase the storage density and life time. Some of the representative domain structures are shown in Figure 1.6 [3]. Within each domain, there is a large number of microscopic magnetic moments pointing along the same direction. The regions between adjacent domains are domain wall, where the magnetization rotates from one domain to another. In static state, the domain is the result of minimization of magnetic energy E,

$$E = \int \{A[\nabla(\frac{M}{M_s})]^2 - K_1\frac{(n\cdot M)^2}{(M_s)^2} - \mu_0 M\cdot H - \frac{\mu_0}{2}M\cdot H_d(M)\}dV \qquad (1.7)$$

n is the unit vector of the local anisotropy, H is the external field and H_d is the

demagnetizing filed, which originates from the magnetostatic self-interaction. The first term in Eq. (1.7) is the exchange interaction term. In ferromagnetic system such term favors the alignment of adjacent magnetization along the same direction. The second term represents a local uniaxial anisotropy. As a phenomenological expression, this term may have different physical origins, such as shape anisotropy or crystal anisotropy. The third term is the Zeeman energy of magnetic moment in external field. The last term is the self-interaction energy and $H_d = \frac{1}{4\pi} \int \frac{3(r-r')(r-r')\cdot M(r') - |r-r'|^2 M(r')}{|r-r'|^2} dV'$. The appearance of integration in the self energy is not surprising, since to calculate the self energy of dV, the field generated by the rest part of the ferromagnet needs to be summed up. Due to the complexity of double integration in Eq. (1.7) for self-interaction energy, when doing simple analysis the last term is usually omitted.

Then we would like to go trough the magnetic textures in Figure 1.6. In panel (a), it is a single domain state, where all of the magnetization in the cube pointing along the same direction. Such single domain structure is usually available in nano magnetic particles. For larger magnetic material without strong anisotropy, the domain structure shown in panel (b) (c) and (d) is common, because in these multi-domain structures the magnetic induction line is closed and the self-interaction energy is minimized. (Just like when putting two bar magnets together, they (energetically) prefers an anti-parallel configuration). Panel (e) (f) are zoom-in views of domain wall. (e) is a Bloch wall and (f) is a Neel domain wall. As shown in Figure 1.6, since multiple magnetic structures are possible in the same cube, determination of the actually magnetic state in a device can be tricky. In some cases, when the energy landscape of the magnetic texture is complicated, there can be multiple meta stable states and the magnetization can even be frustrated, reminding us the possibility of glassy behavior, which will be discussed in detail in the following chapters.

Besides the "common" domain structure shown in Figure 1.6, there are other topologically interesting domain structures. For example, the vortex structure is

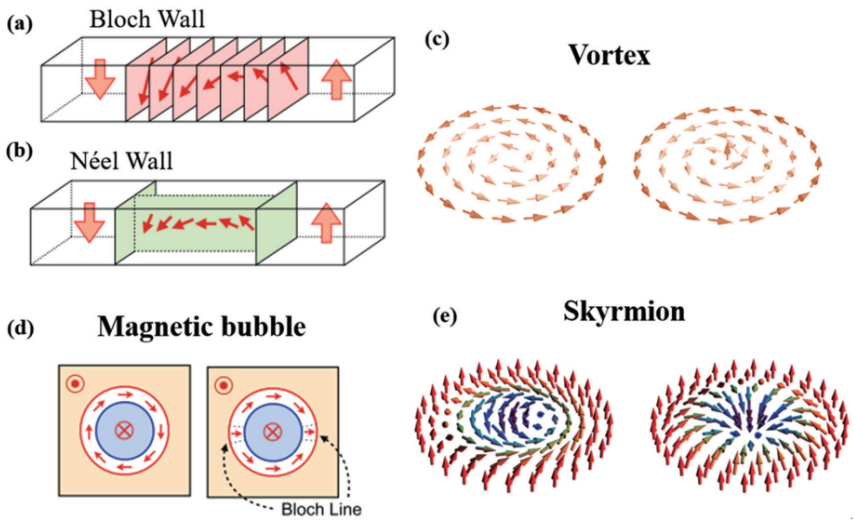

Figure 1.7: Schematic diagram of spin configurations (a) Bloch wall (b) Neel wall (c) clockwise and counterclockwise vortex (d) magnetic bubble (e) skyrmion [4].

shown in Figure 1.7 (c) [4]. Although it is similar to the domain in Figure 1.6(a); however, the magnetization rotates continuously. (interestingly, noticing that the magnetization on different sizes of a vortex is opposite, sometimes within a magnetic stripe, vortex itself can be a domain wall [20]). Panel (e) in Figure 1.7 shows a special texture called skyrmions, which is an research active field. Skyrmions are interesting because they can be tiny (∼100 nm), localized (compared with vortex, skyrmions can exist in uniform magnetic background) and topologically protected (stable) [21].

Since in previous part of this section, we mainly focus on magnetization within domains, here it is worthy to briefly discuss the region between domains, the domain wall. In a simple model of 1D spin chain [22], where only the exchange energy and uniaxial anisotropy is considered, for a 180 degree domain wall, the balancing between these two terms gives $\theta = \pm 2arctan[e^{y/\Delta}]$. Here, θ represents the rotation of magnetization within the domain wall and $\Delta = \sqrt{\frac{A}{K_1}}$ is the domain wall width parameter. Although there are different ways to define the domain wall width, Δ gives the order of magnitude of domain wall width. For common magnetic materials, the domain wall width is around a few hundreds of atoms. It is worthy to note that

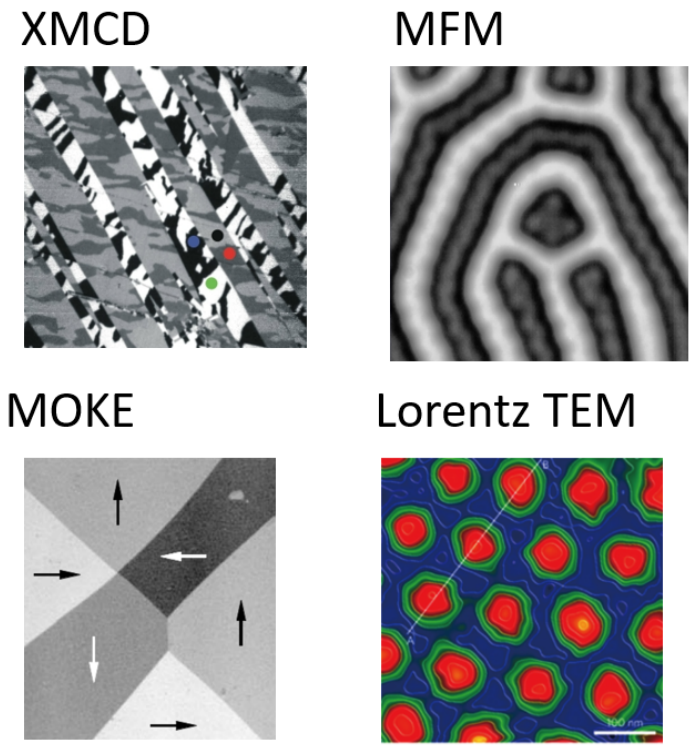

Figure 1.8: Domain structure imaged by XMCD (www-ssrl.slac.stanford.edu /stohr/xmcd), MFM (Wikipedia), MOKE [5] and Lorentz TEM [4].

the domain wall width is proportional to $\sqrt{A}$ and inversely proportional to $\sqrt{K_1}$. The result matches with our physical intuition. For system with large exchange stiffness (large A), a spatially slow rotation is preferred as the large exchange stiffness prefers small angle rotation between the magnetic moment of adjacent atoms. However, when the anisotropy is large, since in the middle of the domain wall, the magnetization is pointing along the hard axis, which is not energetically favored by the anisotropy term. Thus, for system the large anisotropy, domain wall would be "narrow". Nevertheless, in common magnetic texture, the domain wall width is much smaller than the size of domain and that is why in panel (a) (b) (c) (d) of Figure 1.6, domain walls are depicted as solid lines.

1.7 Imaging techniques of magnetic texture

In previous sections, we discussed the magnetic textures in ferromagnetic material. One natural question is how to detect the variation of domain structure. Multiple methods have been developed to directly observe the magnetic domain structure, such as X-ray magnetic circular dichroism (XMCD) [23], Magneto-optic Kerr effect [5], Magnetic force microscope [24] and Lorentz transmission electron microscopy [4]. Some pictures of domain structure taken by these techniques are shown in Figure 1.8. These techniques provide direct image of domain structures.

1.8 Anisotropic magnetoresistance

Moreover, magnetoresistance could also provide useful information of magnetic structure. Although, generally magnetoresistance measurement can't directly probe the domain structure in real space, it has the advantage of simple measurement setup and high-precision detection. Here we would briefly introduce the anisotropic magnetoresistance (AMR).

The configuration of AMR measurement is schematically shown in Figure 1.9(a). For example in Permalloy (Py), its resistance depends on the angle between of magnetization (assuming it is in single domain state) and current, $R = R_{max} - \Delta R sin^2(\varphi)$ (Figure 1.9(b)). In this case, the sample resistance is maximized when the magnetization is parallel with the current and minimized when perpendicular. The magnitude of AMR is usually $\sim$1% of the sample resistance.

1.9 Giant magnetoresistance

Another kind of magnetoresistance that has been widely explored is giant magnetoresistance (GMR) [25]. It was firstly discovered in multilayer structures, where a

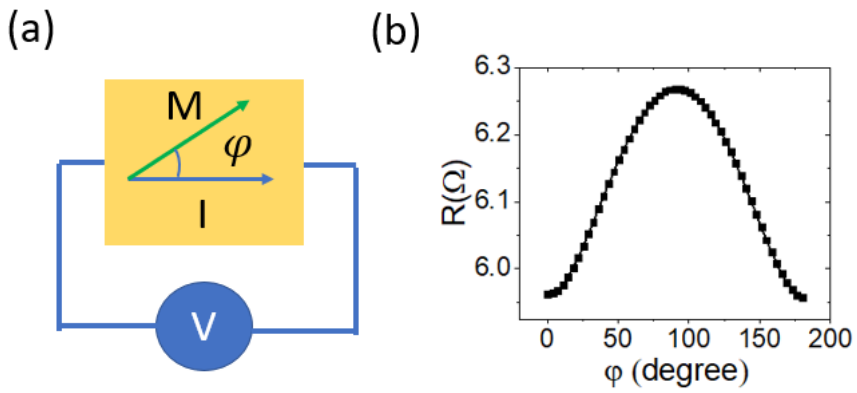

Figure 1.9: (a) Schematic diagram of AMR measurement (b) AMR result of a Py layer.

thin nonmagnetic material is sandwiched by two ferromagnetic layers. It is magnitude can be up to 50% of sample resistance, which is much larger than AMR. GMR can be realized in current in plane (CIP) and current perpendicular to plane (CPP) structure. The configuration of a CPP-GMR device is shown in Figure 1.10(a). When the magnetization in the two ferromagnetic layers are parallel (anti-parallel), the magnetoresistance is minimized (maximized). For intermediate conditions, the magnetoresistance can be expressed as $R = R_0 + \Delta R sin^2 \frac{\Theta}{2}$.

The dependence of magnetoresistance on the configuration of magnetization can be explained in a phenomenological two current model. As shown in Figure 1.10(b), the current can be viewed as a superposition of the movement of spin up and spin down current. When the electron spin is parallel with the magnetization, the channel is in low resistance state $R_{\uparrow\uparrow}$. When the electron spin is antiparallel with the magnetization, the channel is in high resistance state $R_{\uparrow\downarrow}$. Assuming that the two current channels form a parallel circuit, the total resistance of the GMR device is $R_P = \frac{2R_{\uparrow\uparrow}R_{\uparrow\downarrow}}{R_{\uparrow\uparrow}+R_{\uparrow\downarrow}}$ (large) for anti-parallel magnetization and $R_{AP} = \frac{R_{\uparrow\uparrow}+R_{\uparrow\downarrow}}{2}$ (small) for parallel magnetization.

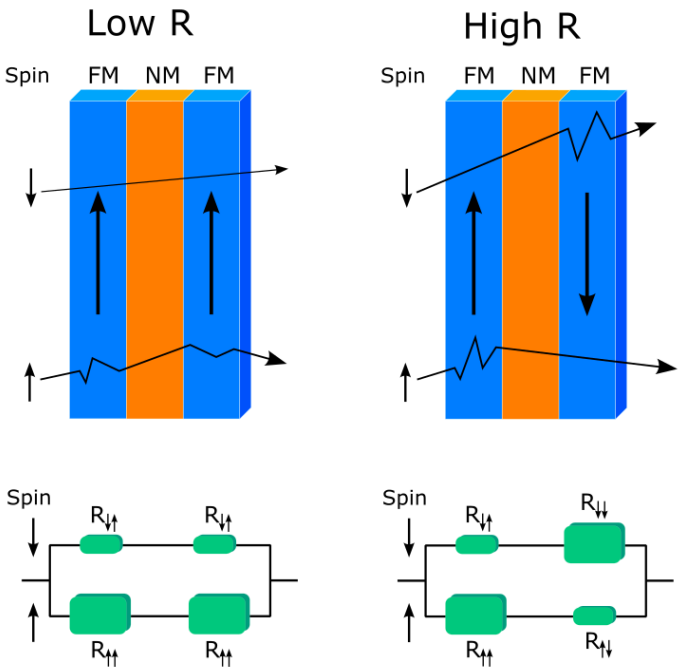

Figure 1.10: Schematic plot of the two current model for giant magnetoresistance. Picture from Wikipedia.

1.10 Landau–Lifshitz–Gilbert (LLG) equation and magnetic dynamics

In the section about magnetic domain structure, we encountered the problem where due to the existence of local minimum in the energy landscape, the multiple domain structures can be stable. In this case, the actual final state of magnetization would be determined by the evolution of magnetization with its initial condition. LLG equation is a classical description of magnetic dynamics and widely used as the foundation of micromagnetic simulation [26].

$$\begin{aligned}\frac{d\hat{m}}{dt} = -\mu_0\gamma\hat{m}\times\vec{H}_{eff} - \alpha\hat{m}\times\frac{d\hat{m}}{dt} \\ +\sigma_{DL}\hat{m}\times(\hat{m}\times\hat{s}) + \sigma_{FL}\hat{m}\times\hat{s}.\end{aligned} \tag{1.8}$$

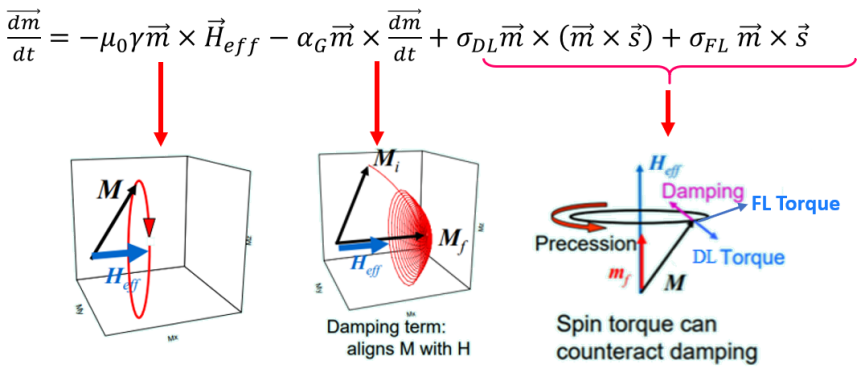

Figure 1.11: Schematic figure of the contribution of different terms in LLG equation with Slonczewski's spin transfer torque. Picture accommodated from "NIST: spin torque tutorial".

Here, $\hat{m}$ and $\hat{s}$ are unit vectors along the magnetizations and injected spin, respectively, μ_0 is the vacuum permittivity, α is Gilbert damping, and γ is the gyromagnetic ratio. The effective field $\vec{H}_{eff}$ includes crystalline and/or shape anisotropies, and the external and demagnetizing fields. As schematically shown in Figure 1.11, the first term is simply describes the Larmor precession. The second term is the Gilbert damping, which characterize the relaxation of magnetization toward its equilibrium position. Since the magnitude of the damping term is proportional to the precession rate $\frac{d\hat{m}}{dt}$, it can be viewed as a viscous damping. The third and forth terms are the Slonczewski's spin transfer torque (STT) term [27], which describes the torque exerted on the magnetization by injected spin current. The STT is the key of spintronic devices and will be discussed in detail in chapter five.

1.11 What is memristor?

Since chapter five is about the proposal of an ideal memristor in viscous magnetic system, it would be worthy to briefly introduce the idea of "memristor". There are three common devices in a electronic circuit, capacitor, resistor and inductor. As shown in Figure 1.12(a), multiple electrical quantities are connected by these

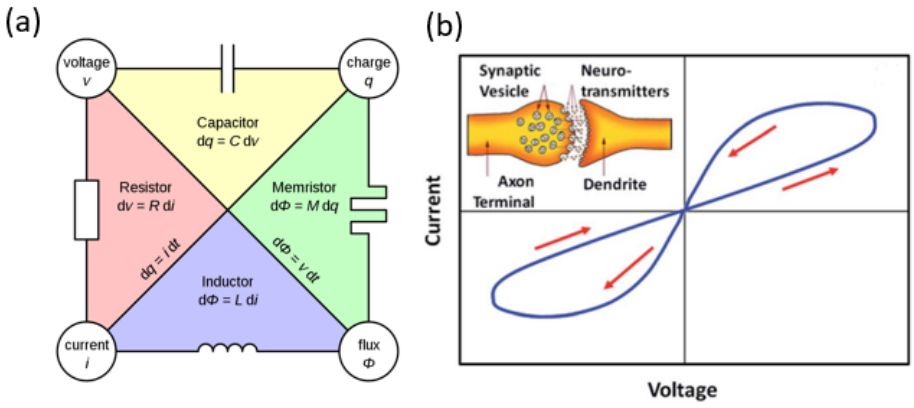

Figure 1.12: (a) Conceptual symmetries between resistor, capacitor, inductor, and memristor (Picture from Wikipedia) (b) The IV curve of a memristor The inset shows a schematic illustration of biological synapse [6].

devices. In 1960's, it is noticed that due to the symmetry, it is possible to introduce a quantity "memristance" [28] with its value defined by $M = \frac{d\Phi}{dq}$. Here Φ is the magnetic flux and q is the charge. This definition is a little bit awkward, as the direct measurement of magnetic flux and charge is difficult. By using the Faraday's law and the definition of current, the expression of memristance can be written as $M(q(t)) = \frac{d\Phi}{dq} = \frac{d\Phi/dt}{dq/dt} = \frac{V(t)}{I(t)}$. In this case, the memristor can be viewed as a special resistor, with its resistance defined by the amount of charge passing through. For an ideal memristor, its memristance should be proportional the charge (q). When driven by ac current, its IV curve has a "butterfly shape, as demonstrated in Figure 1.12(b). This device is of great interest, since it can emulate the functionality of neuron by itself, which will be discussed in more detail in chapter five.

Multiple systems have been demonstrate as candidates for memristor. One example is the structure shown in Figure 1.13, where a TiO_2 layer is sandwiched by two Pt electrodes [7]. Depending on the external bias, Pt "filament" can form or annihilate, leading to the variation of resistance. Since the formation and annihilation process of Pt filament is induced by the integration effect of current, the resistance is a function of charge flow. As shown in Figure 1.13, its IV curve has the butterfly shape, which

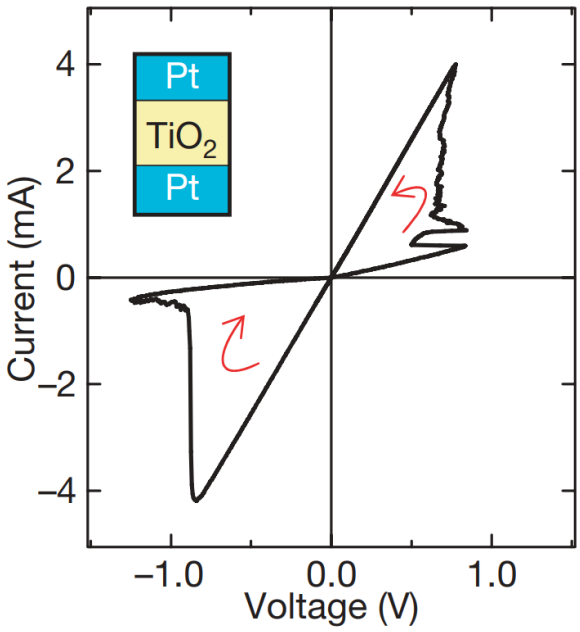

Figure 1.13: IV plot of Pt-TiO_2-Pt based memristor. [7]

is the signature of memristive functionality.

As demonstrated above, the key point of a memristor is the dependence of memristance on the "integration" of a physical quantity. Such dependence is not rare in physical system. For example, the moving distance of an object in a highly viscous medium is the integration of force over time. It suggests that the memristive functionality can be realized via viscous dynamics. Here, we provide a proof-of-principle result of a viscous memristor.

As shown in Figure 1.14 (a), we first connect a motor electrically in series with a variable resistor and also connect their shafts. The rotation angle of the well-lubricated motor with low inertia is proportional to the charge Q that flows through it, while the resistance of the variable resistor is proportional to the angle of its shaft, i.e. $R = R_0 + aQ$. (The damping in the motor plays the role of viscosity, i.e., its rotation angle is approximately proportional to the integration of current overtime.) To explicitly demonstrate its memristive functionality, the IV curve is plotted in Figure 1.14 (b). As demonstrated in the section about LLG equation, the viscous

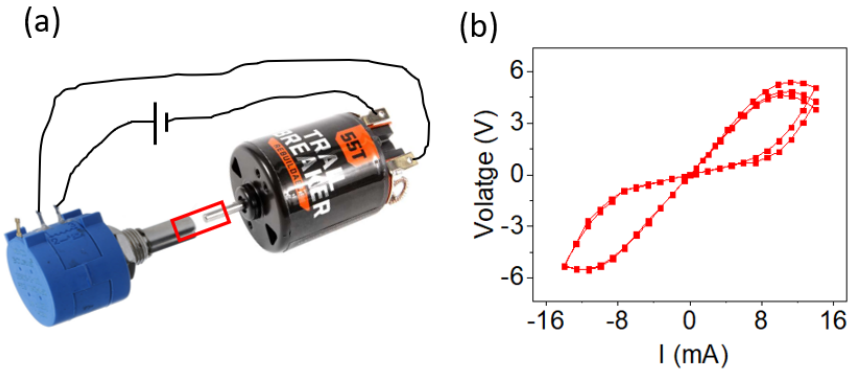

Figure 1.14: (a) Picture of the memristor made up of a motor and a variable resistor. (b) The IV curve of the device.

damping also exists in magnetic system (the Gilbert damping). In chapter five we will continue on the idea of building memristor via viscous dynamics and an ideal memristor based on viscous magnetization dynamics driven by spin torque will be proposed.

Chapter 2

Nonequilibrium phonon distribution in current-driven nano- and micro-structures

2.1 Joule's heating and diffusive heat transfer

Downscaling of modern electronic devices and circuits places ever increasing demands on their operation under increasingly non-equilibrium conditions. At small electric current density J in metallic materials, the electric field E is given by the Ohms law $E = \rho J$, where the material resistivity ρ is assumed to be independent of J. At sufficiently large J, ρ generally becomes bias-dependent, resulting in a nonlinear (non-Ohmic) dependence of E on J.

Non-Ohmic behaviors are common in non-metallic structures. For instance, the conductivity of tunnel junctions is generally bias-dependent, due to the phonon-mediated inelastic tunneling [29]. The non-Ohmic behaviors observed in disordered graphene are associated with the bias-assisted hopping transport of charge carriers [30]. In semiconductors, the non-Ohmic behaviors at large bias are manifested by

the phenomenon of current saturation, which is associated with the onset of spontaneous emission of optical phonons [31]. A strongly non-equilibrium distribution of electrons formed at large bias can also result in purely electronic non-Ohmic contributions to transport properties [32].

In metallic structures, the most common mechanism of non-Ohmic behaviors is associated with electron scattering on phonons generated by current, generally resulting in an increase of ρ with increasing current. In macroscopic systems, current-generated phonons inevitably thermalize, and the effects of current can be well described as an increase of temperature $T^*(J)$ characterizing the distributions of both electrons and phonons. This temperature increase is defined as Joule heating [33, 34]. The thermal energy, generated at a rate $w = \rho J^2$ per unit volume, is dissipated by the diffusion of electrons and phonons away from the heated region, as described by the Fourier's heat diffusion equation ($q = -\kappa \nabla T$) [35].

Since most materials exhibit a significant variation of resistivity with temperature, its current-dependence is commonly utilized for the characterization of Joule heating. This approach is also often extended to nanostructures [36, 37, 38]. However, recent studies have shown that in nanoscale systems, the electron and the phonon distributions may not be adequately described by a single current-dependent temperature [39, 40], because electrons and/or phonons can escape from the system before they thermalize. We broadly define this regime as the breakdown of the Joule heating approximation. For instance, if electrons can quickly escape and are sufficiently weakly coupled to phonons, their effective temperature can be significantly lower than that of phonons, resulting in complex nonlocal energy transfer processes between the two subsystems [41, 42, 43, 44, 45, 46]. In this case, the electrons and phonons can still be separately characterized by effective temperatures, which are generally not the same for the two subsystems.

Electrons and/or phonons may also form a nonequilibrium distribution within

the respective subsystem, which cannot be characterized by an effective temperature [47, 48, 49]. One example is the ultra fast laser excitation. In those experiments, as the fs laser pulse is much shorter than thermalization process of electron and phonons system. Right after the excitation, the electron/phonon system is in highly nonequilibrium state and the following relation process has been investigated in detail by pump probe measurement [50]. Though significant progress has been recently achieved in the understanding of non-equilibrium states of electrons and phonons at nanoscale [51, 52, 53, 54, 55], a comprehensive microscopic understanding of current-induced thermal energy generation and transport has not yet emerged.

2.2 Experimental approach

Here, we experimentally demonstrate that at cryogenic temperatures, common nanostructures such as thin-film metallic nanowires exhibit an anomalous linear variation of resistance with current. We show that this dependence cannot be described by a current-dependent temperature, and is thus inconsistent with the Joule heating approximation. As the temperature is increased, the linear dependence is broadened, and behaviors consistent with Joule heating eventually emerge at sufficiently high temperatures. Nevertheless, signatures of anomalous current dependence persist at temperatures as high as 200 K. We attribute the observed behaviors to substantially non-equilibrium phonon distribution facilitated by the fast phonon escape from the nanoscale system. Based on our interpretation, we show that the observed anomalous behaviors can provide insight into the nonequilibrium electron and phonon dynamics at nanoscale, lead to new approaches to the characterization of electron-phonon interaction, and facilitate the optimization of thermal management in electronic nanodevices.

Below, we discuss mainly the results for thin-film Pt wires deposited on undoped

Si substrates. Similar wires are extensively utilized for spin current generation in spin-orbitronic devices that rely on the spin Hall effect exhibited by Pt [56, 57, 58, 59, 60], as well as microscale heaters and thermometers [61]. We have also performed measurements for other materials and substrates: Au wires on Si, as briefly discussed below, Pt wires on SiO_2 and sapphire, as well as resistive metallic nanocontacts. All these measurements yielded consistent results, suggesting that the observed non-equilibrium phenomena are quite general to micro- and nano-scale current-driven structures characterized by efficient phonon relaxation.

The studied wires were fabricated by a combination of e-beam lithography and high-vacuum sputtering. To ensure consistent thermal contact between the wires and the substrate, native surface oxide was removed from the Si surface by HF etching immediately prior to the Pt wire deposition. The deposited Pt was polycrystalline, due to the large lattice mismatch between Pt and Si. The wires were contacted by four Cu(150) electrodes for the four-probe resistance measurements, which allowed us to eliminate the contribution of the contact resistance between the electrodes and the wires. Here and below, numbers in parentheses are thicknesses in nanometers. Differential resistance $R = dV/dI$ was measured using the standard lock-in technique, with ac current $I_{ac} = 10\ \mu A$ rms superimposed with the dc current I of up to ± 4 mA.

The measured resistivity of the studied Pt films linearly depended on the inverse film thickness d [inset in Fig. 2.1(a)], consistent with the expected contribution of surface scattering [62]. For large thicknesses, the resistivity approaches the usual values reported for bulk sputtered Pt [62]. We note that thin Pt films deposited on SiO_2 and sapphire exhibit significantly lower resistivity than similar films on Si. Since the roughness $\approx 0.25 - 0.3$ nm rms of the substrate and of the film surface, as measured by atomic force microscopy, was similar for all these films, we conclude that the large resistivity of thin Pt films on Si is caused by the diffuse electron scattering at the Pt/Si interface. This allowed us to explore a large range of transport parameters

controlled by the film thickness. We emphasize that the reported nonequilibrium effects were also observed in thin films deposited on sapphire and SiO_2, where the interface contribution to resistivity was much smaller. Therefore, these effects are not associated with the specific scattering properties of the interface.

The morphology of the substrate and deposited film surfaces were characterized by atomic force microscopy, which yield similar roughness values of $0.25 - 0.3$ nm rms. Additionally, the geometries of the fabricated structures were verified by scanning electronic microscopy (SEM). An example of the SEM image for the a 5 nm thick, 1 μm-long, 500 nm-wide Pt wire is shown in Fig. 2.1(a).

We characterized the restivity of the Pt films deposited on etched Si by measuring the resistance of several 1 μm-long, 500 nm-wide Pt wires as a function of temperature and wire thickness. The resistivity exhibits a linear dependence on inverse thickness at all temperatures, as shown in Fig. 2.1(b) for 295 K and 5 K, consistent with the expected contribution of surface scattering.

2.3 Breakdown of Joule's heating at cryogenic temperature

Figure 2.2 shows representative resistance vs current curves for a 1 μm-long and 500 nm-wide Pt(5) wire. At the experimental temperature $T = 295$ K, the resistance $R(I)$ follows a quadratic dependence on current I [Fig. 2.2(a)]. This result is consistent with Joule heating. Indeed, electrical energy is dissipated in the wire at a rate $W = RI^2$. Since the rate of thermal energy dissipation from the wire is proportional to its temperature increase, one can expect that the temperature of the wire follows a quadratic dependence on current $T^* \approx T_0 + CI^2$. The resistance of the Pt(5) wire exhibits an approximately linear dependence on T close to $T = 295$ K [inset in Fig. 2.2(b)]. Thus, $R(I)$ is expected to follow a quadratic dependence, in

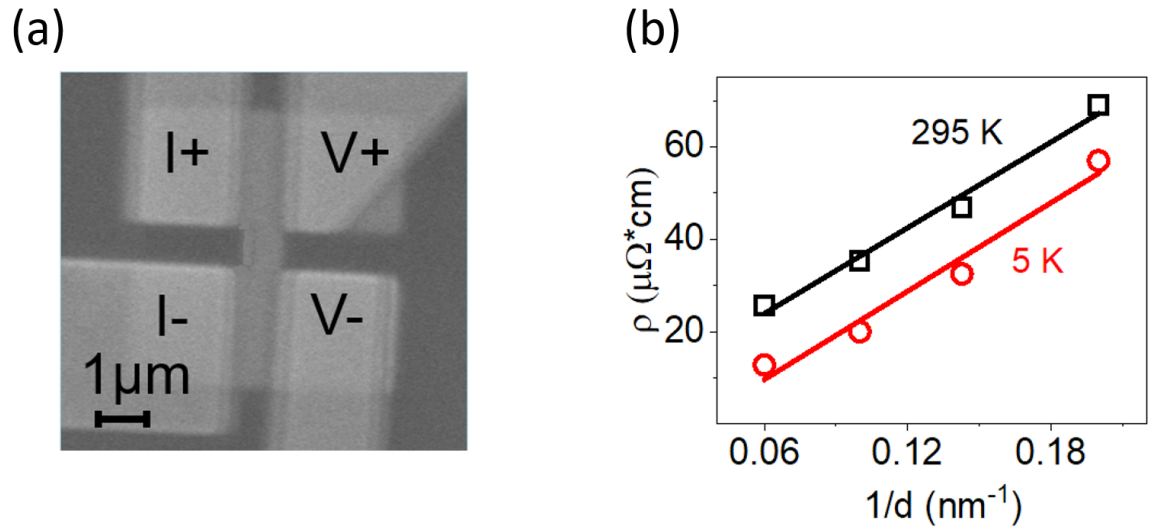

Figure 2.1: (a) SEM image of one of the studied samples, a 5 nm thick, 1 μm-long, 500 nm-wide Pt wire contacted by four 150 nm-thick Cu leads. (b) Dependence of the resistivity of Pt films on Si vs the inverse of their thickness at $T = 5$ K and 295 K, as labeled, at $I = 0$. The resistivity was determined from the resistance of the 1 μm-long, 500 nm-wide Pt wires. Solid lines are linear fitting.

agreement with our data.

At $T = 5$ K, the dependence $R(I)$ is well described by the linear function $R(I) = R_0 + \alpha|I|$, where α is a constant [Fig. 2.2(b)]. This dependence cannot be explained by Joule heating. In particular, numerical simulations confirm that for Joule heating, the dependence $T^*(I)$ of the Pt wire temperature on current should be quadratic even at cryogenic temperatures. The resistance of Pt is almost independent of temperature up to 20 K, due to the freeze-out of large-momentum phonons, and starts to increase approximately linearly with T at higher temperatures [inset in Fig. 2.2(b)]. Simulations show that as a consequence, Joule heating should not affect R for currents up to about 1.8 mA, and should lead to an approximately quadratic dependence $R(I)$ for larger currents. The observed dependence $R(I)$ is clearly qualitatively inconsistent with these expectations.

The anomalous current dependence of resistance cannot be attributed to tunneling or electron hopping effects discussed in the introduction, because the electron

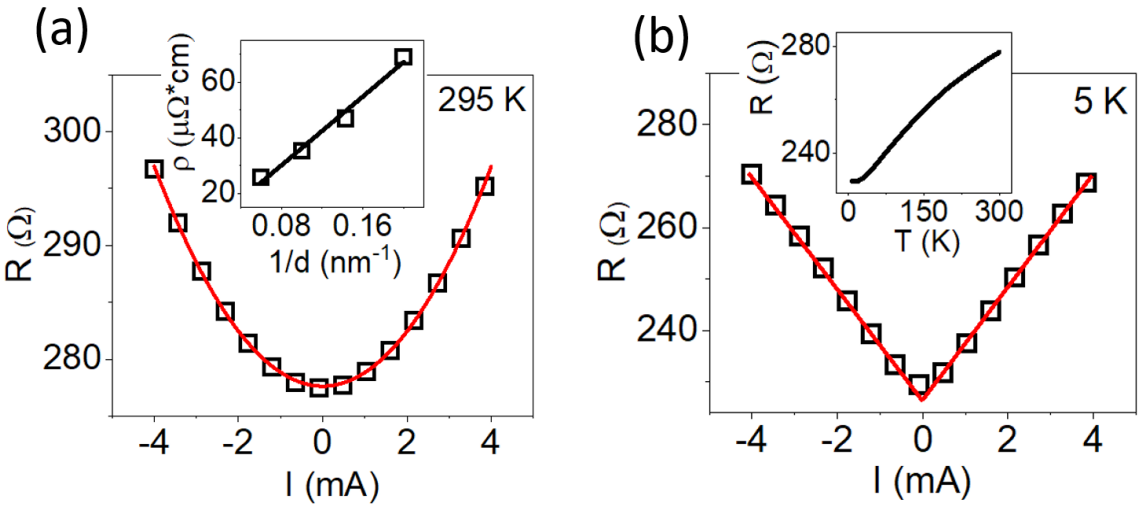

Figure 2.2: (a) Resistance vs current for a 1 μm-long, 500 nm-wide, 5 nm-thick Pt wire deposited on etched Si substrate, at room temperature $T = 295$ K. Curve is the best fit to the data with a quadratic function. Inset: Resistivity of Pt deposited on Si substrates vs inverse Pt thickness, at 295 K. (b) Same as (a), at $T = 5$ K. Curve is a fit with the linear function $R(I) = R(0) + \alpha|I|$, where α is a fitting parameter. Inset: the dependence of the wire resistance on temperature at $I = 0$.

transport properties of the studied metallic thin film wires are determined by scattering rather than tunneling, as can be inferred from the decrease of resistance with decreasing temperature [inset in Fig. 2.2(b)]. The effects of contact resistance are eliminated in our measurements by the four-probe geometry. We also performed separate two-probe measurements that produced very similar results, except for the overall resistance increase due to the contribution of electrodes, confirming that the contact resistance is not relevant to the observed effects.

We can also eliminate the purely electronic contribution to the dependence $R(I)$, because the linear term in this dependence does not change sign with the direction of current, and is negligible for inversion-symmetric materials such as Pt. [32]. One can also expect that such effects should also sensitively depend on the band structure. However, our results for an Au wire discussed below are very similar to those for Pt, despite large differences in their band structure. Resistance may be also affected by the complex nonlocal transport phenomena, which have been reported for mesoscopic

wires with mean free path comparable to the wire dimensions [63]. However, we estimate that the mean free path in our Pt(5) film is only 2 nm, due to the diffuse electron scattering at the Pt/Si interface, resulting in negligible nonlocal effects.

2.4 Dependence of R(I) on temperature

We hypothesize that the observed anomalous low-temperature dependence $R(I)$ is associated with electron scattering on non-equilibrium phonons generated by current, whose distribution and population are qualitatively different from that expected from the Joule heating picture. Indeed, analysis presented below indicates that the linear $R(I)$ dependence can be explained within the Drude-Sommerfeld approximation for electron transport, in conjunction with the simple kinetic analysis of phonon relaxation in the limit of negligible thermalization. Independent estimates of phonon relaxation rates confirm the validity of this approximation. Fast escape of the generated phonons from the system is expected to be the only requirement for the observed non-equilibrium behaviors, and therefore such behaviors should be quite common in current-driven micro- and nano-structures characterized by efficient phonon relaxation.

We now discuss the dependence on temperature, which provides insight into the mechanism of the emergence of behaviors consistent with Joule heating at high temperatures. As the temperature is increased from 5 K, the linear dependence remains evident at large currents, but the zero-current singularity becomes increasingly smoothed-out [Fig. 2.3(a)]. This broadening is reminiscent of the thermal effects observed in electronic spectroscopy of tunnel junctions and point contacts, which can be accounted for by convolving the zero-temperature spectra with the normalized derivative $\frac{df_0}{d\epsilon}$ of the Fermi-Dirac distribution function $f_0(\epsilon) = \frac{1}{e^{\epsilon/k_BT}+1}$, where ϵ is the energy relative to the chemical potential [64]. This function can be well approximated

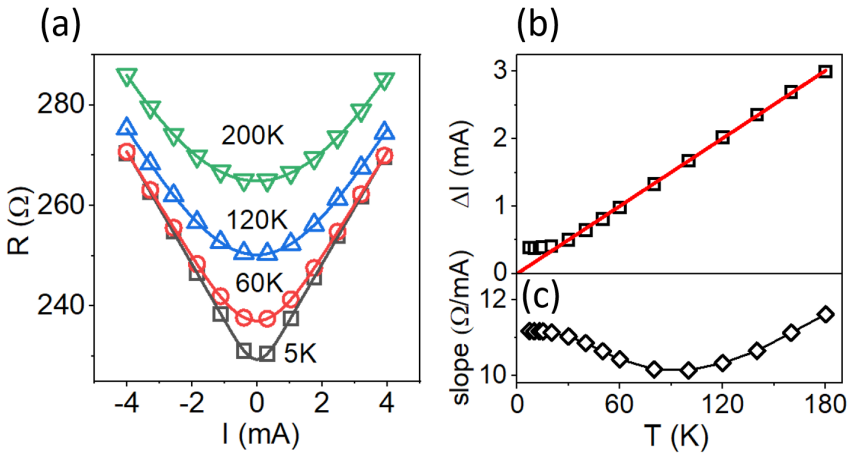

Figure 2.3: (a) Symbols: R vs I for the same sample as in Fig. 2.2, at the labeled values of T. Curves: best fits with the linear function $R(I) = R_0 + \alpha|I|$ convolved with the Gaussian $g(I) = \frac{1}{\sqrt{2\pi}\Delta I} e^{-I^2/2\Delta I^2}$. Some of the data points are omitted for clarity, but fitting was performed for the entire data set. (b),(c) Parameters extracted from the data fitting: the Gaussian width ΔI (b) and the slope of the linear dependence (c). The line in (b) is the best linear fit of the data for $T > 20$ K.

by the Gaussian

$$g(\epsilon) = \frac{1}{\sqrt{2\pi}\sigma} e^{-\epsilon^2/2\sigma^2}, \tag{2.1}$$

with $\sigma \approx 1.6 k_B T$. Indeed, a linear function $R(I) = R(0) + \alpha|I|$ convolved with the Gaussian

$$g(I) = \frac{1}{\sqrt{2\pi}\Delta I} e^{-I^2/2\Delta I^2}. \tag{2.2}$$

provides a good fitting for all our $R(I)$ data measured at different temperatures, as shown by curves in Fig. 2.3(a). At $T > 200$ K, the width ΔI of the Gaussian becomes larger than the range of the dc current scan, resulting in a significant uncertainty of the fitting. Nevertheless, these data suggest that a non-equilibrium current-driven phonon distribution, not described by Joule heating, can be formed at sufficiently large bias even in the ambient temperature range. On the other hand, at small currents, thermal broadening results in a quadratic $R(I)$, consistent with the dependence expected for Joule heating.

We emphasize that in the studied microstructures, phonons are not expected to

thermalize even at elevated temperatures, due to their efficient relaxation. Instead, behaviors consistent with Joule heating emerge because of the thermal broadening of the electron distribution, resulting in a nearly thermal distribution of the generated phonons.

In tunnel junctions or point contacts, the characteristic electron energy competing with the thermal broadening is defined by the bias across the junction [64]. We hypothesize that in the studied metallic wires, the characteristic electron energy defining the thermal broadening scale is the energy provided to electrons by electric field between the scattering events, which is to a good approximation proportional to the bias current. Indeed, the Gaussian width ΔI follows a linear dependence at $T > 20$ K, extrapolating to $\Delta I = 0$ at $T = 0$ [right scale in Fig. 2.3(b)]. This result is consistent with our hypothesis that the observed broadening of $R(I)$ originates from the thermally induced spectral broadening of the electron distribution, whose width is proportional to temperature. In other words, the thermal broadening of $R(I)$ can be interpreted in terms of the competition between the thermal energy $k_B T$ of electrons, and the average energy acquired by electrons between scattering events due to the electric field in the wire. The broadening saturates at $T < 20$ K, suggesting the existence of an additional non-thermal broadening effect. Indeed, at small bias and low temperatures, the energy (and thus the momentum) of phonons generated by current is small, resulting in a reduced contribution of the generated phonons to electron scattering, and thus resistance. We expect that detailed theoretical analysis of these broadening effects, which is beyond the scope of the present work, will provide quantitative information about the relevant energy scales, leading to new quantitative insights into electron transport in nanostructures.

The slope of the linear dependence decreases with increasing temperatures up to 90 K, and then increases at higher temperatures [Fig. 2.3(c)]. These variations are likely associated with the temperature dependence of phonon relaxation rate, which

is dominated by the dissipation into the substrate, as shown below. Qualitatively, there is some correlation between the observed variations of the slope and the temperature dependence of thermal conductivity of bulk Si, which increases with increasing temperature at low temperatures, exhibits a peak typically at temperatures between 30 K and 100 K, and then decreases at higher temperatures [10, 8]. However, the variations of thermal conductivity are almost two orders of magnitude larger than those of the slope in Fig. 2.3(c), suggesting that phonon relaxation may not be adequately described by the diffusive heat transport. Indeed, the phonon mean free path in Si significantly exceeds the dimensions of the studied structures [65]. Therefore, phonons are expected to quasi-ballistically escape into the Si substrate, with negligible contribution from the phonon-phonon scattering governing heat diffusion. Thus, measurements of temperature-dependent slope of $R(I)$ in nanostructures, such as those discussed here, may provide a new method for characterizing phonon transport and relaxation at nanoscale.

2.5 Dissipation channels of the nonequilibrium phonons

Non-equilibrium phonon distribution in the studied Pt wires, manifested by the linear dependence $R(I)$, is associated with fast relaxation of phonons due to their efficient escape from the system, before they become thermalized. To elucidate the mechanisms of phonon relaxation, we analyze the effects of the wire geometry. Phonons are expected to dissipate mainly into the thick Cu leads and the substrate. If phonons dissipate predominantly into the leads, then the efficiently of their dissipation should decrease with increasing wire length L, due to the longer average distance they travel before escaping. On the other hand, the phonon dissipation efficiency, per unit Pt volume, should not be significantly affected by the wire thickness d, aside from the

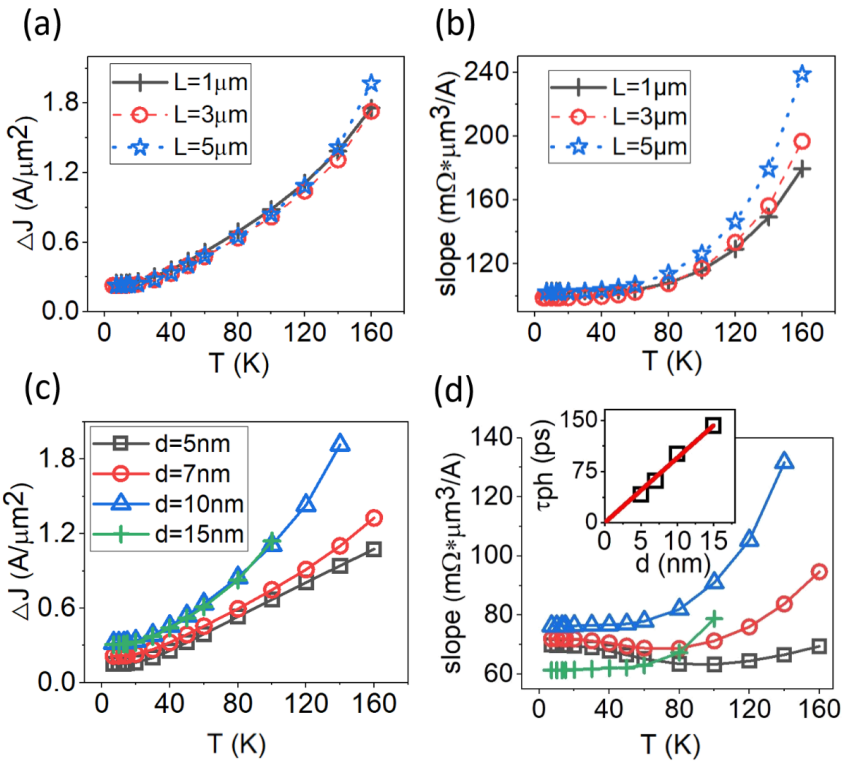

Figure 2.4: Effects of the Pt wire geometry. (a),(b) Temperature dependence of the Gaussian broadening width ΔJ (a) and the linear slope (b) of $\rho(J)$, for 10 nm-thick Pt wires with lengths $L = 1$ μm, 3 μm, and 5 μm, as labeled. (c),(d) Same as (a), (b), for 1μm-long Pt wires with thicknesses $d = 5$ nm, 7 nm, 10 nm, and 15 nm, as labeled in (c). Inset in (d): Dependence of the phonon relaxation rate τ_{ph} on the Pt thickness, determined from the data at $T = 5$ K using Eq. (2.11) (symbols), and linear fit with zero intercept (line).

effects of thickness on the phonon mean free path. However, if phonons dissipate predominantly into the substrate, the length of the wire should not affect the phonon escape into the substrate. On the other hand, increasing the wire thickness d should lead to an increase of the average phonon escape time, resulting in less efficient dissipation (per unit Pt volume). Figure 2.4 summarizes the results for different values of L and d. To facilitate direct comparison of different geometries, we analyze the dependence of resistivity $\rho = RA/L$ on the current density $J = I/A$, where A is the cross-section area of the wire. In all cases, we obtained accurate fits of the data by using a linear dependence convolved with the Gaussian. For the thickest (15 nm) Pt wire, the analysis is limited to $T \leq 100$ K, because of the large thermal broadening

for this thickness.

The thermal broadening ΔJ is independent of the wire length [Fig. 2.4(a)]. The linear slope of $\rho(J)$ is almost independent of length at temperatures up to about 80 K, and starts to increase with increasing length at higher temperatures. However, the dependence on length remains modest even at $T = 160$ K. Thus, we conclude that at cryogenic temperatures, phonons relax in the studied Pt wires predominantly through the substrate.

In contrast to the effects of the wire length, wire thickness significantly affects the characteristics of $\rho(J)$, Figs. 2.4(c),(d). The broadening increases by a factor of two when d is increased from 5 nm to 10 nm, and saturates at larger d. For Pt(5), it increases linearly with temperature $T > 20$ K. This result is consistent with our interpretation of the broadening in terms of the competition between the electron's thermal energy kT and the energy $\propto J$ provided by the electric field between electron scattering events. The observed curving of the dependence $\Delta J(T)$ for larger Pt thickness, especially apparent in Fig. 2.4(c) for Pt(10) and Pt(15), can be attributed to the larger relative contribution of electron-phonon scattering to the electron mean free path, resulting in the reduction of energy acquired by electrons between the scattering events.

The linear slope of $\rho(J)$ also exhibits a significant dependence on the wire thickness, especially apparent at higher temperatures [Fig. 2.4(d)]. The slope increases with wire thickness up to 10 nm, and then decreases for Pt(15), in the temperature range up to 100 K where the broadening was sufficiently small to allow a reliable determination of the slope. These nonmonotonic variations can be explained by the competition between the decrease of the phonon generation rate, with increasing Pt thickness, due to the smaller contribution of scattering at the Pt interfaces, and the increase of phonon escape time, as shown by the analysis below [see also inset in Fig. 2.4(d)].

2.6 Mechanics of the breakdown of Joule's heating

To interpret the observed behaviors, and to evaluate the material parameters that control the non-equilibrium phonon distribution, we perform kinetic rate analysis of the current-driven phonon population. In the Drude-Sommerfeld approximation, the electron mean free path is $l_e = \frac{m^* v_F}{ne^2\rho}$, where v_F and m^* are the Fermi velocity and the effective mass, respectively [66]. In the presence of electric field, the rate of electron scattering per unit volume is $r = \frac{J}{el_e} = \frac{ne\rho}{v_F m^*} J$. Assuming that one phonon is generated in each scattering event, the rate of phonon generation per unit volume is $\frac{dn_{ph}}{dt}|_{gen} = r$. Relaxation due to the quasi-ballistic phonon escape from Pt can be described by the relaxation time approximation

$$\frac{dn_{ph}}{dt}|_{rel} = -\frac{n_{ph} - n_0}{\tau_{ph}}, \tag{2.3}$$

where n_0 is the phonon population in the absence of current, and τ_{ph} is the relaxation time, which is equal to the phonon escape time due to the rapid phonon escape. In the steady state, $\frac{dn_{ph}}{dt}|_{gen} + \frac{dn_{ph}}{dt}|_{rel} = 0$, or

$$n_{ph} = n_0 + \frac{\tau_{ph} ne\rho}{v_F m^*} J. \tag{2.4}$$

The parameters n, v_F, and ρ in this expression are generally dependent on the current density J. For good metals such as Pt, the carrier density is to a very good approximation independent of current. To analyze the bias-driven variations of v_F, we note that electric bias results in a shift of the Fermi surface, affecting the average Fermi velocity [67]. Using the Drude-Sommerfeld approximation, we find $\Delta\vec{v} = \vec{J}/ne$ for the bias-driven change of the electron velocity between the scattering events. For Pt(5) at $I = 4$ mA, we calculate that Δv_F is less than 5% of v_F. Furthermore, the net effect is expected to become negligible when averaged over the Fermi surface, since the variation of the magnitude of electron velocity depends on the direction of

wavevector. In contrast, the dependence of ρ on J is generally non-negligible, as is apparent from the experimental results discussed above. Below, we first derive the general expression accounting for this dependence, and then show that the contribution of the current-dependence of ρ to the phonon population in our measurements is small.

To establish the relationship between the current dependence of resistance and phonon generation/relaxation characteristics, we use the Matthiessen's rule for the electron mean free path in the presence of current-generated phonons, $1/l_e = 1/l_{e,0} + n_{ph}\sigma_{e-ph}$. Here, $l_{e,0}$ is the mean free path in the absence of phonons, and σ_{e-ph} is the average electron-phonon scattering cross section. Combining with Eq. (2.4), we obtain

$$\rho(J) = \frac{\rho(0)}{1 - \tau_{ph}\sigma_{e-ph}J/e}. \tag{2.5}$$

Expanding in powers of the current density, we obtain to the lowest order in $\tau_{ph}\sigma_{e-ph}J/e$

$$\rho(J) \approx \rho(0)[1 + \tau_{ph}\sigma_{e-ph}J/e]. \tag{2.6}$$

According to this relation, to the lowest order in J, the resistivity is expected to depend linearly on the current density, in agreement with our experimental data. The validity of Eq. (2.11) is contingent upon several conditions. First, the kinetic rate equation Eq. (2.3) relies on negligible phonon thermalization. We utilized several independent approaches to estimate that this condition is well-satisfied in the studied wires. For very thick films or bulk samples, phonon thermalization is expected to result in the usual Joule heating characterized by a qualitatively different dependence $\rho(J)$. Second, the generated phonons must efficiently scatter electrons, which requires that their characteristic momentum is comparable to the Fermi momentum of electrons, such that the electron scattering on the generated phonons can described by the average scattering cross-section parameter σ_{e-ph}. Because of the energy con-

servation, this condition is not satisfied at small bias, consistent with the observed rounding of the linear dependence around $J = 0$. Finally, the linear approximation for $\rho(J)$ holds only for $J \ll e/\tau_{ph}\sigma_{e-ph}$. Based on Eq. (2.11), this condition can be equivalently formulated as $(R(J)/R(0) - 1) \ll 1$. This is well-satisfied for the the presented measurements, with the largest value of $(\rho(J)/\rho(0) - 1) \approx 0.17$ reached at $I = 4$ mA for the Pt(5) wire. We have performed additional measurements of the nonlinear regime at larger currents, which could be well described by the general Eq. (2.10) without any additional fitting parameters.

It should be emphasized that the obtained results are independent of the functional form of $\rho(T)$, which usually exhibits an approximately linear dependence on temperature at high temperatures, and saturates at low temperatures, due to the freeze-out of large-momentum phonons. As a consequence, Joule heating results in a quadratic or even slower dependence $\rho(J)$, instead of the linear dependence in the non-thermalized regime discussed above.

These differences are closely related to the differences between phonon populations and characteristic energies in the two regimes. In particular, according to Eq. (2.4), the population of non-equilibrium phonons is proportional to current density. Meanwhile, their characteristic energy is determined by the energy acquired by electrons due to electric field between the scattering events, which is also approximately proportional J. We can contrast this with Joule heating at sufficiently high temperatures, when $\rho(T)$ is approximately linear, and $\rho(J)$ is quadratic. In the degenerate regime above the Debye temperature, the average phonon energy is independent of T, while according to the Rayleigh-Jeans law, their population is proportional to T. Thus, in the Joule heating regime, the average phonon energy is independent of J, while their population is quadratic in J. The total phonon energy $\propto J^2$ is the same in both regimes, as expected since the dissipated power is $w = \rho J^2$.

The result in Eq. (2.11) demonstrates that the linear slope of the dependence $\rho(J)$

provides direct information about phonon relaxation and electron-phonon scattering. For the studied Pt wires, because of the effects of electron scattering at the film interfaces, as reflected the thickness dependence of resistivity [inset in Fig. 2.2(a)], the phonon population [and thus the slope of $\rho(J)$], determined by the balance between phonon generation and escape rates, exhibits a complex dependence on d [Fig. 2.4(d)]. This is reflected in Eq. (2.11) by the dependence of the slope of $\rho(J)$ on both $\rho(0)$ and τ_{ph}. To gain insight into the observed variations, we use σ_{e-ph} determined from the temperature dependence of resistivity and the measured $\rho(0)$ to calculate the values of τ_{ph} for different Pt wire thicknesses d. The dependence of $\tau_{ph}(d)$, determined from the $T = 5$ K data, is well described by a linear function with zero intercept, as expected for the substrate-dominated relaxation [inset in Fig. 2.4(d)]. The experimental values of τ_{ph} are in a semi-quantitative agreement with the calculation of the quasi-ballistic phonon escape time into the substrates based on the acoustic mismatch theory. These results confirm that phonon relaxation in the studied Pt wires is dominated by the fast quasi-ballistic phonon escape into the substrate, which facilitates non-equilibrium current-driven phonon distribution.

2.7 Generality of the observation: the linear R(I) in Au wire

We have confirmed the general relevance of the observed behaviors to nanostructures with efficient thermal dissipation, by measurements of current-dependent resistance in Pt wires fabricated on different substrates, as well as resistive metallic nanocontacts. Here, we briefly discuss the results for an Au(5) wire deposited on HF-cleaned undoped Si substrate. A Ni(0.5) wetting layer was inserted between Au(5) and the substrate, to improve adhesion and ensure the continuity of the ultrathin Au(5). The geometry of this wire was identical to that of the Pt(5) wire

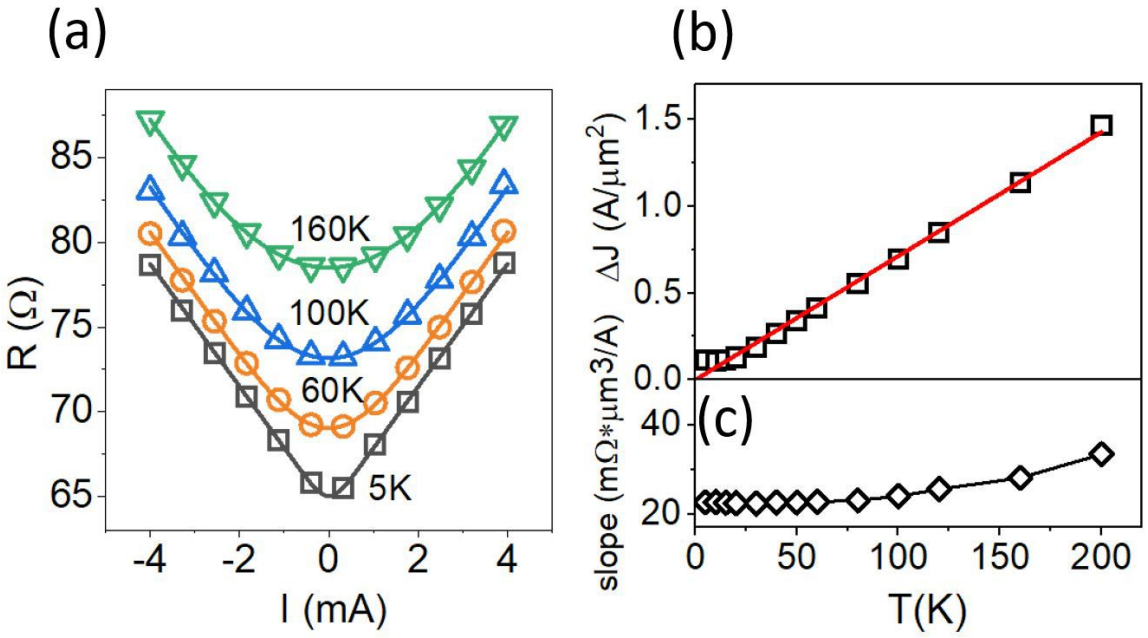

Figure 2.5: (a) Symbols: resistance vs current for a 1 μm-long, 500 nm-wide Au(5) wire on Si substrate, at the labeled values of temperature. Curves: results of the data fitting with a linear function $R(I) = R(0) + \alpha|I|$ convolved with the Gaussian. (b),(c) Parameters extracted from the data fitting: the Gaussian width ΔI (b) and the slope of the linear dependence (c). The line in (b) is the best linear fit of the data for $T > 20$ K.

in Figs. 2.2, 2.3. At $T = 5$ K, the dependence $R(I)$ is well approximated by the linear function [Fig. 2.5(a)], in agreement with the results for Pt. This dependence becomes increasingly broadened with increasing temperature, with the broadening proportional to temperature at $T > 20$ K [Fig. 2.5(b)]. The temperature dependence of the broadening is almost identical to that for Pt(5). At $T = 5$ K, the resistance of the Au(5) wire is 4 times smaller than that of Pt, while the linear slope is about 3.5 times smaller than for Pt(5). In contrast to Pt(5), the slope for Au(5) monotonically increases with temperature. This dependence is similar to that observed for Pt(10) and Pt(15), but the magnitude of the variations is smaller, closer to Pt(5) and Pt(10). The similarities between the results for Pt and Au, two materials with very different electronic band structures, confirms that the mechanisms underlying the observed effects are likely quite general to micro- and nano-scale systems characterized by ef-

ficient thermal dissipation. The almost identical thermal broadening for Pt and Au implies that the energy acquired by the electrons due to the electric field between the scattering events is almost the same for the two materials. Based on the Drude-Sommerfeld approximation, this energy is proportional to the effective electron mass and Fermi velocity, and inversely proportional to the electron density. The latter is similar in Pt and Au, while the effective electron mass is about 1.6 times larger in Pt and the Fermi velocity is about 1.4 times smaller [68]. Thus, the almost identical values of ΔJ likely result from a fortuitous cancellation of different contributions to thermal broadening. Studies of other materials where such a fortuitous cancellation is not expected can provide a critical test for the proposed interpretation.

At $T = 5$ K, the normalized slope $\frac{1}{\rho(0)}\frac{d\rho(J)}{dJ}$ is only 20% smaller for Pt(5) than for Au(5). According to Eq. 2.11, this implies that $\tau_{ph}\sigma_{e-ph}$ is similar for these materials. However, estimates based on the temperature dependence of resistivity show that $\sigma_{e-ph,Pt} \approx 4\sigma_{e-ph,Au}$, and therefore the phonon relaxation time in Au(5) at 5 K is about 5 times larger than in Pt(5). The difference between phonon relaxation times becomes even larger at higher temperatures, as manifested by the increase of the slope for Au(5). This difference is likely associated with the much larger phonon escape time from the Au film. The escape time calculated from the acoustic mismatch at Au/Si interface, assuming isotropic momentum distribution of the generated phonons, is 75 ps, less than half of the relaxation time determined from the slope of $R(I)$ at 5 K. We speculate that the large value of τ_{ph} for Au originates from its poor wetting of the substrate, resulting in reduced phonon transparency of the interface with Si. Elucidating the relationship between wetting and phonon transparency of interfaces, by measurements such as those presented here, will be important for gaining further insight into thermal relaxation mechanisms in nanostructures, and for optimizing the thermal management in nanoelectronic devices.

2.8 Dependence on the substrate type

To verify that the anomalous R vs I dependence associated with nonequilbrium current-driven phonon distribution is not limited to Pt wires on Si substrates discussed in the previous section, we have studied thin-film Pt wires fabricated on sapphire and oxidized Si [surface SiO_2 thickness 300 nm]. Figure 2.6(a) shows temperature-dependent thermal conductivities of Si, sapphire, and fused quartz. The thermal conductivity of the fused quartz (SiO_2) is several orders of magnitude smaller than that of Si and sapphire. Thus, using SiO_2 as a substrate allowed us to test whether high thermal conductivity of the substrate is essential for the observed nonequilibrium phenomena.

The dependences R vs I are shown in Figs. 2.6 (b) and (c) for Pt(5) wires fabricated on sapphire and SiO_2, respectively. The resistivity of Pt(5) on sapphire is slightly smaller than for Pt(5) on SiO_2, and about three times smaller than for the Si substrate. These differences were reproducible among different samples. The value of ρ for the sapphire substrate is slightly smaller than for SiO_2, because Pt grows on sapphire preferentially with (111) texture, as was verified by x-ray diffractometry, resulting in less electron scattering at the crystalline grain boundaries. The resistivities of very thick/bulky Pt films [200 nm-thick Pt in our studies] deposited on Si or SiO_2 substrates are similar to each other, confirming the interfacial origin of the additional contribution to the resistivity of Pt on Si. We attribute this contribution to the strongly diffuse electron scattering at the Pt/Si interface, associated with a combination of large electronic and structure mismatch between the two materials, perhaps combined with some interfacial alloying. We note that if Si diffused into Pt over distances beyond a thin interfacial region, e.g. comparable to the smallest studied Pt thickness of 5 nm, then the dependence of resistivity on thickness [Fig. 2.1(b)]] would have exhibited a nonlinear increase at small Pt thicknesses.

For sapphire, the current-driven resistance increase between $I = 0$ and $I = 4$ mA

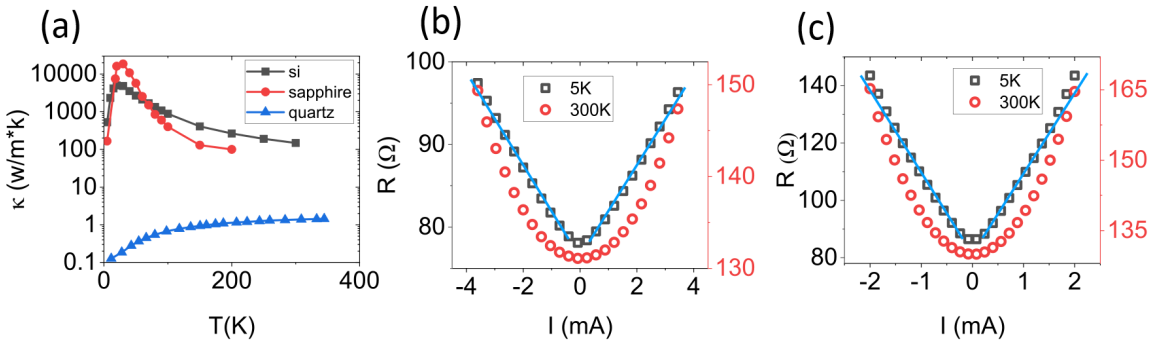

Figure 2.6: (a) Temperature dependence of thermal conductivity of Si, sapphire, and fused quartz, as labeled [from Refs. [8, 9, 10]]. (b) R vs I for a 1μm-long, 500 nm-wide Pt(5) wire fabricated on sapphire substrate, at $T = 5$ K and 300 K, as labeled. (c) Same a (b), but using a Si substrate with a 300 nm-thick thermal SiO_2 surface layer. Blue straight lines are guides for the eye.

is about 20 Ω both at 5 K and 300 K, Fig.2.6(b). In contrast, the increase for the oxidized Si substrate is significantly larger, almost 60 Ω at 5 K, and 35 Ω at 300 K, Fig.2.6(b). These results are consistent with the large differences between the thermal conductivities of the two substrates, which are expected to determine the phonon relaxation rates in the Pt wires. In particular, not only is the thermal conductivity of SiO_2 smaller than that of sapphire, resulting in a larger resistance increase, but it also decreases at low temperatures, in contrast to the increase in sapphire. This is consistent with the increasing current-dependent resistance variation for Pt on Si with decreasing temperature.

Despite significant quantitative differences among different substrates, at 5 K the curves $R(I)$ are almost linear both for sapphire and SiO_2, consistent with the non-equilibrium current-induced phonon distribution. A slight upcurving, more significant for SiO_2, is consistent with the nonlinear effects of phonon generation due to the electron scattering on the generated phonons. This effect is the most pronounced for SiO_2 substrate, because of the slower phonon relaxation. However, it becomes noticeable at sufficiently large current for other substrates, as discussed below for Pt on Si.

2.9 Dependence on the wire thickness for Pt on sapphire

In previous sections, we discussed how the observed complex thickness-dependence of the $\rho(J)$ curves reflects a competition between the decrease of scattering (phonon generation rate) and the increase of the phonon relaxation time τ_{ph}. Despite the complexity of the observed variations of the raw data with thickness d, the calculated $\tau_{ph}(d)$ exhibited a linear dependence on thickness with a zero intercept, consistent with the expectation that phonon relaxation is dominated by the phonon escape into the substrate.

Here, we confirm this relationship for Pt wires on sapphire. Namely, we show that the slope of $\rho(J)$ exhibits a nonmonotonic dependence on d, but nevertheless the calculated phonon τ_{ph} exhibits a simple linear dependence on thickness.

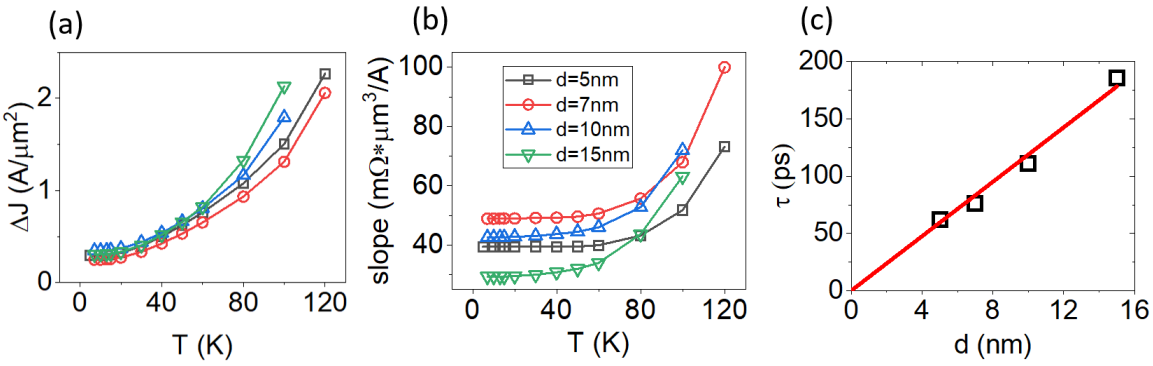

Figure 2.7: (a) Temperature dependence of thermal broadening (ΔJ) of Pt wires with different thickness on sapphire substrate. (b) Temperature dependence of slope of Pt wires with different thickness on sapphire substrate. (c) Dependence of the phonon relaxation time τ_{ph} on the thickness of Pt on sapphire, determined from the data at $T = 5$ K (symbols), and linear fit with zero intercept (line).

We fabricated 1 μm-long, 500 nm-wide Pt wires with thicknesses $d = 5$ nm, 7.5 nm, 10 nm, and 15 nm on sapphire substrate, and measured their $R(I)$ dependences at temperatures between 5 K and 295 K. All the $R(I)$ curves were well fitted with a with linear function convolved with the Gaussian, allowing us to determine the slope

and broadening ΔJ, as discussed in previous sections [Figs. 2.7(a),(b)].

The temperature dependences of both parameters are qualitatively similar to those observed for Pt on Si, with some deviations consistent with the smaller effects of interface scattering. In particular, for Pt on Si, the dependence $\Delta J(T)$ was linear for $d = 5$ nm, and became increasingly curved for larger d. The curving was explained by the increasing contribution of electron scattering on thermal phonons, which reduces the energy acquired by electrons between the scattering events. For Pt on sapphire, the effects of interfacial scattering are smaller, i.e. the relative contribution of thermal phonons to scattering is larger. Accordingly, $\Delta J(T)$ exhibits strong curving for all the studied Pt wires on sapphire [Fig. 2.7(a)].]

The slopes of $\Delta J(T)$ exhibit a generally nonmonotonic dependence on d, similarly to Pt on Si. We used these data and Eq.(2.6) to determine τ_{ph}. The latter exhibits a linear dependence on the Pt thickness with zero intercept, as shown in Fig. 2.7(c) for $T = 5$ K. The characteristic values of τ_{ph} are larger for Pt on sapphire than for Pt on Si. This is consistent with the larger sound speed in sapphire (10 km/s vs 8 km/s in Si). The higher sound speed in sapphire results in a larger acoustic mismatch between Pt and substrate, resulting in a smaller average transmission coefficient. The effect is larger than may be naively inferred from the modest difference between the sound velocities, because of the large range of wavevectors of phonons experiencing a total internal reflection.

2.10 Dependence of resistance on current in a resistive nanocontact

Our results for thin-film metallic wires on thermally conductive substrates suggest that nonequlibrium phonon distribution is generally formed in current-driven nanostructures characterized by efficient phonon relaxation. This hypothesis is supported

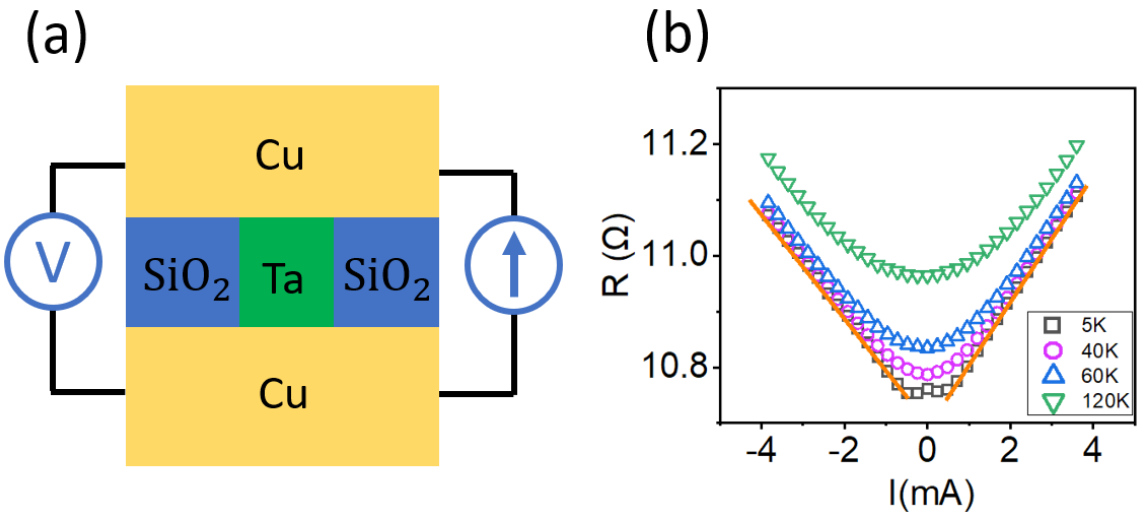

Figure 2.8: (a) Schematic of the resistive nanocontact, based on a 70-nm Ta(10) disk sandiched between two thick conducting electrodes, and the pseudo-four-probe measurement setup. (b) R vs I for the studied nanocontact, at the labeled values of temperature. The straight lines are guides for the eye.

by measurements of R vs I for a resistive nanocontact - a nanostructure whose geometry and thermal dissipation mechanisms are completely different from those of thin-film wires. The studied nanocontact is shown schematically in Fig. 2.8(a). It consists of a circular Ta(10) disk with a 70 nm diameter, sandwiched between a micrometer-scale Cu(50) bottom lead, and Cu(100) top lead. The electrical leads are separated by a SiO_2(15) insluating layer. The nanostructure was fabricated using a multi-step e-beam lithography process we developed for the studies of current-induced magnetization dynamics in magnetic nanostructures, and described in detail in multiple publications [69]. The resistance of the nanocontact is measured in the pseudo-four-probe geometry, with current and voltage contacts attached to the opposite sides of the Cu leads, as shown in the schematic.

In addition to the contribution of 4 Ω of the bulk Ta resistivity, estimated based on the separately measured resistivity of sputtered $\beta - Ta$ of about 1500 nΩ·m, the measured resistance of 10.8 Ω at 5 K comprises the interfacial resistance of Ta/Cu interfaces, which is expected to be high because of the large crystalline and band

structure mismatch between Ta and Cu, and also a contribution from the Cu leads, non-negligible in the pseudo-four-probe geometry. Our prior studies of similar magnetic spin-valve nanopillars suggest that the latter is about 1 Ohm.

Altogether, the resistance of the studied nanocontacts is likely dominated by the Ta(10) layer and its interfaces, which are also expected to provide a dominant contribution to the current-induced phonon generation. Meanwhile, the thick highly conductive Cu leads provide efficient thermal dissipation. According to our analysis, if the escape of phonons from the Ta layer into the Cu leads is faster than their thermalization, a linear dependence of resistance on current is expected. Indeed, a linear dependence $R(I)$ is observed for the studied nanocontact at T=5 K [Fig. 2.8(b)]. The linear dependence becomes increasingly smeared out at higher temperatures, consistent with the thermal broadening mechanisms discussed for thin-film wires in previous sections.

2.11 COMSOL simulation of Joule heating

To eliminate the possibility that the linear dependence of Pt wire resistance on current, observed in our experiments at cryogenic temperatures, can be explained by Joule heating, we performed simulations of current-dependent temperature distribution in Pt wires utilizing the COMSOL Multiphysics software. To reproduce $R(I)$ measured in the experiment at $T = 300$ K, we introduce boundary thermal conductivity $1 \times 10^8\ K \cdot m^2/W$ at the interface between sample and substrate, which accounts for imperfect thermal contact and the effects of acoustic mismatch on thermal conductivity discussed below. We note that the COMSOL simulation is based on the quasi-equilibrium (thermalized) approximation for the phonon distribution underlying the Joule heating law, and diffusive approximation for the heat flow underlying the Fourier's equation.

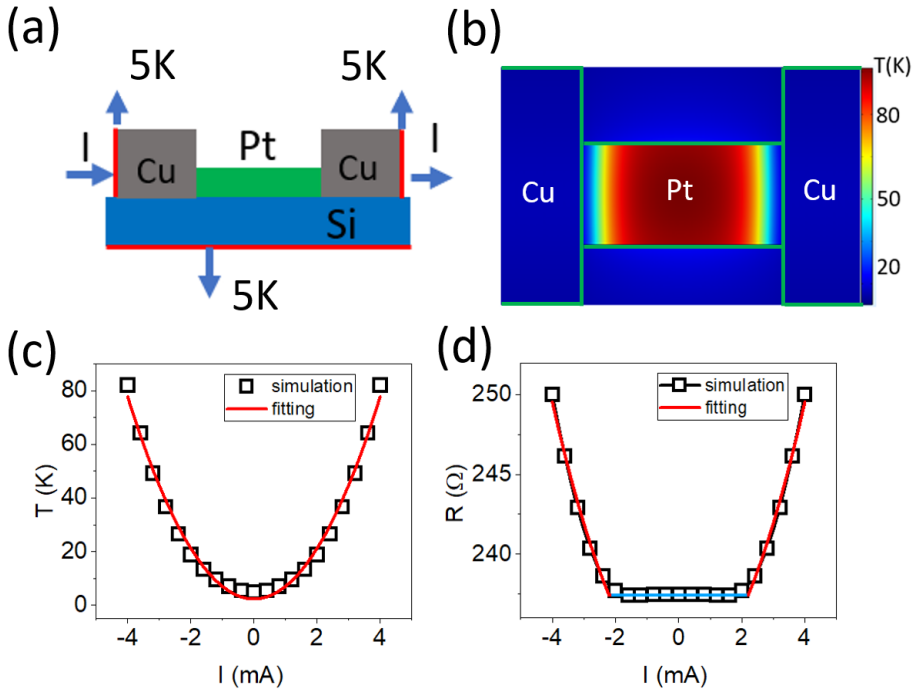

Figure 2.9: COMSOL simulations of Joule heating at temperature $T = 5$ K. (a) Schematic of sample configuration used in the simulation. The simulated dimensions of the Pt wire are 1μm $\times$500 nm $\times$5 nm. (b) Top view of the pseudocolor map of the calculated temperature distribution of the structure shown in (a), at current $I = 4$ mA. (c) Average sample temperature vs current. The curve is a fitting with a quadratic function. (d) Sample resistance vs current, determined from the calculated current-dependent temperature distributions such as shown in panel (b), and the measured dependence of resistivity on temperature. Blue line is $R = 229.6$ Ω, and the red curve is a fit of the $I > 2.2$ mA data with the quadratic function.

The simulated configuration, including the Pt wire, Cu leads and the Si substrate, closely matches the experimentally studied geometry, as illustrated in Fig. 2.9(a). A top view of the temperature distribution calculated at current $I = 4$ mA is shown in Fig. 2.9(b). It is worthy to notice that since compared to Pt, the Cu leads are much thicker and has much smaller resistivity, the heating in Cu leads is much smaller than the Pt wire. The highest calculated temperature, near the center of the wire, is 90 K at this current. Based on the measured $R(T)$ dependence, the sample resistance is expected to increase by less than 13 Ω at $I = 4$ mA, which is inconsistent with the increase of 40 Ω observed in the experiment. Figure. 2.9(c) shows the calculated de-

pendence of the average temperature in the Pt wire on current. This dependence is precisely fitted by the quadratic function, in agreement with the qualitative analysis in previous sections. Combining the calculated current-dependent spatial distribution of temperature with the measured dependence of resistivity on temperature, we obtain the dependence of sample resistance on current expected for Joule heating. The calculated current-dependent sample resistance is constant at small bias $I < 1.8$ mA, because resistance is almost temperature-independent at $T < 20$ K, and is well approximated by a quadratic function at $I > 2.2$ mA [Fig. 2.9(d)]. This result is inconsistent with the experimental observation of a linear dependence of resistance on current, confirming that the Joule heating approximation is inapplicable to the studied system at cryogenic temperatures.

2.12 Estimation of phonon escape time from the acoustic mismatch

We estimate the phonon escape time from Pt into the Si substrate using quasi-ballistic phonon transport approximation, which is justified by the small thickness of the studied Pt wires. The escape time is determined by the phonon scattering at the Pt/Si interface, which can be analyzed using the theory of acoustic mismatch [70]. For an acoustic wave incident from Pt at an angle θ_1 and refracted into Si at an angle θ_2 related to θ_1 by Snell's law [Fig. 2.10 (a)], the transmission coefficient is

$$\alpha = \frac{\frac{4D_2c_2}{D_1c_1} \cdot \frac{cos\theta_2}{cos\theta_1}}{(\frac{D_2c_2}{D_1c_1} + \frac{cos\theta_2}{cos\theta_1})^2}. \tag{2.7}$$

Here, c is the speed of sound, and D is the mass density, with the subscript "1" used for Pt, and "2" - for Si. The escape time can be then estimated as $\tau = \frac{2d}{\alpha c_1}$. Since the speed of sound in Si is higher than in Pt, transmission is possible only at

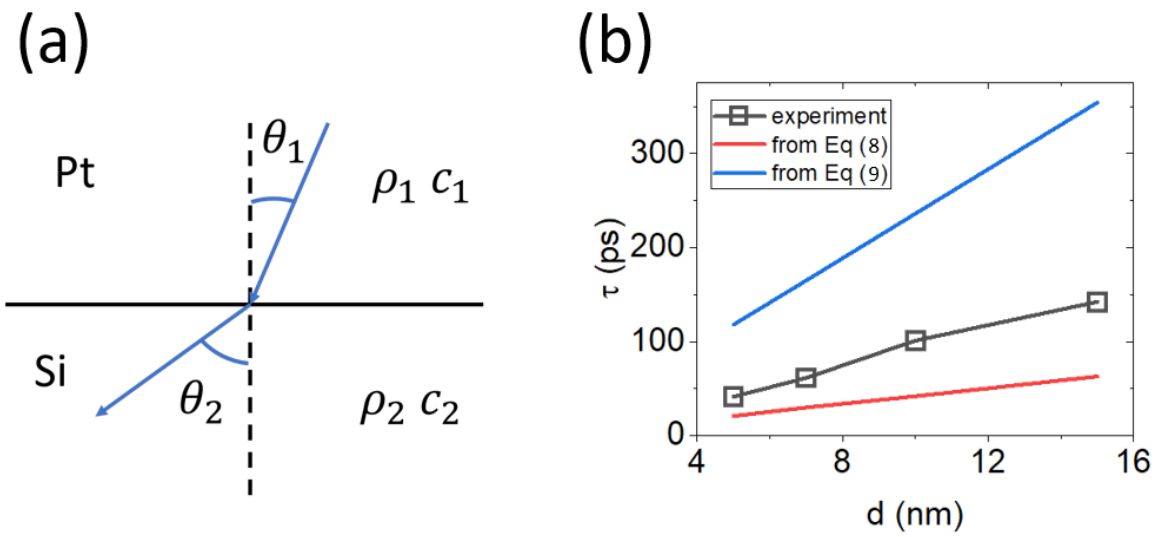

Figure 2.10: (a) Schematic of the configuration used in the acoustic mismatch calculation. Phonons are generated in the Pt layer and are scattered at the Pt/Si interface. The probability of transmission into the Si substrate determines the escape rate. (b) Comparison between the phonon relaxation time of Pt derived from experiment with relaxation time calculated with acoustic mismatch vs Pt thickness d. The experimentally determined dependence $\tau_{ph}(d)$ is between the values of τ_{esc} obtained in two different limits of phonon momentum distribution considered in the acoustic mismatch calculations, as shown by blue and red curves.

incidence angles smaller than the critical angle θ_c for the total internal reflection. We note that the average transmission probability exhibits a strong dependence on the momentum distribution of phonons. The distribution can be calculated with Boltzmann equation, which is beyond the scope of this work. Instead, we consider two limiting approximations. First, we assume that the momentum distribution of the generated phonons is confined to the plane of incidence shown in Fig. 2.10(a), and is isotropic in this plane. The average phonon transmission coefficient is then

$$\bar{\alpha} = \frac{\frac{\int_0^{\theta_c} \alpha\theta_1 d\theta_1}{\theta_c}}{\frac{\frac{\pi}{2}}{\theta_c}} = \frac{\int_0^{\theta_c} \alpha\theta_1 d\theta_1}{\frac{\pi}{2}} \tag{2.8}$$

For Pt(5) on Si, the average phonon escape time, estimated based on Eq. (2.8), is $\tau_{esc} = \frac{2d}{\bar{\alpha}c_1}$=21 ps. This estimate neglects imperfections at the Pt/Si interface that produce an additional acoustic barrier reducing the transmission. Thus, this estimate

provides a lower bound for the phonon escape time from Pt. For Au(5) on Si, similar analysis gives $\tau_{esc} = 15$ ps.

For the second limiting estimate, we assume that the distribution of the momenta of the generated phonons is isotropic in three dimensions, so the transmission probability needs to be averaged over the solid angle. In this limit, the average phonon transmission coefficient is

$$\bar{\alpha} = \frac{\int_0^{2\pi} \int_0^{\theta_c} \alpha sin(\theta)\, d\theta d\phi}{2\pi} \tag{2.9}$$

For Pt(5) on Si, the average phonon escape time estimated based on Eq. (2.9) is $\tau_{esc} = \frac{2d}{\bar{\alpha} c_1}$=118 ps. As shown in Fig. 2.10(b), the phonon relaxation time determined from the experiment lies between the two limiting values of escape times calculated as described above. More precise matching between the experiment and the acoustic mismatch calculation requires a more detailed quantitative analysis of the momentum distribution of the generated phonons. For Au(5) on Si, similar analysis based on the assumption of spatially isotropic phonon momentum distribution gives τ_{esc}=75 ps, less than half of the experimental relaxation time. As mentioned above, the discrepancy between the two values likely originates from the poor wetting of the substrate by Au, resulting in a reduced phonon transparency of the Au/Si interface.

2.13 Estimation of phonon scattering time

Phonons generated by current do not become thermalized if the thermalizing scattering is slower than relaxation. We can estimate the phonon scattering time based on the known phonon average mean free path, $l \approx 1$ μm at 300K for Pt [71, 72, 73], and the sound velocity $c = 2.6 \times 10^3$ m/s, giving $\tau_{sc} = l_{ph}/c = 3.8 \times 10^{-10}$ s. Since not all phonon-phonon scattering is inelastic, this estimate gives a lower bound on the phonon thermalization time. Nevertheless, the estimated value of τ_{sc} is significantly

larger than the estimated phonon escape time, confirming that the nonequilibirum phonon distribution generated in the studied microwires by current does not thermalize even at room temperature.

2.14 Nonlinear dependence of resistance on large driving current

The general expression for $\rho(J)$, Eq.(2.6) is

$$\rho(J) = \frac{\rho(0)}{1 - \tau_{ph}\sigma_{e-ph}J/e}. \tag{2.10}$$

This is a nonlinear dependence that can be approximated by a linear dependence When driving current is small, the first order expansion gives

$$\rho(J) \approx \rho(0)(1 + \tau_{ph}\sigma_{e-ph}J/e). \tag{2.11}$$

only at sufficiently small currents [Eq.(2.6)]. Note that the slope of the dependence Eq.(2.11) valid at small currents uniquely defines the entire nonlinear dependence Eq.(2.10), without any additional fitting parameters. This provides an independent test for the validity of the proposed interpretation and analysis.

The significance of the nonlinearity is determined by the value of $\tau_{ph}\sigma_{e-ph}J/e$, or equivalently the value of $(R(I)/R(0) - 1)$. For the Pt on Si data discussed above, the largest value of $(R(I)/R(0) - 1) = 0.17$ was reached for the Pt(4) wire at $I = 4$ mA at $T = 5$ K. The corresponding nonlinear relative correction to resistance is $0.17^2 = 0.03$, too small to be noticeable in these data. On the other hand, for the Pt(5) wire on SiO_2 discussed above, $(R(I)/R(0) - 1) = 0.7$ at $I = 2$ mA, so the nonlinearity is much more noticeable in Fig. 2.6(c)

Here, we show that the nonlinear dependence $R(I)$ becomes apparent at large

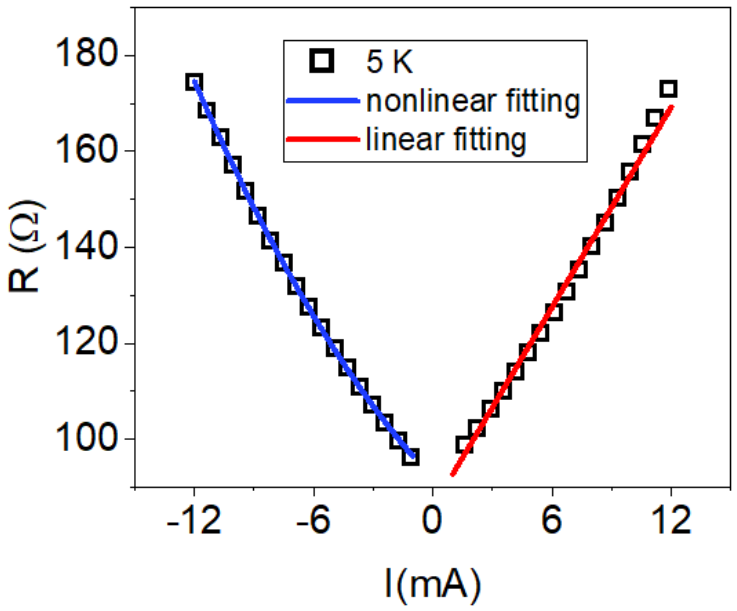

Figure 2.11: (a) Symbols: Dependence of resistance on driving current for the 1μm-long, 500 nm-wide Pt(7) wire on Si at 5 K. Red line is the fitting of the $I > 1$ mA data with Eq. (2.11). Blue curve is the fitting of the $I < -1$ mA data with Eq. (2.12.)

driving currents even for Pt on Si, and that it can be precisely fitted with Eq. (2.10) without any additional parameters. We use a 1μm-long, 500 nm-wide Pt(7) wire on Si substrate as an example [Fig. 2.11]. The measured dependence is symmetric with respect to the current direction. We use the two different branches in this Figure, $I < 0$ and $I > 0$, to illustrate the nonlinear effects. We fit only the data at $|I| > 1\ mA$, to avoid the complications associated with small-current broadening effects discussed above.

At large driving currents, the dependence $R(I)$ clearly becomes nonlinear, as illustrated by the poor linear fit shown by the red line for the $I > 0$ data in Fig. 2.11. For small nonlinearity, we expand Eq. (2.10) to the second order in J,

$$\rho(J) \approx \rho(0)(1 + \tau_{ph}\sigma_{e-ph}J/e + (\tau_{ph}\sigma_{e-ph}/e)^2 * J^2). \tag{2.12}$$

Fitting using this dependence, without any additional fitting parameters, provides excellent agreement with the data, as shown by the blue curve for the $I < 0$ data in

Fig. 2.11.

In previous sections, we focused on the linear regime at smaller currents, for two main reasons. First, the observed linear dependence provided a stark contrast with the Joule heating picture, allowing us to unambiguously assert that the latter is inapplicable to the studied system. Second, we kept the driving currents within a comfortable range, where the effects of heating and electromigration were insufficient to damage the studied samples.

2.15 Estimation of electron-phonon scattering cross-section

The electron-phonon scattering crossection σ_{e-ph} determines the relationship between the population of phonons and their contribution to resistivity, as follows. According to the Matthiessen's rule for the electron mean path ($1/l_e = 1/l_{e,0} + n_{ph}\sigma_{e-ph}$). Here, $l_{e,0}$ is the mean free path in the absence of phonons, and σ_{e-ph} is understood as the average scattering cross-section over the phonon distribution. Using the Drude formula $\rho = \frac{m^* v_F}{ne^2 l_e}$, we obtain

$$\rho(n_{ph}) = \rho(0) + \frac{m^* v_F n_{ph} \sigma_{e-ph}}{ne^2}, \tag{2.13}$$

or in the differential form

$$\sigma_{e-ph} = \frac{ne^2}{m^* v_F} \frac{d\rho}{dn_{ph}} = \frac{ne^2}{m^* v_F} \frac{\partial\rho/\partial T}{\partial n_{ph}/\partial T} \tag{2.14}$$

We can use Eq. (2.14) to extract σ_{e-ph} from the temperature dependence of resistivity and the known thermal phonon distribution. For temperatures above the Debye temperature T_D, we can approximate $n_{ph} \approx 3n_{at}T/T_D$, so that

$$\sigma_{e-ph} \approx \frac{ne^2 T_D}{3n_{at}m^* v_F}\frac{\partial \rho}{\partial T}. \tag{2.15}$$

We are interested in the scattering cross section on large-momentum phonons generated by current, corresponding to the linear regime of $R(I)$ observed at sufficiently large currents, as discussed in the previous section. Large-momentum thermal phonons also dominate electron-phonon scattering in thermal equilibrium at high temperatures ($T > T_D$), due to the dominance of their phase volume over the small-momentum phonons. Thus, we can assume that the average scattering cross section on thermal phonons above the Debye temperature is similar to that on current-generated phonons in the linear $R(I)$ regime (at sufficiently large bias). We use the dependence $\rho(T)$ close to $T = 300$ K and Eq. (2.15) to obtain $\sigma_{e-ph} = 4.6 \times 10^{-22}\ m^2$ for Pt, and $\sigma_{e-ph} = 1.3 \times 10^{-22}\ m^2$ for Au.

Chapter 3

Transport and relaxation of current-generated nonequilibrium phonons from nonlocal electronic measurements

3.1 Motivation: the propagation and decay of the nonequilibrium phonons

As described in the previous chapter, at cryogenic temperature the phonon system in current driven nano/micro- devices can be far from equilibrium and the effect of current can't be characterized as an elevation of sample temperature. The nano-wire device investigated in the last chapter has the advantage of being easy for fabrication and giving clear proof of principle result. However, there are two main drawbacks. Firstly, it is hard to disentangle the phonon generation and detection process, since both process happens simultaneously in the same wire. Moreover, such structure could not provide further information about the propagation and relaxation of the

nonequilibrium phonons after generated in the wire. In this section, a nonlocal geometry is used, where we study phonons generated by current in a Pt nanowire, by measuring resistance of another nanowire separated from the first one by an insulating spacer. For thin spacer, the resistance varies almost linearly with current at cryogenic temperatures, while an additional quadratic contribution emerges for thicker spacers. These observations suggest a non-thermal distribution of current-generated phonons that relax via strongly nonlinear dynamical processes rather than few-phonon scattering. Our results provide insight into the nonequilibrium phonon dynamics at nanoscale, which may facilitate efficient heat management in electronic nanodevices.

3.2 Experimental setup for nonlocal measurement

We present nonlocal electronic measurements utilizing a phonon-detecting nanowire separated from the phonon-generating wire by an electrically insulating spacer. The separation between phonon generation and detection allows us to confirm non-thermal distribution of current-generated phonons. Our approach also allows us to characterize inelastic phonon scattering, and to elucidate its mechanisms.

Our samples were fabricated by e-beam lithography and sputtering. They consisted of two 7 nm-thick, 1 μm-wide and approximately 18 μm-long Pt nanowires fabricated on top of one another on undoped Si substrates, and contacted by Cu electrodes [Fig. 3.1(a)]. Their large length ensured that phonon escape into the electrodes was negligible. The wires were separated by an insulating amorphous SiO_2 spacer whose thickness d was varied between 5 and 100 nm. To generate phonons, dc current I_s was applied to the top wire. The resistance R_d of the bottom wire used as a phonon detector was simultaneously measured using lock-in detection with a small ac current $I_d = 10$ μA applied to this wire. Both wires were metallic with resistance

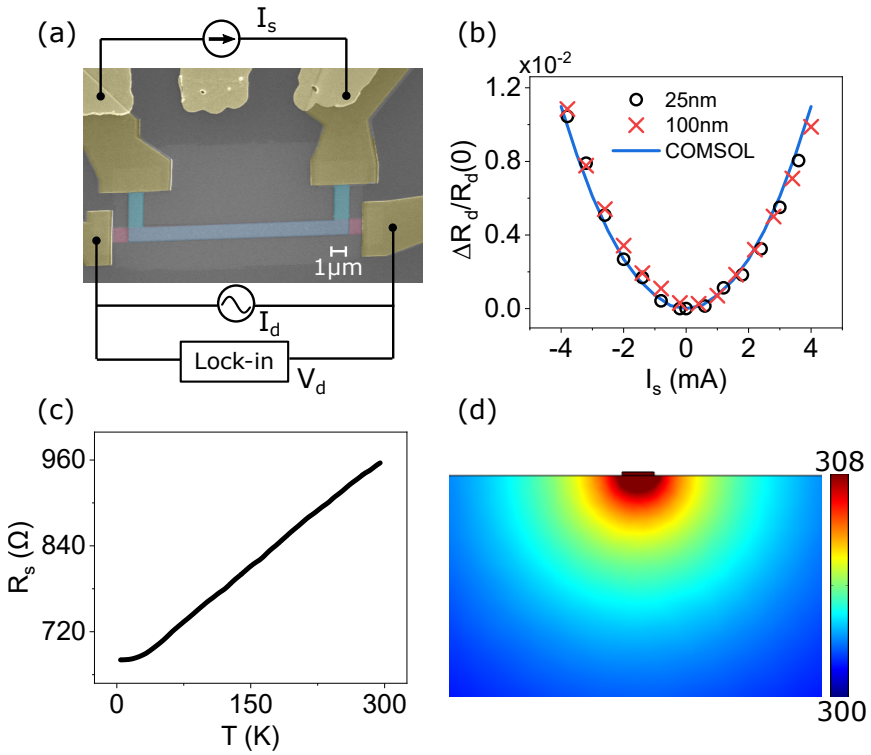

Figure 3.1: (a) Pseudocolor SEM image of one of the studied samples and measurement setup. (b) $\Delta R_d/R_d(0)$ vs I_s for $d = 25$ nm (circles) and 100 nm (crosses), at $T = 300$ K. Here, $\Delta R_d = R_d(I_s) - R_d(0)$. Curve: COMSOL simulation for $d = 100$ nm. The curve is well-approximated by a parabola. The result for $d = 25$ nm [not shown] is nearly identical. (c) R_s vs T at $I_s = 0$. The temperature dependence of R_d is similar. (d) Crossection of the temperature distribution calculated for $d = 100$ nm, at $I_s = 4$ mA and $T = 300$ K.

of about 800 Ω, with negligible contribution from contact resistance, as verified by separate 4-probe measurements. The resistance between the wires was at least 25 MΩ at cryogenic temperatures.

3.3 Room temperature result

Figure 3.1(b) shows $R_d(I_s)$ for two spacer thicknesses, $d = 25$ nm and 100 nm, at temperature $T = 300$ K (Room-temperature measurements for d < 25 nm were unreliable because ofelectron activation across spacer). To account for minor geometric differences leading to slightly different resistances, the data are offset and normalized

by $R_d(0)$. The two datasets closely follow the same quadratic dependence. This result is consistent with Joule heating and Fourier's law of heat diffusion. Indeed, the rate of Joule dissipation per unit source wire area is $w = d_{Pt}\rho j_s^2$, where d_{Pt} is its thickness, j_s is the current density, and ρ is resistivity. For the studied thin-film wires, the latter is dominated by scattering on the surfaces and impurities, as evidenced by its weak dependence on T [Fig. 3.1(c)], so to the lowest order the variation of ρ with j_s can be neglected.

The dissipated energy produces a heat flux $q = w$ flowing through the spacer and the sensing layer into the substrate and spreading over the characteristic depth z_c defined by the wire width, as illustrated by the COMSOL simulation, Fig. 3.1(d). In the 1d approximation, this can be modeled by a heat sink with the temperature T at the depth z_c below the sensing Pt wire. According to the Fourier's law, $q = -\kappa\nabla T$, where κ is the thermal conductivity of the substrate. We infer that the temperature of the detector wire $T_d = T + z_0 d_{Pt}\rho {j_s}^2/\kappa$ does not depend on the properties of the spacer, and is quadratic in I_s. Above the Bloch–Grüneisen temperature $\Theta_R \approx 50$ K [74], the resistance R_d of the detector wire is linear in T [Fig. 3.1(c)], so R_d is expected to be quadratic in I_s, in agreement with the data and the COMSOL simulations based on the Fourier's law [curve Fig. 3.1(b)].

Similar analysis predicts a quadratic $R_s(I_s)$, but with a coefficient that depends on the properties of the spacer. The resistivity of the Pt wires saturates below Θ_R [Fig. 3.2(c)]. Therefore, for measurements performed at $T \ll \Theta_R$, Joule heating should result in almost constant R_s at small I_s, crossing over to a quadratic dependence at large I_s, as illustrated by the COMSOL simulation [dashed curve in Fig. 3.2(a)].

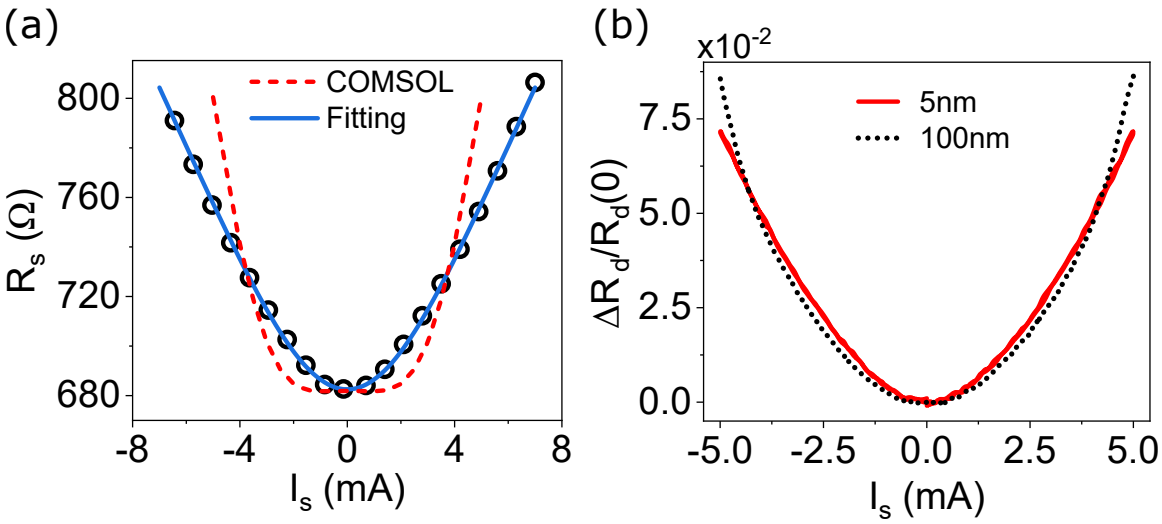

Figure 3.2: (a) R_s vs I_s for $d = 5$ nm at $T = 7$ K. Symbols: data, dashed curve: COMSOL simulation, solid curve: fit with the function $\gamma(\alpha, \Delta I_s, I_s)$ defined in the text. (b) $\Delta R_d/R_d(0)$ vs I_s for $d = 5$ nm (solid curve) and 100 nm (dashed), at $T = 7$ K.

3.4 Low temperature result

The measured $R_s(I_s)$ at $T = 7$ K [symbols in Fig. 3.2(a)] is qualitatively different from this prediction. Instead, it can be well-fitted by $R_s(I) = R_s(0) + \gamma$, where γ is a linear function of $|I_s|$ convolved with a Gaussian of width ΔI_s, $\gamma(\alpha, \Delta I_s, I_s) = \alpha \int dI |I| e^{-(I-I_s)^2/2\Delta I_s^2}/\sqrt{2\pi}\Delta I_s$ [solid curve in Fig. 3.2(a)] (Phonon generation due to electron-phonon scattering can be neglected, sinceresistance is dominated by scattering at the boundaries and defects even atlarge bias.). A similar result obtained in Ref. [75] was interpreted as evidence for the non-equilibrium distribution of current-generated phonons that cannot be described by an effective temperature. We now outline this interpretation. According to the Drude-Sommerfeld model, the rate of electron scattering in the source wire is proportional to I_s. Assuming that one phonon is generated in each electron scattering event, and that phonons escape into the substrate before they can thermalize, one obtains from the kinetic balance relation a linear dependence of current-generated phonon population on current [75]. Electron

scattering on these phonons leads to a linear dependence $R_s(|I_s|)$.

In this picture, phonon distribution must be non-thermal by energy conservation argument. The deposited electrical energy is quadratic in I_s, while the number of the generated phonons is proportional to $|I_s|$, and thus the average energy per phonon is also proportional to $|I_s|$. The same conclusion is obtained by considering the energy imparted by electric bias to each electron between the scattering events, which must be transferred to the phonon generated upon scattering. Smoothing of the weak singularity at $I_s = 0$, accounted for by the Gaussian of width ΔI_s, is explained by the reduced electron scattering cross-section on low-energy phonons.

For thermalized phonon distribution below the Debye temperature $\Theta_D = 240$ K of Pt, the average phonon energy $\langle\epsilon\rangle$ is linear in T, as follows from the Debye integral $\langle\epsilon\rangle \propto \int_0^\infty (e^x - 1)^{-1} kTx^3 dx / \int_0^\infty (e^x - 1)^{-1} x^2 dx \propto T$. Thus, for $T_s \propto I_s^2$, $\langle\epsilon\rangle \propto I_s^2$. At $T > \Theta_D$, the average energy of thermalized phonons is independent of T, as follows from the Raleigh-Jeans law for the thermal mode population, $n(\epsilon) = kT/\epsilon$. One can conclude that linear dependence of R_s on $|I_s|$ is inconsistent with thermal distribution of current-generated phonons.

3.5 Dependence on spacer thickness

Non-local measurements provide a test for this interpretation. If the distribution of phonons injected into the spacer is non-thermal, their inelastic scattering is expected to result in gradual thermalization. Thus, as the spacer thickness is increased, $R_d(I_s)$ may be expected to gradually transform from the linear dependence to the form expected for Joule heating. Indeed, $R_d(I_s)$ for $d = 5$ nm is close to the linear dependence $R_s(I_s)$, while the dependence for $d = 100$ nm is closer to parabolic [Fig. 3.2(b)]. As a consequence, at small I_s the normalized R_d is larger for $d = 5$ nm than for $d = 100$ nm, and smaller at large I_s, with a crossover at $|I_s| = 4$ mA.

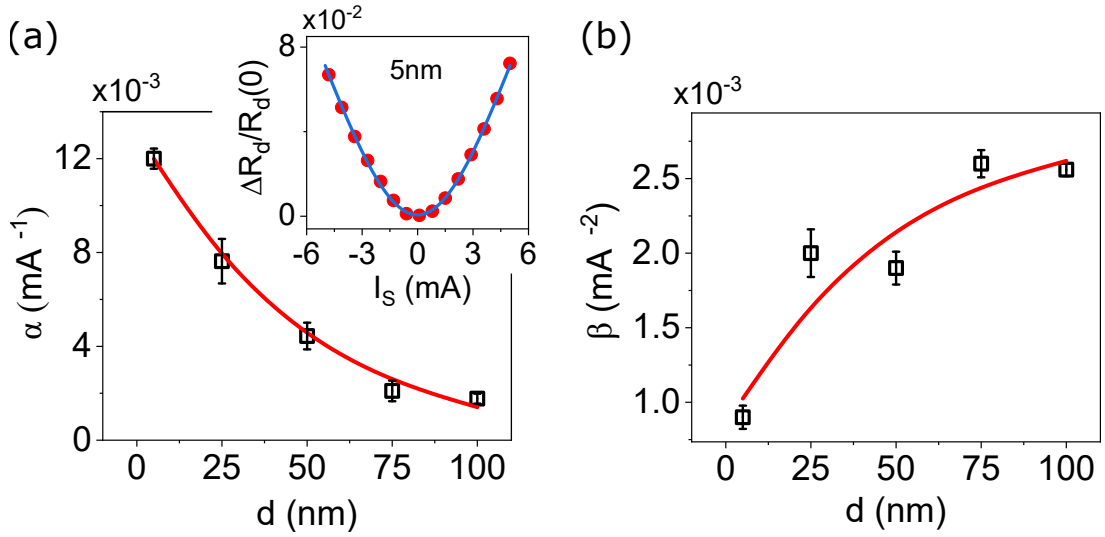

Figure 3.3: Dependence of the amplitudes α (a) and β (b) of the linear and the quadratic contributions to $R_d(I_s)$ on d, determined from fits such as shown in the inset for $d = 5$ nm, at $T = 7$ K. Curves are fits with the exponential dependences $\alpha_0 e^{-\ d/d_0}$ in (a), and $\beta_0 - \beta_1 e^{-d/d_0}$ in (b).

All the R_d vs I_s curves obtained at $T = 7$ K were well-approximated by a sum of the function $\gamma(\alpha, \Delta I_s, I_s)$ used for fitting the local measurements, with the same value of ΔI_s, and the quadratic function βI_s^2 [inset in Fig. 3.3(a)]. The first contribution describes the "primary" phonons generated in the source wire that diffuse to the detector without experiencing thermalizing inelastic scattering. The quadratic term was empirically found to provide a good fitting to the data. It reflects the presence of a "secondary" group of phonons generated due to inelastic scattering of the "primary" phonons.

The amplitude α of the linear contribution decreases, while the quadratic contribution increases with increasing d [Fig. 3.3]. The dependence $\alpha(d)$ is well-approximated by the exponential decay with decay length $d_0 = 44 \pm 2$ nm [curve in Fig. 3.3(a)]. The variability of the quadratic amplitude β is significantly larger. Nevertheless, it can be also fitted using the same exponential form describing its increase and saturation at large d [curve in Fig. 3.3(b)]. These results are consistent with increasing effects of inelastic scattering that involves annihilation of the primary phonons and generation

of the secondary phonons.

We note that $\beta(d)$ extrapolates to a finite value $\beta(0) = 8 \times 10^{-4}$ mA^{-2}, indicating that the secondary phonons are also generated at Pt/SiO_2 interfaces. We can estimate the probability P_{el} that the primary phonon is transmitted elastically across the Pt/SiO_2 interface, by using the extrapolated value $\beta(\infty) = 2.8 \times 10^{-3}$ mA^{-2}, which corresponds to all the primary phonons converted into secondary phonons in a thick spacer. Accounting for the two Pt/SiO_2 interfaces separating the source from the detector, we obtain $P_{el}^2 = 1 - 8/28$, i.e., $P_{el} = 0.85$.

Based on the energy conservation arguments discussed above, the density n_1 of the primary phonons and their average quasiparticle energy ϵ_1 are proportional to $|I_s|$. The quadratic term in the dependence $R_d(I_s)$ indicates that the density n_2 of the secondary phonons is quadratic in I_s, and thus their average quasiparticle energy ϵ_2 is independent of I_s. This implies that the secondary phonons generated at $T = 7$ K are not thermalized, since the average energy of thermalized phonons at $T \ll \Theta_D$ would be proportional to I_s^2 [see above].

3.6 Model for the thermalization of nonequilibrium phonons

To analyze inelastic scattering that results in the generation of secondary phonons, we consider the continuity equations in the relaxation time approximation, $\partial n_1/\partial t = -\nabla \cdot \mathbf{f}_1 - n_1/\tau_{in}$ for the primary phonons, and $\partial n_2/\partial t = -\nabla \cdot \mathbf{f}_2 + n_1\epsilon_1/\tau_{in}\epsilon_2$ for the secondary phonons. Here, $\mathbf{f}_{1,2}$ are the quasiparticle fluxes of the two phonon groups, and we used energy conservation to relate the secondary phonon generation to the annihilation rate $1/\tau_{in}$ of the primary phonons.

In the diffusive phonon transport approximation justified by the small phonon MFP $l_{el} \approx 5$ nm in amorphous SiO_2 at cryogenic temperatures [13, 76], $\mathbf{f}_{1,2} =$

$-D\nabla n_{1,2}$, where $D = v_{ph}l_{el}/3$ is the diffusion coefficient and v_{ph} is the phonon group velocity, which can be approximated by the sound velocity ≈ 4.5 km/s in amorphous SiO_2. Thus, we estimate $D \approx 7.5 \times 10^{-6}\mathrm{m}^2/\mathrm{s}$.

The phonon distribution in the spacer depends only on the normal coordinate z, defined to be directed into the substrate, with the origin located in the SiO_2 spacer at the boundary with the source wire. Assuming that the only phonon source is at $z < 0$, we obtain for the stationary state at $z > 0$

$$\begin{aligned} n_1(z) &= n_1^{(0)} e^{-z/\sqrt{D\tau_{in}}}, \\ n_2(z) &= n_1^{(0)} \frac{\epsilon_1}{\epsilon_2} + (n_2^{(0)} - n_1^{(0)} \frac{\epsilon_1}{\epsilon_2}) e^{-z/\sqrt{D\tau_{in}}} \end{aligned} \tag{3.1}$$

where $n_1^{(0)}$ ($n_2^{(0)}$) is the primary (secondary) phonon density at $z = 0$. These dependences are consistent with the observed exponential decay of α and the corresponding increase of β [Fig. 3.3(b)], allowing us to estimate the inelastic scattering time $\tau_{in} = d_0^2/D = 270$ ps. The inelastic scattering length, defined as the length of the phonon path between inelastic scattering events, is $l_{in} = \tau_{in} v_{ph} = 1.2$ μm. Such a large value is promising for the possibility to transport non-thermalized phonons over significant distances, by utilizing materials with large phonon MFP.

3.7 The mechanisms of secondary phonon generation

We now analyze the mechanisms of secondary phonon generation. Inelastic scattering is usually described in terms of three- and four-phonon processes [77, 78, 79]. In these processes governed by quasiparticle energy and momentum conservation, the average energies of the generated phonons linearly scale with the energies of the annihilated phonons, which is inconsistent with our results. A cascade of three-phonon

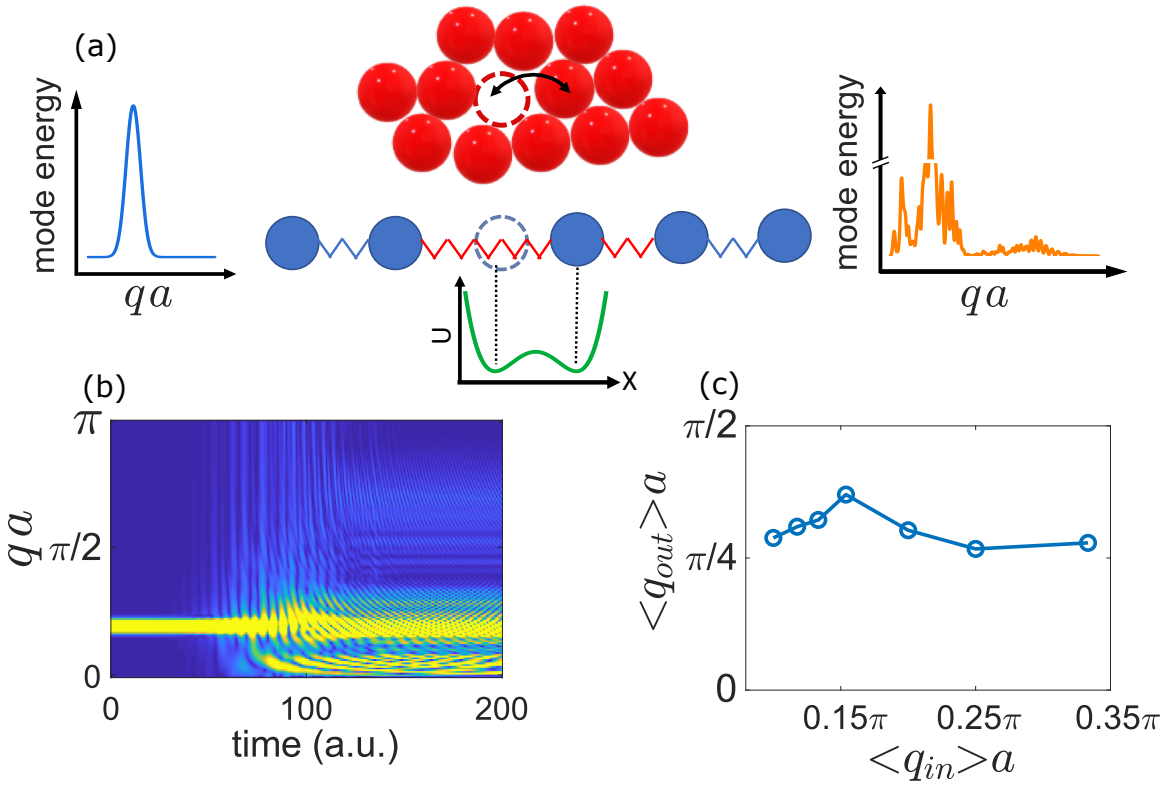

Figure 3.4: (a) Schematic of the 1d simulation of inelastic phonon scattering by a strongly anharmonic defect as a chain of masses connected by springs. Top inset: example of a strongly anharmonic defect associated with a bistable atomic position in amorphous solid. Bottom inset: potential vs displacement for the mass n_0 attached to the anharmonic springs. Left (right) inset: mode energy vs wavevector times the lattice constant for the phonon wavepacket before (after) scattering. (b) Wavevector distribution vs time during phonon scattering on the defect. (c) Average wavevector of the generated phonon modes vs the incident phonon wavevector, obtained by cutting out twice the Guassian width around the wavepacket center after scattering.

processes could result in effective thermalization. However, this cannot explain our observation of similar behaviors over a wide range of spacer thicknesses. Damping of long-wavelength acoustic waves can be described by the diffusive Akhiezer mechanism associated with the strain-induced modulation of phonon spectrum [80]. However, this quasi-adiabatic mechanism is not applicable to high-energy nonequilibrium phonons generated at large electric bias.

Since inelastic scattering requires anharmonicity, but weak anharmonicity responsible for the few-phonon processes cannot account for our observations, we conclude

that secondary phonons are likely generated due to strongly anharmonic dynamics. Such dynamics may be related to the bosonic peak ubiquitous in the spectra of amorphous materials [81, 82, 83] and to the problem of phonon glass [84, 85], and may be associated with quasi-localized nonlinear defect states such as bistable atomic configurations [top inset in Fig. 3.4(a)], as well as interstitial impurities and incoherent interfaces [86, 87].

To model phonon scattering by a bistable defect, we consider a wavepacket propagating along a 1d chain of masses $n = 1..300$ connected to their neighbors by springs [Fig. 3.4(a)]. Masses $n = 1$ and 300 are also connected to avoid artifacts from boundary reflections. All the springs are linear with the same spring constant, except the two springs connected to the mass $n_0 = 150$ are described by the double-well potential energy $U(x) = -k_1x^2/2 + k_3x^4/4$, resulting in bistable equilibrium of mass n_0 [bottom inset in Fig. 3.4(a)].

Dynamics spanning both potential wells cannot be described in terms of the perturbative anharmonic expansion because of the saddle point of the potential at $x = 0$. Scattering of the wavepacket on the defect results in the generation of a broad range of modes throughout the entire Brillouin zone, Fig. 3.4(b), instead of the usual harmonics expected for weak anharmonicity [11]. Figure. 3.4(c) shows that the average wavevector of the generated modes remains almost constant when the center wavevector of the incident wavepacket is varied by more than a factor of 5, consistent with our experimental observations. This result indicates a breakdown of the perturbative picture underlying the concept of quasiparticles [phonons] [88], enabling nonresonant scattering not constrained by the usual quasiparticle momentum and energy conservation laws.

3.8 Phonon transport and relaxation in a crystalline MgO spacer

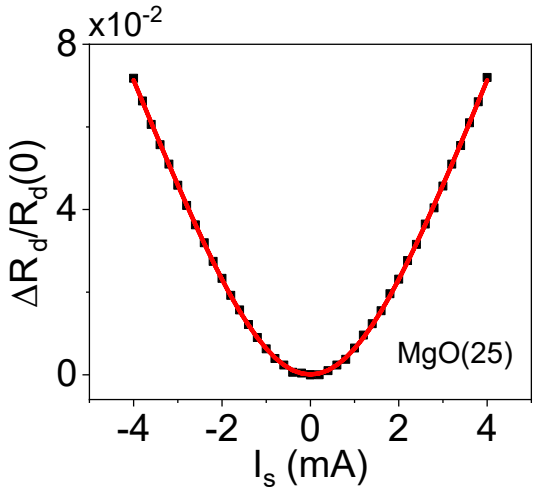

Figure 3.5: Symbols: $\Delta R_d(I_s)/R_d(0)$ vs I_s, for the sample that consists of two 7 nm-thick Pt nanowires separated by a 25 nm-thick crystalline MgO spacer, at $T = 7$ K. Solid curve: fitting with the superposition of the function $\gamma(\alpha, \Delta I_s, I_s)$, defined in previous sections, and the quadratic function βI_s^2.

The studies above focused on phonon diffusion and relaxation in amorphous SiO_2 spacer sandwiched between two Pt wires. Our observation of the quadratic contribution to the dependence $R_d(I_s)$, which emerges with increasing spacer thickness, was interpreted in terms of inelastic phonon scattering on strongly anharmonic defects that scrambles phonon momentum and energy conservation laws governing weakly anharmonic processes. In amorphous materials such as SiO_2, a significant density of such defects may be generally expected thanks to the local structural disorder. This raises the question whether the observed behaviors are general, and may be expected for the technologically relevant materials, or specific only to SiO_2 and perhaps other amorphous materials.

To address this question, we prepared an additional sample with the same structure and geometry as described above, but with a crystalline MgO spacer instead of amorphous SiO_2. This spacer was fabricated using the approach well-established in

the spintronics community, where MgO is extensively utilized as a tunneling barrier in magnetic tunnel junctions [89, 90]. The 25 nm-thick MgO spacer layer was deposited on top of the bottom Pt wire by high-vacuum rf sputtering in ultrahigh-purity Ar. After the top Pt wire was deposited on top of the MgO spacer, the sample was annealed in vacuum at 350° C for 1 hour, which resulted in the crystallization of MgO layer into the rocksalt structure [91, 92]. An additional 1 nm-thick MgO spacer was also deposited between the Si substrate and the bottom Pt nanowire to prevent the diffusion of Si into Pt during the annealing. We verified that the resulting electronic properties of the Pt wires were similar to those in the samples with SiO_2 spacers.

The same nonlocal measurements as described in previous sections for SiO_2 spacers were performed for this sample at $T = 7$ K, as shown in Fig. 3.5. The dependence $R_d(I_s)$ is close to linear in $|I_s|$, with some smoothing at small I_s. It is clearly inconsistent with Joule heating, which is expected to exhibit a current-independent region at small I_s and a quadratic increase at larger I_s. These data are well-approximated by the superposition of the smoothed linear function $\gamma(\alpha, \Delta I_s, I_s)$ defined in previous sections and the quadratic function βI_s^2, the same form as the fitting performed for SiO_2 spacers. This result suggests that the behaviors reported above are likely quite general to both crystalline and amorphous spacers.

Both the linear amplitude $\alpha = 11 \times 10^{-3}$ mA^{-1} and the quadratic amplitude $\beta = 2.16 \times 10^{-3}$ mA^{-2} are larger than the corresponding values $\alpha = 7.6 \times 10^{-3}$ mA^{-1}, $\beta = 2 \times 10^{-3}$ mA^{-2} for the same-thickness SiO_2 spacer. We speculate that both the elastic phonon MFP and the inelastic scattering time in crystalline MgO are is likely larger than in amorphous SiO_2, due to the smaller density of structural defects including the strongly anharmonic defects mediating phonon relaxation. According to Eq. (3.1) in previous sections, this should result in a slower decay of the "primary" phonons into the "secondary" ones. This can explain the larger linear amplitude, but not the larger quadratic amplitude. Thus, scattering at the Pt/spacer interfaces

likely plays an important role. Detailed measurements of the dependence on MgO spacer thickness, and comparison to the corresponding data for SiO_2, are necessary to unambiguously establish the mechanisms underlying these differences.

3.9 Dependence on experimental temperature

In previous sections, we have analyzed the dependences $R_d(I_s)$ at room temperature, and showed that they are consistent with the Joule heating approximation and Fourier's law of heat diffusion. Meanwhile, the results obtained at $T = 7$ K are inconsistent with Joule heating, and were interpreted instead in terms of the highly non-thermal distribution of current-generated phonons. These results raise the question about the mechanism of transition between these two qualitatively different phonon generation regimes.

The effects of temperature on the local current-dependent resistance variations were studied in detail in Ref. [75]. It was shown that the width ΔI_s, which describes the broadening of the linear dependence $R_s(|I_s|)$, linearly increases with $T > 20$ K. The function $\gamma(\alpha, \Delta I_s, I_s)$ introduced above can be approximated by a quadratic dependence in the range of current $|I_s| < \Delta I_s$, and by the linear dependence at $|I_s| > \Delta I_s$. At cryogenic temperatures, ΔI_s is significantly smaller than the range of applied currents, so the variations of R_s are dominated by the linear dependence.

At room temperature, ΔI_s is extrapolated to become slightly larger than the range of applied currents, so the entire measured dependence $R_s(I_s)$ [and consequently $R_d(I_s)$] is expected to be well-approximated by a quadratic form consistent with Joule heating. This result can be expected based on the general statistical arguments. Indeed, electric field applied to metallic nanowire biases the electron distribution, opening inelastic electron scattering channels that result in the generation of non-thermal phonons. At sufficiently high temperatures, this bias becomes smaller than

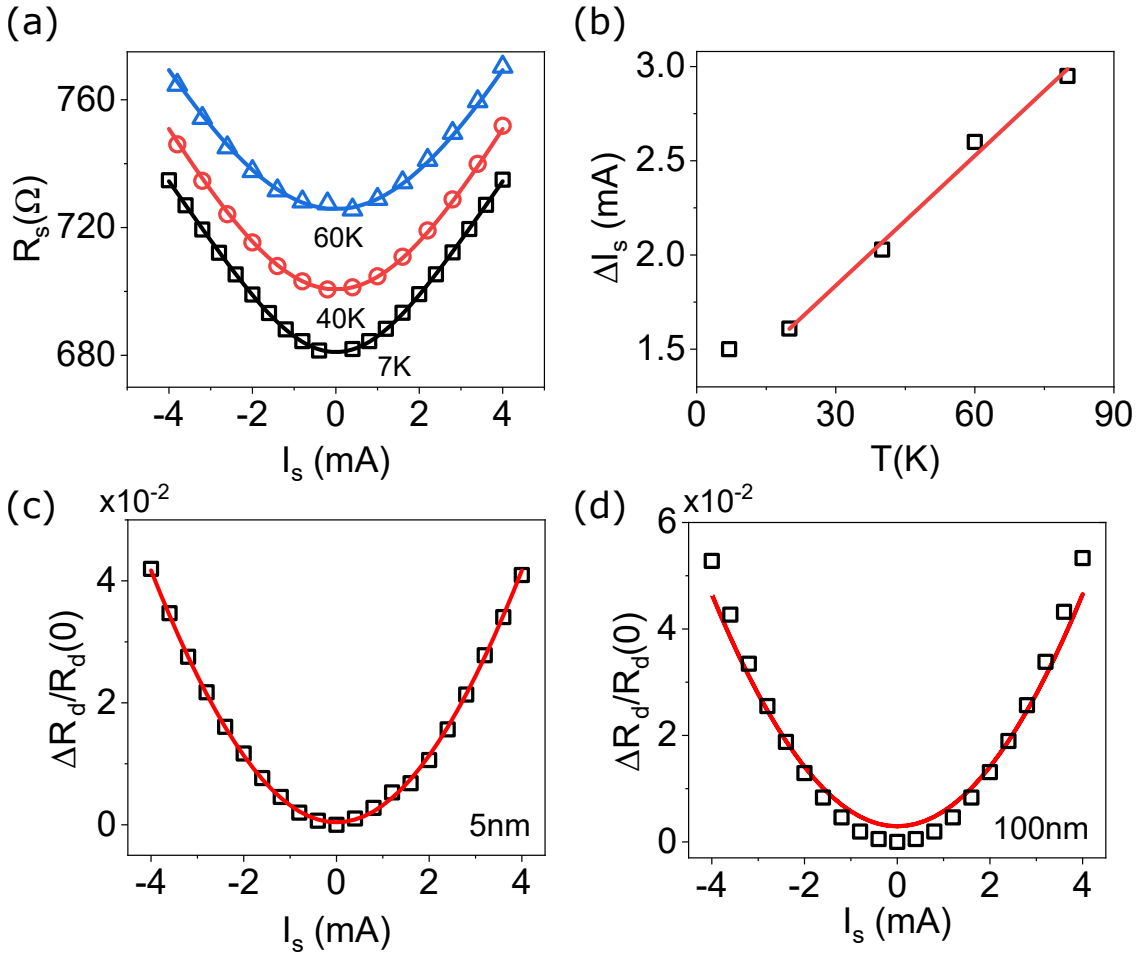

Figure 3.6: (a) $R_s(I_s)$ for $d = 5$ nm, at the labeled values of T. Solid curves are best fits with $\gamma(\alpha, \Delta I_s, I_s)$. (b) ΔI_s vs T extracted from the fits of $R_s(I_s)$. The solid line is a linear fit for $T > 15$ K. (c), (d) $\Delta R_d(I_s)/R_d(0)$ vs I_s for $d = 5$ nm (c) and 100 nm (d), at $T = 60$ K. Curves are calculations using the function $\gamma(\alpha(T = 7K), \Delta I_s(T = 60K), I_s) + \beta(T = 7K)I_s^2$.

the thermal broadening of the electron distribution. By the principle of detailed balance, the distribution of phonons generated by scattering of almost thermalized electrons is also almost thermalized, i.e., it can be well-approximated as Joule heat. Our non-local measurements allow us to independently test this picture by eliminating possible artifacts from the electrical biasing in local measurements, and to explore the role of thermal phonons in phonon transport and relaxation. We start with the local measurements of $R_s(I_s)$ to confirm the previously reported behaviors and determine the relevant parameters. As shown in Fig. 3.6(a) for several values of T,

as the temperature is increased, the R_s vs I_s curves become increasingly smoother at small I_s, but the linear dependence at larger I_s remains evident at the highest shown temperature $T = 60$ K. All of these data are well-approximated by the function $\gamma(\alpha, \Delta I_s, I_s)$, with the value of ΔI_s linearly increasing with $T > 20$ K [Fig. 3.6(b)], and the value of α remaining almost independent of temperature. These results are consistent with the findings of Ref. [75].

We note that thermal broadening provides an energy scale allowing one to estimate the average energies of non-equilibrium phonons generated by current, as follows from the above discussion of the thermal broadening mechanisms. In particular, the slope of the dependence $\Delta I_s(T)$ in Fig. 3.6(b) is $\frac{d\Delta I_s}{dT} \approx 0.03$ mA/K. According to our interpretation, $I = \Delta I_s$ is the crossover bias where the characteristic energy of the generated non-equilibrium phonons is similar to the thermal energy of electrons, i.e. $\langle \epsilon_1(I_s) \rangle / I_s = k_b / \frac{d\Delta I_s}{dT}$, where k_B is the Boltzmann constant, which amounts to about 3 meV per mA of bias current. This implies that the non-equilibrium effects described in this work could be observed at room temperature at $I_s > 9$ mA for the studied Pt nanowires. In our measurements, we limited the applied current to smaller values in order to avoid current-induced damage.

These results also allow us to estimate the characteristic energy of secondary phonons generated in the SiO_2 spacer. The dependence of the linear amplitude on the spacer thickness is $\alpha(d) = 1.3 \times 10^{-2} e^{-d/d_0}$ mA^{-1}, while for the quadratic amplitude varies as $\beta(d) = 2.8 \times 10^{-3} - 2.0 \times 10^{-3} e^{-d/d_0}$ mA^{-2}. Here, $d_0 = 44$ nm is the decay length. Assuming that the electron scattering crossection on these phonons is similar to that for the primary phonons, this implies that at $I_s = 1$ mA, an average of $1.3 \times 10^{-2} / 2.0 \times 10^{-3} = 6.5$ secondary phonons are generated by annihilation of one primary phonon. Thus, based on the above estimates of $\langle \epsilon_1(I_s = 1mA) \rangle$, $\langle \epsilon_2 \rangle = 0.5$ meV. This value is likely an underestimate, because it would place the secondary phonons in the spectral range where electron scattering crossection on

these phonons is small, so they would not provide a significant contribution to the current-dependent resistance. Nevertheless, these estimates indicate that both the primary and the secondary phonons in SiO_2 are likely predominantly acoustic.

Several thermal effects may be expected in the nonlocal measurements. The thermal broadening of the electron distribution in the source wire results in the increasing broadening of phonon distribution, as reflected by the increase of the broadening parameter ΔI_s in the local measurements. In addition, scattering of the current-generated phonons on thermal vibrations may influence the transport properties and the relaxation of phonons at the Pt/SiO_2 interfaces and in the SiO_2 spacer

Figures 3.6(c) and (d) show the dependences $R_d(I_s)$ for $d = 5$ nm and 100 nm, respectively, at $T = 60$ K. The curves show the dependences calculated based on the temperature-dependent local measurements and the nonlocal measurements performed at $T = 7$ K. These calculations account for the thermal broadening in the source wire but not for the possible thermal effects on phonon propagation and relaxation. Specifically, the calculated dependence is the sum of $\gamma(\alpha(d), \Delta I_s(T = 60K), I_s)$ and $\beta(d)I_s^2$, with the same values of all the parameters as at $T = 7$ K, except for the increased value ΔI_s as determined from the local measurements.

For $d = 5$ nm, the calculated curve is in excellent agreement with the data [Fig. 3.6(c)]. This agreement provides further support for the validity of our interpretation and analysis of phonon generation and transport in the studied structures. It also indicates that the effects of thermal vibrations on phonon transport across the Pt/SiO_2 interfaces are negligible. In contrast, for $d = 100$ nm, the experimental dependence is significantly more curved than the calculated curve, indicating an increased efficiency of primary phonon relaxation into the secondary phonons. This result may be expected due to the decrease of the phonon diffusion coefficient associated with scattering of the current-generated phonons on thermal phonons. Additionally, thermal fluctuations may enhance activation of the strongly anharmonic

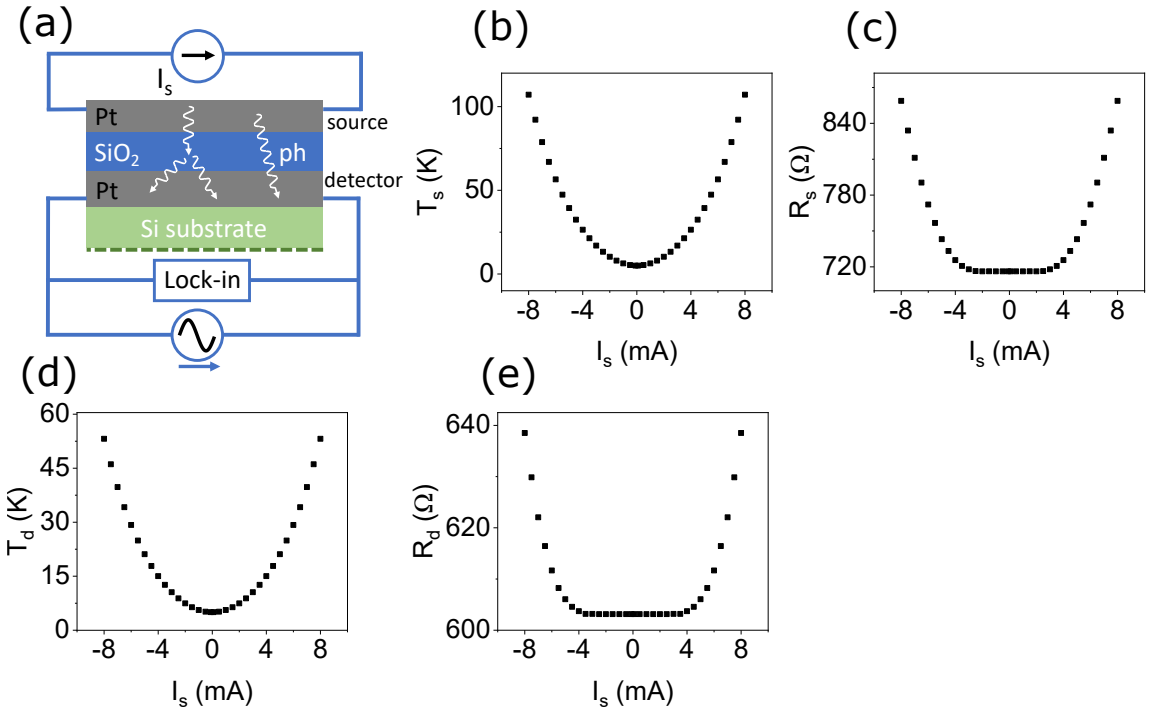

Figure 3.7: (a) Cross section view of the nonlocal measurement setup used in COMSOL simulation. (b) T_s vs I_s at 7K in simulation. (c) Simulated dependence of R_s on I_s (d) Simulated dependence of T_d on I_s (e) COMSOL simulated dependence of R_d on I_s

defects that likely provide the dominant mechanism for the phonon relaxation. Additional detailed experimental studies and calculations are necessary to fully elucidate the mechanisms of this effect.

3.10 COMSOL simulation

To further confirm that our observation in experiment can't be explained within the framework of diffusive heat transfer and Joule's heating picture. We performed COMSOL simulation. The structure in simulation is schematically plotted in Fig. 3.7(a), where two $1\mu m$-wide $18\mu m$-long, and $7nm$-thick Pt wires are separated by a SiO_2 insulator layer. The size of Si substrate is more than a magnitude larger than the wire length and the dependence of ρ_{Pt} on T measured in experiment is included in the simulation. In the simulation DC current is applied in the top(phonon generat-

ing) wire. The temperature and resistance of the two wires are calculated by solving coupled differential equations accounting diffusive heat transfer and Joule's heating via COMSOL.

As shown in Fig. 3.7(b) and (d), the DC current "heats" up the structure and the device temperature (T_s and T_d) quadratically increases with the DC current. Moreover, the fact that since the bottom wire is closer to heat sink, for the same I_s its temperature (T_d) should be lower than the top wire (T_s) is correctly captured in the simulation. The dependence of resistance of the two wires on I_d is shown in Fig. 3.7 (c) and (e). For small I_d, T_s (T_d) is in low temperature region where the impurity scattering dominates and ρ_{Pt} is independent on T. In this case, even though the T_s (T_d) quadratically increases with I_s, the R_s (R_d) stays constant. When the I_d is large, since in high temperature range the resistance linearly increases with temperature, both R_s and R_d should quadratically increase with I_s, which is correctly captured in COMSOL simulation. The qualitative inconsistency between the dependence of R_s and R_d on I_s in simulation and experiment, suggests that the observation in experiment is can't be explained by diffusive heat transfer and Joule's heating.

Chapter 4

Experimental demonstration and analysis of random field effects in ferromagnet/antiferromagnet bilayers

4.1 Ferro-/Antiferromagnetic heterostructure

From this section, we would like to disccus the nonequilibrium phenomenon in the second system , ferromagnet /antiferromagnet structure experiencing random interfacial coupling. The exploration of ferromagnet/antiferromagnet (F/AF) heterostructures started over 60 years ago with the discovery, by Meiklejohn and Bean, of exchange bias (EB) effect - asymmetry of the ferromagnetic hysteresis loop that emerges below a certain blocking temperature T_B [93]. EB can be utilized for "pinning" the magnetization of Fs, which has found extensive applications in magnetoelectronic sensors and memory devices [94, 95, 96, 96, 97]. A recent resurgence of interest in the fundamental properties of F/AF heterostructures has been motivated by the emergence of AF spin-

tronics - a research field that aims to take advantage of the vanishing magnetization of AFs, their high characteristic dynamical frequencies, and weak coupling to external fields to develop efficient, fast, and stable magnetic nanodevices [98]. While some of the implementations of such AF-based devices rely on standalone AFs [99, 100, 101], many others utilize auxiliary Fs, usually in F/AF heterostructures, to generate spin currents for nanodevice operation, detect the state of AFs, and/or directly control this state via exchange interaction [102, 103, 104, 105, 106, 107, 108].

Extensive studies of F/AF heterostructures have revealed complex behaviors that sensitively depend on a variety of experimental and material parameters, which could not be explained by naïve models assuming perfectly magnetically ordered materials and interfaces [109]. This has lead to the realization that inhomogeneous magnetization states are likely formed in AF and/or F to minimize the exchange energy at the F/AF interfaces. Several models have been developed to account for this possibility. For instance, some of the observed magnetic properties were attributed to the magnetic domain walls formed in AF to reduce the interfacial exchange energy [110, 111]. It was also proposed that spin glass-like magnetically disordered states can be formed near the F/AF interface [112, 113, 114].

Even atomic-scale imperfections can reverse the exchange interaction across the F/AF interface, which led Malozemoff [115] to suggest that the effects of this interaction can be approximated by an uncorrelated random effective field acting on AF at its interface with F. Analysis based on the extension of the Imry-Ma argument [116] suggested that as a result, AF breaks up into domains. This model predicted EB magnitude qualitatively consistent with the experimental observations. Extending this analysis to ultrathin AF films, Malozemoff also predicted a crossover to the "Heisenberg domain state" (HDS), wherein AF magnetic domains shrink to sizes below the AF domain wall width [117]. The magnetization of AF is then envisioned to become twisted everywhere, and the long-range magnetic ordering of AF is lost.

The implications of these predictions for the fundamental properties of F/AF heterostructures have so far received relatively little attention [118, 119]. Recent time-domain measurements of magnetization states in F/AF bilayers utilizing several common AF materials have revealed universal power law aging [120, 121, 122]. Aging was observed only for AF films with thickness below a certain material-dependent value. Thus, aging was attributed to the emergence of a HDS. Based on the analysis of the dependence of aging on the magnetic history and temperature, it was conjectured that in terms of the dynamical properties, the HDS is a correlated spin glass [122]. This conjecture was supported by measurements of ac susceptibility, which demonstrated that the temperature dependence of the dynamical response is consistent with the glass transition at the EB blocking temperature T_B [123]. In particular, the magnetization exhibited viscous dynamics above T_B and elastic dynamics below T_B, with viscosity varying by several orders of magnitude close to this temperature. These recent results highlighted the potential significance of the random-field effects proposed by Malozemoff, but have not directly demonstrated the existence of random effective exchange fields at F/AF interfaces.

If the effects of exchange interaction across the F/AF interface can be described by an effective random field exerted on AF, then its reciprocal effects on F can be similarly described by an effective random field. Indeed, the Heisenberg exchange interaction preserves rotational symmetry, and therefore the local exchange torques exerted across F/AF interface on AF should be opposite to the local torques exerted by AF on F. Theoretical studies have shown that random fields acting on Fs produce an inhomogeneous magnetization state, with the magnitude of deviations from the saturated state related to the external field by certain scaling exponents dependent on the system dimensionality [124, 125, 126].

Here, we present experimental characterization and analysis of effective exchange fields in Permalloy(Py)/CoO bilayers, one of the "classic" F/AF bilayer systems ex-

tensively studied in the context of EB. In the next section, we introduce our approach. In Section 4.3, we present measurements of the effects of the applied field on the magnetization states for different thicknesses t of Py, and show that our results for one of the field directions are inconsistent with the approximation of quasi-uniform effective exchange field produced by CoO. In Section 4.4, we present an analytical model for the effects of uncorrelated random field on 2d systems. In Section 4.5, we utilize a combination of scaling arguments and micromagnetic simulations to extend our analysis to the thin-film geometry of our experiment. In Section 4.6, we use the developed approach to show that our experimental results can be explained in terms of the uncorrelated effective random exchange field exerted on Py at its interface with CoO. We also analyze the temperature dependences of the characteristics extracted from our analysis, and show that they are consistent with prior measurements of similar systems. We conclude with a discussion of the scientific and technological relevance of our results.

4.2 Our approach

To introduce our approach to characterizing the exchange interaction at F/AF interfaces, we consider the interactions defining the equilibrium state of the magnetization $\vec{M}(\vec{r})$ of the F with thickness t in an F/AF bilayer. We assume that $\vec{M}$ is confined to the film plane (the xy plane) by the demagnetizing effects. We neglect the small magnetocrystalline anisotropy of F=Py, which is negligible compared to the other effects discussed here. We also neglect the effects of dipolar magnetic fields, since the analysis of the data presented below excludes highly inhomogeneous magnetization states where these effects may be significant. This set of approximations is commonly referred to as the standard xy spin model.

The Zeeman interaction of $\vec{M}$ with the in-plane external field H is characterized

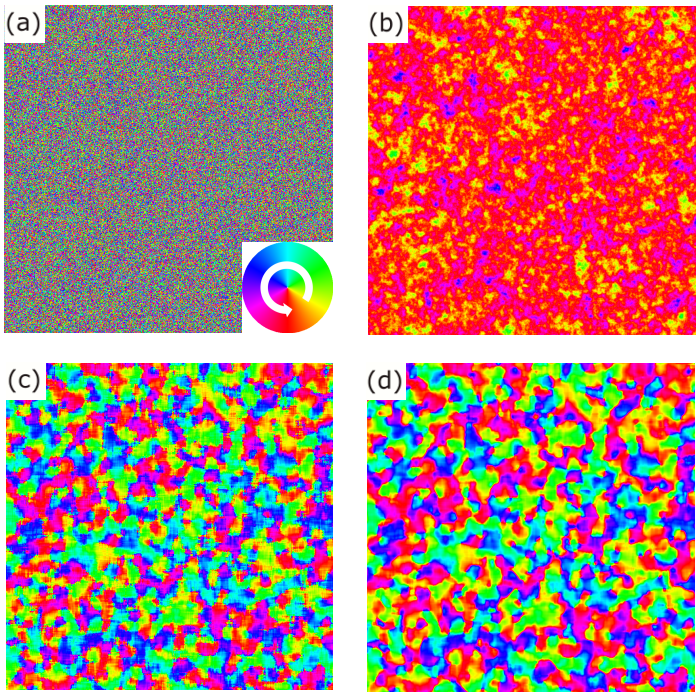

Figure 4.1: Uncorrelated vs correlated random field effects. (a),(b) Distribution of uncorrelated random field $h = 50$ kOe on a 2d mesh of square 2 nm$\times$2 nm cells (a) and the resulting magnetization distribution calculated using the $mumax3$ micromagnetic simulation software for a Py(6) film (b), at $H = 4$ kOe. For clarity, only a 1 $\mu m \times 1$ μm region of the 2 $\mu m \times 2$ μm simulation region is shown. (c),(d) same as (a),(b), for random field with the correlation length $l_h = 18$ nm.

by the magnetic energy density $\epsilon_Z = -\mu_0 \vec{M} \cdot \vec{H}$, where μ_0 is the vacuum permeability. The exchange interaction within F can be described by the Heisenberg energy density $\epsilon_{ex} = \frac{A}{M^2}((\vec{\nabla}\vec{M}_x)^2 + (\vec{\nabla}\vec{M}_y)^2)$, where A is the exchange stiffness. Finally, our analysis must include the effects of exchange interaction at the F/AF interface. At the microscopic level, the Heisenberg exchange energy per atom at the interface is $E_{ex,F/AF} = 2J_{F/AF} \langle \vec{s}_F \rangle \langle \vec{s}_{AF} \rangle$, where $J_{F/AF}$ is the Heisenberg exchange constant characterizing the strength of the interaction across the interface, $\vec{s}_F$ is the spin of the F atom at the interface, and $\vec{s}_{AF}$ is the spin of the nearest-neighbor AF atom. Different local atomic arrangements at the interface introduce a correction factor of order one, which can be absorbed in the definition of $J_{F/AF}$. The interfacial contribution to the energy density can be interpreted, in the spirit of Weiss's molecular field theory, as

an effective field $H_{int} = -2J_{F/AF} \langle \vec{s}_{AF} \rangle / g\mu_B$ exerted on the interfacial F spins due to the exchange interaction across the interface. Here, $g = 2$ is the g-factor for Py, and μ_B is the Bohr magneton. This contribution can be also approximated as an effective spatially-varying field acting on the entire F, if we assume that t is sufficiently small so that the magnetic configuration of F does not significantly vary through its thickness. This approximation is relaxed in the computational analysis presented later in this chapter. For F=Py with fcc crystal structure characterized by the cubic lattice constant $a = 0.36$ nm, the area per atom at the (111)-textured interface is $P = a^2/4\sqrt{3}$. The magnetic energy density associated with the exchange interaction across the F/AF interface can then be written as $\epsilon_{ex,F/AF} = -\mu_0 \vec{M}(\vec{r})\vec{h}(\vec{r})$, where

$$h(\vec{r}) = \frac{4\sqrt{3}J_{F/AF} \langle \vec{s}_{AF}(\vec{r}) \rangle}{\mu_0 M t a^2} \tag{4.1}$$

is the effective exchange field dependent on the in-plane position $\vec{r}$ but uniform through the thickness of F. The magnetic energy density of F is then

$$\epsilon = -\mu_0 \vec{M}(\vec{H} + \vec{h}) + \frac{A}{M^2}[(\vec{\nabla} M_x)^2 + (\vec{\nabla} M_y)^2]. \tag{4.2}$$

Following the notations of Garanin et al. [124], who analyzed the 3d version of a similar xy model, we introduce the angle $\varphi(\vec{r})$ between the magnetization and the field $\vec{H}$, and the angle $\phi(\vec{r})$ between $\vec{h}$ and $\vec{H}$. Minimizing the energy $\int \epsilon(\vec{r}) d^2r$ with respect to $\varphi(\vec{r})$, we obtain

$$\frac{A}{\mu_0 M} \nabla^2 \varphi(\vec{r}) - H sin\varphi(\vec{r}) = h sin(\varphi(\vec{r}) - \phi(\vec{r})). \tag{4.3}$$

This equation can be simplified for sufficiently large H, when the magnetization is almost saturated, and φ is small. We note that even in this limit, often described as the weak random field approximation [124], the magnitude of h needs not be small compared to H. In particular, the component $h \sin\phi$ parallel to $\vec{H}$ can be large

(both locally and on average), as is the case for F/AF bilayers, where this component determines the unidirectional and the uniaxial anisotropies associated with exchange bias [127, 128]. The component $h_\perp = h \sin\phi$ perpendicular to $\vec{H}$ may also be large if it rapidly varies in space, since its effects on the magnetization are averaged out by the exchange stiffness. Separating the contributions of $h_\parallel$ and $h_\perp$ in Eq. (4.3), we obtain

$$\frac{A}{\mu_0 M}\nabla^2\varphi - \varphi(H + h_\parallel) = -h_\perp. \tag{4.4}$$

We assume that neither the preparation of the magnetic system (such as field-cooling) nor its magnetocrystalline properties favor any particular in-plane direction non-collinear with $\vec{H}$. The symmetry with respect to the direction of $\vec{H}$ implies that the average of $h_\perp$ over a sufficiently large area must vanish, and therefore this quantity must vary in space, changing sign over some characteristic length scale l_h.

Malozemoff's uncorrelated random-field approximation is based on the assumption that effective field varies randomly on the atomic lengthscale, i.e. $l_h \sim a$. While the effective field itself is uncorrelated, the exchange stiffness of the ferromagnet defines the magnetic correlation length $l_M = \sqrt{A/\mu_0 M(H + \langle h_\parallel \rangle)}$. This is illustrated in Figs. 4.1(a),(b) by the micromagnetic simulations for a Permalloy=Py(6) film subjected to an uncorrelated random field $h = 50$ kOe. Here, the number in parenthesis is the thickness in nanometers. The statistical properties of the magnetization state in this limit are analyzed in Sections 4.4 and 4.5. We note that because of the negligible anisotropy of Py, the local magnetic configuration in such as state is determined entirely by the competition between the random field and the exchange stiffness. Therefore, the magnetization in such a state is twisted everywhere, i.e. it is an xy version of the HDS predicted by Malozemoff.

Here, we consider the opposite limit of quasi-uniform $h_\perp$, $l_h > l_M$, such that the first term in Eq.(4.4) can be neglected. This limit may provide a good description

for the exchange-spring behaviors of thin-film polycrystalline AFs, where the characteristic length scales for the variation of interfacial exchange torques, determined by the "winding" of the exchange spring, are expected to be determined by the size of AF grains [129, 102].

In this limiting case, $\varphi = h_\perp/(H + h_\parallel)$, i.e. $\vec{M}(\vec{r})$ is simply aligned with the local net effective field $\vec{H} + \vec{h}$, as illustrated by the simulations in Figs. 4.1(c),(d). For the average magnitude of deviation from saturation, we obtain

$$\langle \varphi^2 \rangle = \frac{\langle h_\perp^2 \rangle}{(H + h_\parallel)^2}, \tag{4.5}$$

where we have neglected the higher-order effects associated with the spatial variations of $h_\parallel$. This approximation is justified, for example, for $H \gg h_\parallel$.

By fitting the experimentally determined dependence of $\langle \varphi^2 \rangle$ on H with Eq.(4.5), one can determine the parameters $\langle h_\perp^2 \rangle$ and $h_\parallel$. In the discussion and figures presented in the next section, we will for brevity use the notation $h_\perp$ when referring to $\sqrt{\langle h_\perp^2 \rangle}$. For $l_h \gg l_e$, both $h_\parallel$ and $h_\perp$ are expected to scale inversely with the thickness t of the ferromagnet [see Eq. (4.1)]. Some of the data discussed below exhibit significant deviations from this expected dependence. We will present analysis based on a combination of analytical calculations, simulations, and scaling, to show that these results are consistent with Malozemoff's hypothesis of uncorrelated random effective exchange field.

4.3 Experiment setup

Multilayer films with the structure CoO(6)Py(t)Ta(5) were deposited on 6 mm×2 mm silicon substrates at room temperature, in a high vacuum sputtering system with the base pressure of 5×10^{-9} Torr. The numbers in parenthesis are thicknesses in nanometers, the thickness t of Py was varied between 5 nm and 50 nm, and Ta(5)

served as a capping layer protecting the films from oxidation. The multilayers were deposited in 150 Oe in-plane magnetic field, which is known to facilitate magnetic ordering in CoO. Py and Ta were deposited by dc sputtering from the stoichiometric targets, in 1.8 mTorr of ultrapure Ar, while CoO was deposited from a Co target by reactive sputtering in ultrapure oxygen atmosphere, with the partial pressure of oxygen optimized as in our previous studies of CoO-based systems [130, 121, 123].

To characterize the unsaturated magnetization state of the Py films in the studied heterostructures, we utilized electronic measurements of the variations of resistance R due to the anisotropic magnetoresistance (AMR), using ac current with rms amplitude of 50 μA and lock-in detection in the four-probe van der Pauw geometry. The AMR exhibits a 180°-periodic sinusoidal dependence on the angle between the magnetization of Py and the direction of current, as was verified by measurements at temperature $T = 300$ K above the Neel temperature of CoO, $T_N = 291$ K [inset in Fig. 4.2(a)].

Measurements described below were performed for two orientations of the external field, one collinear and the other perpendicular to the direction of current, so that in the saturated state the AMR was maximized and minimized, respectively. Any deviations from saturation resulted in resistance decrease in the first configuration, and increase in the other. These were the signals detected in our magnetoelectronic measurements to characterize the inhomogeneous states. Data analysis was limited only to resistance ranges deviating by less than 10% of the full magnetoresistance from the saturation value, ensuring the small-angle limit for φ. For the measurements performed at $T < T_N$, the sample was cooled through T_N in field $H = 1$ kOe. The cooling field was aligned with the positive direction of the field H utilized in the subsequent measurements.

At high temperature $T > T_N$, CoO is a paramagnet, and is not expected to significantly affect the state of Py. The magnetization $\vec{M}$ of Py is expected to become

saturated at small fields determined by the magnetocrystalline anisotropy of Py. Indeed, magnetoelectronic hysteresis loop measurements show negligible variations of R, aside from a sharp peak at small H associated with the reversal of M, as shown in Fig. 4.2(a) for Py(7.5)/CoO(6). In contrast, at $T = 7$ K, the R vs H curves exhibit gradual variations and do not saturate even at $H = \pm 4$ kOe, Fig. 4.2(b).

These data clearly indicate the presence of a large transverse component $H_\perp$ of the effective exchange field, resulting in the deviations of magnetization from the saturated state even at large H. The curves labeled a,c were acquired using the field direction collinear with the current direction, such that the resistance is maximized when M is saturated along the field. Meanwhile, the curves labeled b,d were acquired with the field perpendicular to the current, resulting in the resistance minimum in the saturated state. These two complementary sets of measurements are necessary for the quantitative data analysis, as discussed below.

The peaks in the hysteresis curves correspond to the magnetization reversal points. These points are shifted in the negative-field direction in Fig. 4.2(b), as expected due to the exchange bias effect. We note that the values of $R(H)$ do not exactly coincide for two opposite directions of field sweep. The difference can be attributed to the aging phenomena in AF, as demonstrated by recent time-domain measurements [121]. Aging effects were shown to be large for CoO thicknesses below 4 nm, and become rapidly reduced for larger thicknesses. To minimize their possible influence on our analysis, we focus below only on the hysteresis branches obtained with the field swept from larger to smaller magnitudes. To directly relate our $R(H)$ data to the analysis presented above, we note that AMR provides direction information about the local deviations of the magnetization state from saturation, according to $R = R_{min} + \Delta R sin^2\varphi$ for $\vec{H}$ perpendicular to the current, and $R = R_{max} - \Delta R sin^2\varphi$ for $\vec{H}$ parallel to the current. Here, R_{min} and R_{max} are the minimum and the maximum of resistance due to AMR, respectively, $\Delta R = R_{max} - R_{min}$, and $\varphi(\vec{r})$ is the angle

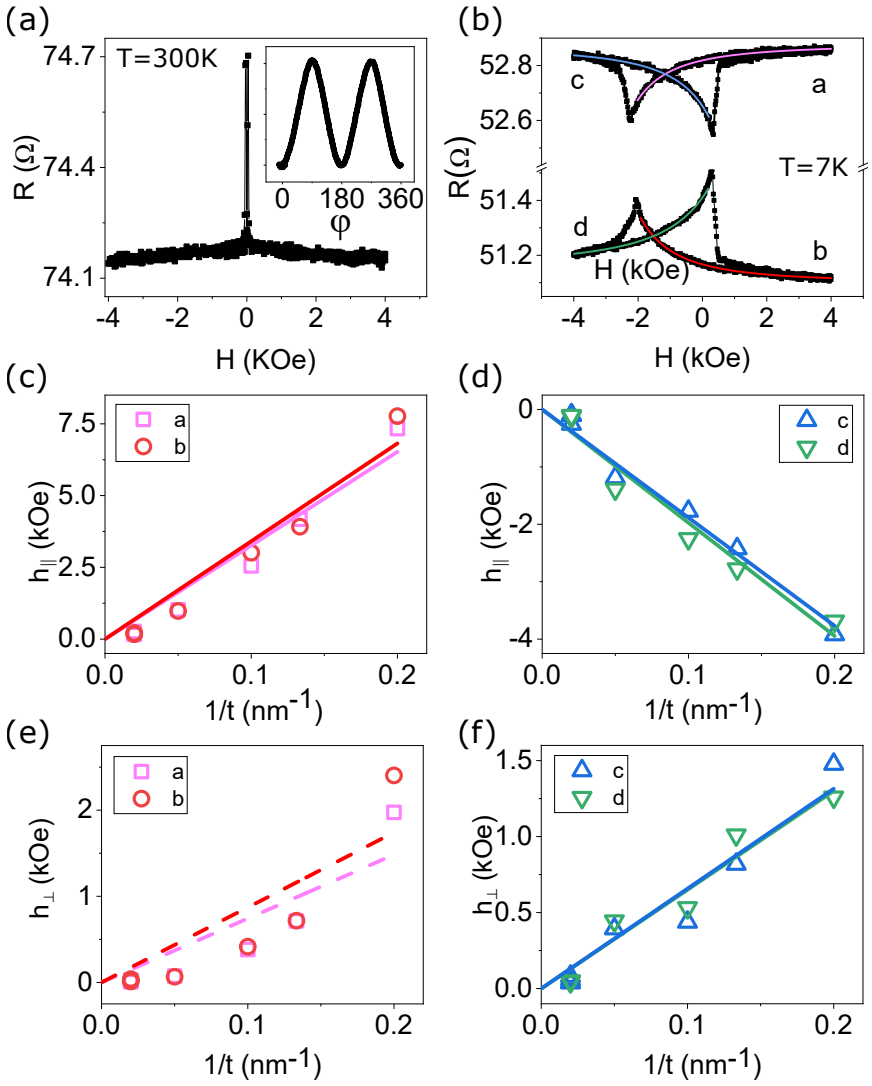

Figure 4.2: Evidence for random-field effects in Py/CoO bilayers. (a) Magnetoelectronic hysteresis loop of Py(7.5)/CoO(6) measured at 300 K, with the external field $\vec{H}$ oriented in-plane perpendicular to the current. Inset: dependence of resistance on the direction of in-plane field $H = 1$ kOe, at $T = 300$ K. (b) Symbols: Magnetoelectronic hysteresis loop for Py(7.5)/CoO(6) at $T = 7$ K, for external field parallel to current (labeled a,c) and perpendicular to current (labeled b,d). Curves: fits with Eq. (4.5). (c)-(f) Symbols: $h_{\parallel}$ (c), (d) and $h_{\perp}$ (e), (f) vs $1/t$ obtained from the fits as shown in (b), for the four hysteresis branches a-d. Lines are linear fits with zero intercept.

between $\vec{H}$ and $\vec{M}$. For $h_\perp$ characterized by a large correlation length l_h, we obtain from Eq.(4.5) for small φ

$$R = R_{max} - \Delta R \frac{h_\perp^2}{(H + h_\parallel)^2}, \tag{4.6}$$

for the external field direction parallel to current, and

$$R = R_{min} + \Delta R \frac{h_\perp^2}{(H + h_\parallel)^2}, \tag{4.7}$$

for the external field perpendicular to current. We emphasize that Eqs. (4.6), (4.7) are valid only in the limit of large correlation length l_h of $\vec{h}$, so that the magnetization locally follows the direction of the total effective field.

The curves in Fig. 4.2(b) show the results of data fitting with Eqs.(4.6) and (4.7), with $h_\parallel$ and $h_\perp$ treated as independent parameters for each of the four branches, but with the same fitting values of R_{min}, R_{max}, and $\Delta R = R_{max} - R_{min}$. By fitting all the four branches of the hysteresis loops obtained for different thicknesses t of Py with Eqs. (4.6) and (4.7), the dependence of $h_\parallel$ and $h_\perp$ on t was determined. Since both of these quantities represent the effects of exchange interaction at the F/AF interface averaged over the thickness of Py, they are expected to scale inversely with t [see Eq. (4.1)]. To assess the validity of this expectation, we plot the dependences of $h_\parallel$ and $h_\perp$ on $1/t$ in Figs. 4.2(c),(d) and Figs. 4.2(e),(f), respectively.

The dependence $h_\parallel(1/t)$ is well described by a linear fit with zero intercept for all four branches [Figs. 4.2(c),(d)], consistent with our analysis. We emphasize that this result is expected regardless of the correlation length l_h of the effective exchange field, because the spatial average of $h_\parallel(\vec{r})$ is finite. Similarly, $h_\perp(1/t)$ is also well described by a linear fit with zero intercept, for the hysteresis branches c,d corresponding to the magnetization state reversed relative to the field-cooling, Fig. 4.2(f). This result indicates that the correlation length l_h of the effective exchange field is large in this

reversed state, consistent with the picture of AF exchange spring "wound" by the reversal of magnetization, with the same "winding" direction over a significant volume of CoO the may include the entire grains of the polycrystalline CoO film [129, 102].

In contrast, for the two branches a,b corresponding to the magnetization aligned with the field-cooling direction, the dependence $h_\perp(1/t)$ is strongly nonlinear [Fig. 4.2(e)], demonstrating that the correlated effective exchange field approximation underlying Eqs.(4.6) and (4.7) is invalid. We emphasize that the linear fits in this panel are included only to highlight the nonlinear variations of the data. These fits are not used in this work to determine any physically meaningful parameters of the studied system.

The values of $h_\perp(1/t)$ extracted from our analysis increase superlinearly with increasing $1/t$. This result can be qualitatively expected for the effects of random field with a small correlation length, because at large $1/t$ (small t), magnetic correlations within F are less efficient in averaging the short-scale variations of the field. To quantitatively analyze our results, in the next sections we will extend our analysis of the magnetization state of F in F/AF bilayer to include the effects of random uncorrelated effective fields, and show that the results of Fig. 4.2(d), for the field parallel to the cooling field, are consistent with the presence of uncorrelated random effective exchange field at the Py/CoO interface.

4.4 2d xy model of uncorrelated random field effects

In this section, we analyze the effects of an uncorrelated random field on a 2d magnetic system. This analysis is expected to be applicable to magnetic films with sufficiently small thickness t, such that their magnetization is uniform through the thickness. In the next section, we present realistic 3d micromagnetic simulations of thin films,

and show that their results asymptotically approach our analytical predictions for 2d systems in the limit of vanishing film thicknesses.

Since Py is characterized by negligible magnetocrystalline anisotropy, and its magnetization in the studied films remains in-plane due to the large demagnetizing field, the system can be described by the 2d xy model. We follow the approach of Garanin et al., who analyzed the 3d version of a similar random-field xy model [124]. The system is characterized by the position-dependent angle $\varphi(\vec{r})$ between the magnetization and the external field, which is determined by the distribution of the effective field $\vec{h}(\vec{r})$ according to Eq. (4.4). The average of the component $h_{\parallel}$ of the effective field parallel to $\vec{H}$, which is nonzero in the experimental system discussed above, is absorbed into the definition of H. Thus, in the analysis below, we assume that both $h_{\parallel}$ and $h_{\perp}$ form the same random distributions with zero averages. Since φ is small at sufficiently large H, the term $\varphi h_{\parallel}$ in Eq. (4.4) can be neglected, giving

$$\frac{A}{\mu_0 M}\nabla^2\varphi - \varphi H = -h_{\perp}. \tag{4.8}$$

The random field $h_{\perp}$ is assumed to be uncorrelated among different lattice sites i, j, $\langle h_{\perp,i} h_{\perp,j}\rangle = h^2\delta_{ij}/2$. In the micromagnetic simulations discussed in the next section, the simulation cells play the role of the lattice sites. To capture the effects of random field, the cubic cell size D must be smaller than the magnetic correlation length l_M. The magnitude of the random field is then scaled between the two descriptions according to $h_{\perp,mm}D = h_{\perp,at}\sqrt{P}$, where P is the area per site of the 2d lattice, $\sqrt{P} = a$ for square lattices, and $\sqrt{P} = a/4\sqrt{3}$ for the (111) face of the fcc lattice. In the continuous limit discussed in this section,

$$\langle h_{\perp}(\vec{r}) h_{\perp}(\vec{r}')\rangle = h^2 P\delta(\vec{r} - \vec{r}')/2. \tag{4.9}$$

Using $k = 1/l_M = \sqrt{\mu_0 MH/A}$, we rewrite Eq. (4.8) as

$$(\nabla^2 - k^2)\varphi = -h_\perp \mu_0 M/A. \tag{4.10}$$

The solution in terms of the Green's function $G(k, \vec{r})$ of the operator $\nabla^2 - k^2$ is

$$\varphi(\vec{r}) = -\frac{\mu_0 M}{A} \int d^2\vec{r}' G(k, \vec{r} - \vec{r}') h_\perp(\vec{r}'). \tag{4.11}$$

The Green's function can be expressed in terms of the modified Bessel function of the second kind, $K_0(x) = \frac{1}{2}\int_{-\infty}^{+\infty} \frac{e^{ixt}dt}{\sqrt{1+t^2}}$, $G(k, \vec{r}) = -K_0(k|r|)/2\pi$. The average of φ^2 over the realizations of random field is

$$\begin{aligned} \left\langle \varphi^2(\vec{r}) \right\rangle = \left(\frac{\mu_0 M}{2\pi A}\right)^2 \int d^2\vec{r}' d^2\vec{r}'' K_0(k|\vec{r} - \vec{r}'|) \cdot \\ \cdot K_0(k|\vec{r} - \vec{r''}|) \left\langle h_\perp(\vec{r}') h_\perp(\vec{r}'') \right\rangle . \end{aligned} \tag{4.12}$$

Using the correlation relation Eq. (4.9), we obtain

$$\left\langle \varphi^2(\vec{r}) \right\rangle = \frac{\mu_0^2 M^2 h^2 P}{8\pi^2 A^2} \int d^2\vec{r}' K_0^2(k|\vec{r} - \vec{r}'|). \tag{4.13}$$

Finally, we use the relation $\int d^2 r K_0^2(kr) = \pi/k^2$ to obtain

$$\left\langle \varphi^2 \right\rangle = \frac{\mu_0^2 M^2 h^2 P}{8A^2 k^2} = \frac{\mu_0 M h^2 P}{8AH}. \tag{4.14}$$

In comparison, Garanin et al. [124] obtained $\langle \varphi^2 \rangle \propto h^2/\sqrt{H}$ for the 3d xy random field model, and our correlated-random-field result, Eq. (4.9), is $\langle \varphi^2 \rangle \propto h^2/H^2$. In all cases, $< \varphi^2 > \propto h^2$. This can be expected from the general Eq. (4.8) for the magnetization distribution, which is invariant under the scaling transformation $h_\perp \to \alpha h_\perp$, $\varphi \to \alpha\varphi$. Thus, this result is expected to generally hold regardless of the system

geometry or the spatial properties of $\vec{h}$. On the other hand, these expressions contain different powers of external field H, dependent on the random field distribution and the dimensionality of the system. All these relations can be written in an explicitly dimensionless form as

$$\langle \varphi^2 \rangle = C \left(\frac{h}{H} \right)^2 \left(\frac{P}{l_M^2} \right)^d , \tag{4.15}$$

where the numeric coefficient C and the power-law exponent d are dependent on the system realization. For the correlated random field, $d = 0$, while for the uncorrelated random field in 2d (3d), $d = 1$ (3/2). Based on the scaling arguments for the random field, we expect $d = n/2$ for the uncorrelated random field in n dimensions. In the next section, we use Eq. (4.15) as an ansatz with d treated as a fitting parameter, to analyze the micromagnetic simulations of interfacial exchange effects in F/AF bilayers.

4.5 Simulations of uncorrelated random field effects

The analytical model introduced in the previous section is expected to quantitatively describe the effects of uncorrelated random field only for atomically-thin F. For finite thickness of F in F/AF bilayers, magnetic moments away from the F/AF interface experience only indirect effects of effective exchange field averaged over their neighbors, introducing spatial correlations that are not accounted for by the model. In this section, we use 3d micromagnetic simulations and an extension of the scaling arguments presented above to analyze a more realistic model where random field is applied only to one of the surfaces of a thin Py film. We also show that the results are consistent with the analytical model in the limit of ultrathin films.

We performed micromagnetic simulations with the mumax3 software [26], using the standard parameters for Py, the magnetization $\mu_0 M = 1.0$ T, Gilbert damping $\alpha = 0.01$, and exchange stiffness $A = 1.3 \times 10^{-11}$ J/m. The simulated volume was 2 $\mu m \times 2$ $\mu m \times t$, with varied thickness t. This volume was discretized into cubic cells, whose size D was varied from 1 nm to 12 nm to evaluate the discretization effects, as described below. Periodic boundary conditions were used to eliminate edge effects. Random uncorrelated field with fixed magnitude h was generated by selecting a random variable ϕ uniformly distributed over the interval $[0, 2\pi]$. In all the simulations discussed below, this field was applied only to the bottom layer of the simulation mesh.

In the limit of vanishing film thickness, $D \to 0$ and only one layer present in the simulation mesh, this system maps onto the analytical model described in the previous section via $D^2 \to P$. The magnitude of h can be related to the effective exchange field experienced by the atoms at the interface, according to $H_{int} = 3^{3/4} 2hD^2/a^2$ for the (111)-textured surface of fcc ferromagnet with a cubic lattice constant a.

The simulations were performed with the magnetic system initialized in a uniform state aligned with the field $\vec{H}$, and were continued until the dynamics became negligible for all the simulation cells. The distribution was then analyzed to determine $\langle \varphi^2 \rangle$. Figs. 4.1(a),(b) illustrate a representative random field distribution and the resulting magnetization map in the equilibrium state, for $t = D = 2$ nm, $H = 4$ kOe, $h = 50$ kOe. While the random field distribution is uncorrelated, the resulting magnetization distribution exhibits correlations on the length scale $l_M = \sqrt{A/\mu_0 MH} = 6$ nm. For the correlated field with the correlation length $l_h > l_M$, the magnetization is expected to simply follow the local direction of the net effective field, as was verified by the simulation using random field with correlation length $l_h = 18$ nm [Figs. 4.1(c),(d)].

To determine the optimal simulation cell size D that does not significantly dis-

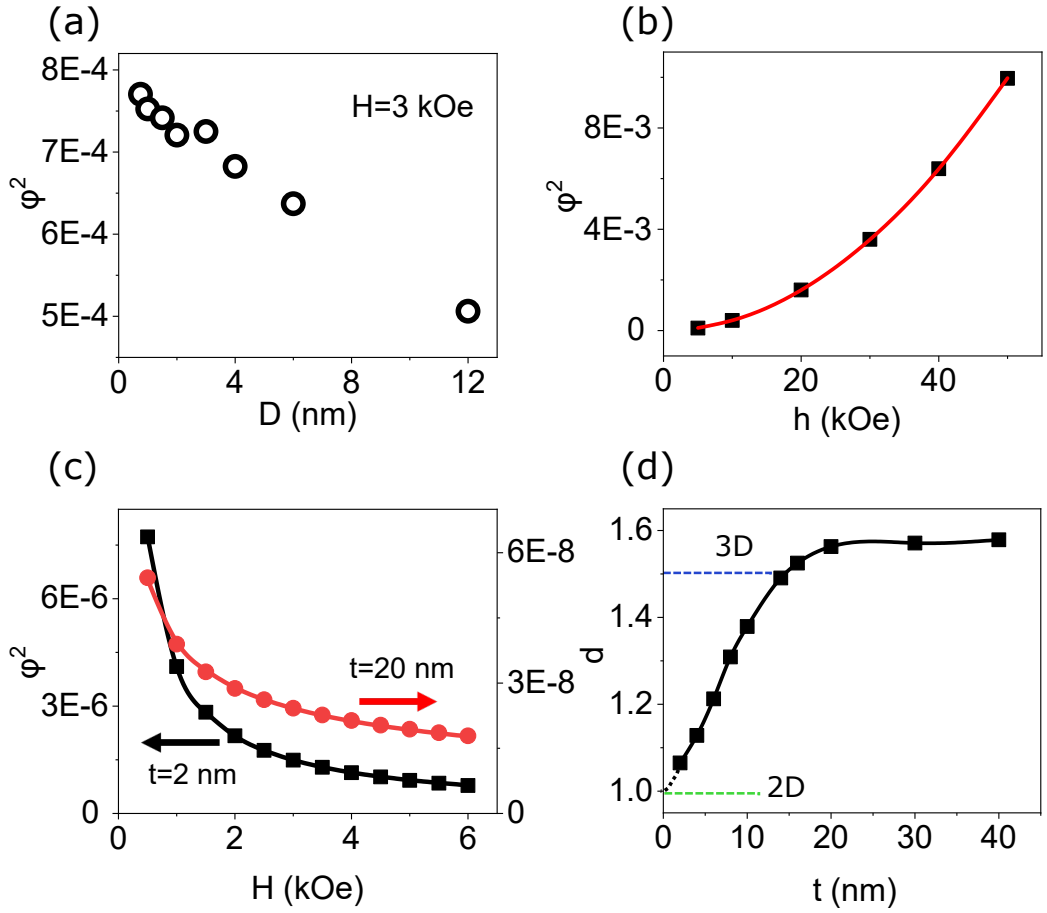

Figure 4.3: Micromagnetic simulations of random field effects. (a) $\langle\varphi^2\rangle$ vs cell size D for a 12 nm-thick Py film, at $H = 3$ kOe and $\mu_0 h D^2 = 5\ T \cdot nm^2$. (b) Symbols: $\langle\varphi^2\rangle$ vs h for a 10 nm-thick Py film, at $H = 6$ kOe. Curve: fit with a quadratic function. (c) $\langle\varphi^2\rangle$ vs H, for Py films with $t = 2$ nm and $t = 20$ nm, as labeled. Symbols are the results of simulations, and curves are fits using the ansatz Eq. (4.15). (d) Dependence of the power law exponent d in Eq. (4.15) on the Py film thickness.

tort the magnetization response to the random field, we performed simulations with different values of D ranging from 1 nm to 12 nm, Fig. 4.3(a). To facilitate direct comparison, the value of h was adjusted so that hD^2 remained independent of D, in accordance with the scaling relations expected for the random field. The value of $\langle\varphi^2\rangle$ monotonically decreases with increasing D, as expected due to the filtering effect of larger cells on the short-scale random field variations. In the simulations discussed below, we use a sufficiently small cell size $D = 2$ nm so that these filtering effects are small, while keeping the simulations of thicker films manageable. Figure 4.3(b) shows

the dependence of $\langle\varphi^2\rangle$ on h, with all the other parameters fixed. This dependence is precisely described by the quadratic relation expected from Eq. (4.15). Thus, it is sufficient to perform simulations only for one value of h small enough to satisfy the weak random field approximation $\varphi^2 \ll 1$.

The central goal of our simulations was to determine the dependence of random field effects on the film thickness. To this end, we performed simulations of the dependence of the magnetization state on the external bias field $H = 0.5 - 6$ kOe for thicknesses $t = 2 - 40$ nm, with h fixed at 100 Oe. In all cases, the dependence of $\langle\varphi^2\rangle$ on H could be precisely fitted by Eq. (4.15), or equivalently

$$\left\langle\varphi^2\right\rangle = C'\frac{h^2D^4}{H^{2-d}}, \tag{4.16}$$

with the power-law exponent d and the constant $C' = CD^{-4}(\mu_0 Ma^2/4\sqrt{3}A)^d$ used as fitting parameters. In this expression, we scaled h by the cell size, so that the constant C' becomes independent of D. Figure 4.3(c) shows the fits for two representative thicknesses $t = 2$ nm and 20 nm, yielding the best-fit values $d = 1.065$ and 1.57, respectively. We note that these two representative dependences are substantially different, demonstrating that precise fitting requires the value of d to be varied with t.

Figure 4.3(d) shows the dependence of the power-law exponent d on the film thickness, extracted from the $\langle\varphi^2\rangle$ vs H curves such as those shown in Fig. 4.3(c). This dependence extrapolates to $d = 1$ in the limit of vanishing film thickness, consistent with the results of the analytical 2d xy model described in the previous section. The value of d increases with t, reaching $d_s = 1.57$ for $t = 20$ nm, and becomes constant at larger t. Qualitatively, these behaviors can be interpreted in terms of the crossover from the effective 2d regime to the effective "bulk" regime, where the effects of random field become almost completely averaged out far enough from the interface, such that

increasing t simply rescales $\langle\varphi^2(H)\rangle$ due to averaging over the larger volume, without changing the functional relation. We emphasize that random field is applied only to one of the film surfaces. Thus, this regime is not equivalent to the 3d random-field model considered by Garanin et al. [124]. Indeed, the saturation value d_s is different from $d = 3/2$ obtained in the latter case.

4.6 Analysis of experimental results

We now show that Eq. (4.15), with the power-law exponent $d(t)$ determined from the micromagnetic simulations, provides an explanation of our experimental data, supporting Malozemoff's uncorrelated random-field hypothesis.

If the effects of the exchange field at the Py/CoO interface can be approximated by a random field uncorrelated on the atomic scale, then the dependence of R on H can be inferred from Eq. (4.16), with the power-law exponent d and the scaling constant C' determined from the simulations discussed above, H offset by $h_\parallel$, and h^2D^4 replaced by $H_{int}^2a^4/4\sqrt{3}$,

$$R = R_{max} - \frac{C'\Delta R}{4\sqrt{3}}\frac{H_{int}^2a^4}{(H+h_\parallel)^{2-d}}, \tag{4.17}$$

for the external field parallel to current, and

$$R = R_{min} + \frac{C'\Delta R}{4\sqrt{3}}\frac{H_{int}^2a^4}{(H+h_\parallel)^{2-d}}, \tag{4.18}$$

for the external field perpendicular to current.

Figure 4.4(a) shows the same data as in Fig. 4.2(b), but now fitted using Eqs. (4.17), (4.18), with the power-law exponent $d = 1.28$ for Py(7.5) determined from the micromagnetic simulations described above. Both this fitting and the fitting with $d = 0$ in Fig. 4.2(b) provide good fits for the data. This shows that, in contrast to the mi-

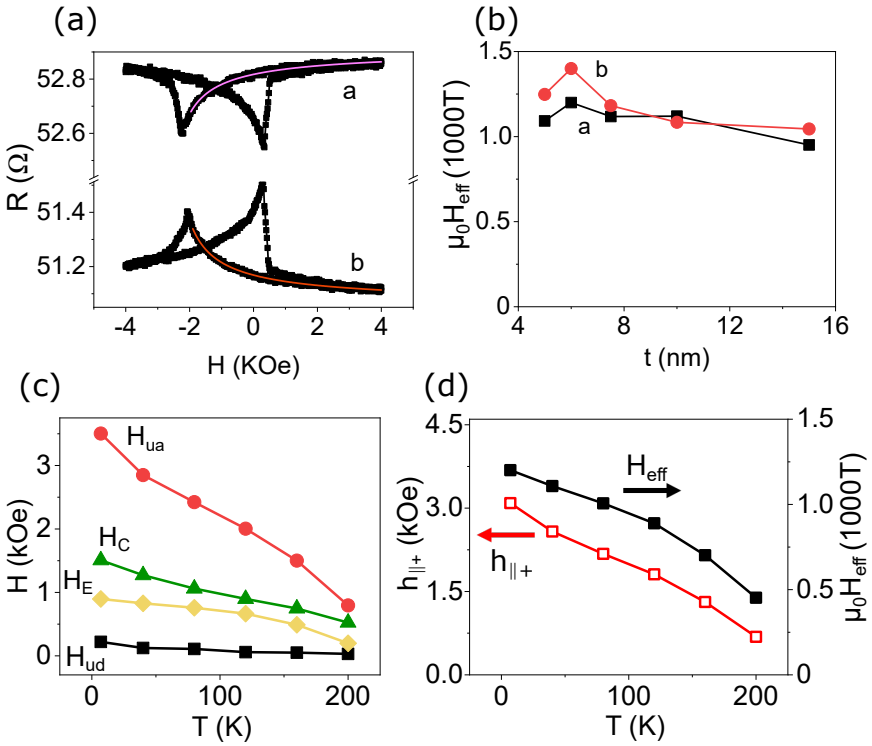

Figure 4.4: Quantitative analysis of effective exchange fields. (a) Symbols: the same magnetoelectronic hysteresis loop as in Fig. 4.2(b), acquired at $T = 7$ K for Py(7.5)/CoO(6). Curves: fits of branches a,b based on Eq. (4.15), with the power-law exponent $d = 1.28$ determined from the micromagnetic simulations. (b) The magnitude of the effective random exchange field $\mu_0 H_{eff}$ vs Py thickness, determined from fits such as shown in panel (a). (c) Coercivity H_C, effective exchange bias field H_{EB}, effective uniaxial anisotropy field H_{ua}, and unidirectional anisotropy field H_{ud} vs T, determined for Py(6)/CoO(6) as discussed in the text. (d) Parallel component $h_{\parallel,+}$ of the effective exchange field, [open symbols and right scale] and the effective random field H_{eff} [solid symbols and right scale] vs T for Py(6)/CoO(6), obtained from branch a of the R vs H data.

cromagnetic simulations, the power-law exponent d cannot be accurately determined from the experimental data. The reason for this discrepancy is that the values R_{min} and R_{max} of resistance in the saturated states with the magnetization perpendicular and parallel to current, respectively, as well as the parallel component $h_{\parallel}$ of the effective exchange field, cannot be independently determined, and must be thus treated as additional fitting parameters. The experimental data do not provide sufficient information to accurately determine these parameters together with d. While fitting the experimental R vs H curves does not allow us to determine d, we can still establish

whether the observed behaviors are consistent with the uncorrelated random field approximation. We use the approach similar to that described in Section 4.3, where we have shown that the correlated effective field approximation cannot describe the magnetization state for the field aligned with the cooling field [see Fig. 4.2(d)]. We fit the $R(H)$ curves for different thicknesses t of Py with Eqs. (4.17), (4.18), using the thickness-dependent values of $d(t)$ and $C'(t)$ obtained from the micromagnetic simulations. Each such fitting independently yields the value of the effective exchange field H_{int}. The uncrorrelated random field approximation is valid if the obtained values of H_{int} are independent of t. However, if the effective exchange field is correlated, then the values of H_{int} extracted from such fitting should increase with t, because in contrast to the uncorrelated field, the effects of the correlated field are not averaged out by larger thickness.

Figure 4.4(b) shows the values of $\mu_0 H_{int}$ determined from the fits of $R(H)$ for different Py thicknesses. The values exhibit modest variations around the average value of 1×10^3 T, and appear to slightly decrease at large t, but clearly do not increase, as would be expected for the correlated field. We note that our procedure for calculating the values of H_{eff} involves multiple sources of random and systematic errors, including the uncertainty of the thicknesses of Py, slight variations of the deposition conditions resulting in the variation of H_{eff} among different samples, as well as the uncertainty of the fitting itself. These uncertainties are difficult to estimate *a priori*, warranting more detailed studies of multiple similar samples to assess them statistically. Nevertheless, the results shown in Fig. 4.4(b) for five samples with different thicknesses provide strong evidence for the validity of random-field approximation. Furthermore, the magnitude of $\mu_0 H_{eff}$ of about 1×10^3 T is about 10 times smaller than the typical strength of the nearest-neighbor exchange interactions in magnetic materials [131], as would be expected given that the spin-flop of AF spins at the F/AF interface results in their partial alignment [127, 128].

Our approach to quantifying the effective exchange fields in F/AF bilayers is validated by the analysis of the relationship between these fields and the essential characteristics of the magnetic hysteresis loop, the coercivity $H_C = (H_1 - H_2)/2$ and the exchange bias field $H_E = (H_1 + H_2)/2$. Here, H_1 (H_2) is the magnetization reversal field on the down (up) sweep, signified by the sharp peaks in R vs H curves [see Fig. 4.4(b)]. The exchange bias field is generally attributed to the unidirectional anisotropy, while the enhanced coercivity is attributed to the uniaxial anisotropy acquired by F due to the exchange interaction at F/AF interface.

Our approach allowed us to determine the value of $h_\parallel$, the net effective exchange field experienced by Py, separately for the magnetization orientation parallel to the cooling field [by fitting $R(H)$ branches a,b with Eqs. (4.17), (4.18)], and for the magnetization orientation opposite to the cooling field [by fitting $R(H)$ branches c,d with Eqs. (4.6), (4.7)]. We label the corresponding two values $h_{\parallel,+}$ and $h_{\parallel,-}$. The effective unidirectional and uniaxial anisotropy fields can be then directly determined as $H_{ud} = (h_{\parallel,+} + h_{\parallel,-})/2$ and $H_{ua} = (h_{\parallel,+} - h_{\parallel,-})/2$, respectively. We emphasize that these values are determined by fitting the $R(H)$ curves for small deviations from saturation at large fields, completely independently from H_C, H_E that characterize magnetization reversal at small fields.

Figure 4.4(c) shows the temperature dependences of all four characteristics H_E, H_C, H_{ud}, and H_{ua}, for the Py(6)/CoO(6) sample at $T \leq 200$ K. At higher temperatures, the deviations from saturation were too small to reliably determine $h_\parallel$ by fitting the $R(H)$ curve. The relations among H_E, H_C, H_{ud}, and H_{ua} are consistent with the results for a similar Py/CoO bilayer system, obtained by a completely different technique of transverse ac susceptibility [123]. In particular, that study showed that the unidirectional anisotropy in this system is much smaller than the effective exchange bias field, and does not follow the temperature dependence of the latter. The data in Fig. 4.4(c) are consistent with this observation. Transverse ac susceptibility measure-

ments also showed that H_E and H_C are about half of H_{ua}, and approximately follow the temperature dependence of the latter. These observations are also confirmed by the results in Fig. 4.4(c). While these results may seem surprising, they are consistent with the analysis of Ref. [123], which suggested that the asymmetry of the hysteresis loop for the Py/CoO bilayers is predominantly caused not by the unidirectional anisotropy, but rather by the different mechanisms of magnetization reversal between the two opposite magnetization states stabilized by the uniaxial anisotropy.

The random field H_{eff}, determined by fitting branches a and b of the $R(H)$ curve with Eqs. (4.17) and (4.18), decreases with increasing temperature [solid symbols and right scale in Fig. 4.4(d)], following the same overall trends as $h_{\parallel,+}$ [open symbols and left scale in Fig. 4.4(d)]. The similarity between the behaviors of these two quantities is a manifestation of their common origin from the exchange interaction at the Py/CoO interface.

Chapter 5

Ideal memristor based on viscous magnetization dynamics driven by spin torque

5.1 Memristor: an electronic neuron

As a follow up of the last section, here we demonstrate the potential memristive functionality of such system, which can be used for neuromorphic computing and artificial neural networks. Artificial neural networks, modeled after the functionality of brain, have recently emerged as a promising alternative to the traditional von Neumann computer architecture [132, 133, 134]. Among the advantages of neural networks are built-in adaptability, robust fault-tolerant operation, and the ability to process large amounts of data in real time. At the core of these capabilities is a network of neurons extensively connected by synapses. Synaptic plasticity - the dependence of the connection strength on the history of the transmitted signals - is central to the neural network's functionality [135, 136, 137].

An efficient hardware implementation of synaptic plasticity is provided by mem-

ristors - two-terminal circuit elements whose resistance is ideally proportional to the integral control parameter such as the total charge that passes through them [28, 138, 139, 140]. However, this "ideal" memristive behavior has not been achieved yet. Instead, many types of "generalized memristors" - devices whose properties depend in some way on their electronic history - have been explored for neuromorphic applications [141].

One of the most extensively studied memristors is based on the electromigration of oxygen in metal oxides [142, 7]. However, physical motion of atoms limits its device endurance, while abrupt formation and destruction of oxygen-depleted conductive filaments results in behaviors more akin to a switch. Another notable approach utilizes magnetic domain wall (DW) motion through a ferromagnetic (F) nanowire incorporated in a magnetic tunnel junction (MTJ) [143]. The DW is driven by the spin-transfer torque (STT), and its position is read-out via the tunneling magnetoresistance (TMR). Magnetism-based operation enables high endurance, but thermal fluctuations and defects compromise controllable STT-driven DW motion at nanoscale [144].

5.2 Ideal memristor in magnetic system

Here, we show that nearly ideal magnetoelectronic memristors can be implemented using nanoscale single-domain F characterized by strongly damped (viscous) dynamical characteristics, which can be achieved by sandwiching it with an ultrathin low-anisotropy antiferromagnet (AF) in the correlated spin liquid state. The active magnetic layer is incorporated into a magnetoresistive heterostructure such as MTJ [Fig. 5.1(a)], enabling its control by STT and readout via TMR. We also discuss practical device limitations and benefits.

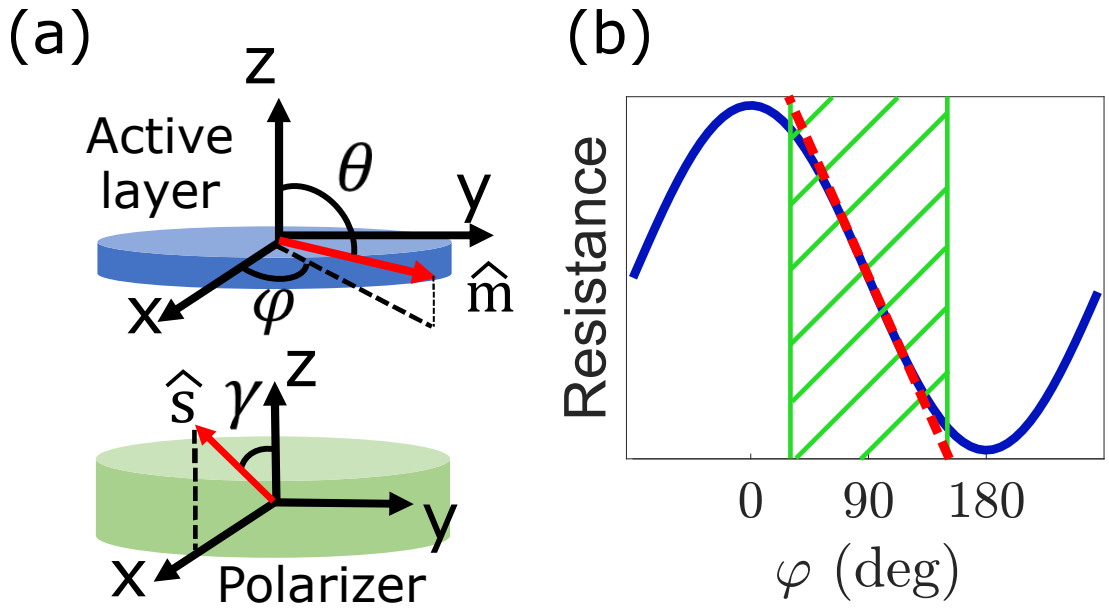

Figure 5.1: (a) Schematic of the proposed STT-driven memristor and the relevant parameters. (b) Typical sinusoidal dependence of resistance R on the in-plane magnetization orientation. The expected angular range of nearly ideal memristive behaviors is hatched. The dashed line is a guide for the eye.

5.3 Memristive functionality of the proposed device

STT-driven magnetization dynamics of a nanoscale single-domain F is described by the macrospin Landau-Lifshitz-Gilbert-Slonczewski (LLGS) equation,

$$\begin{aligned}\frac{d\hat{m}}{dt} &= -\mu_0\gamma\hat{m}\times\vec{H}_{eff} - \alpha\hat{m}\times\frac{d\hat{m}}{dt} \\ &+\sigma_{DL}\hat{m}\times(\hat{m}\times\hat{s}) + \sigma_{FL}\hat{m}\times\hat{s}.\end{aligned} \tag{5.1}$$

Here, $\hat{m}$ and $\hat{s}$ are unit vectors along the magnetizations of the free layer and the polarizer, respectively [Fig. 5.1(a)], μ_0 is the vacuum permittivity, α is Gilbert damping, and γ is the gyromagnetic ratio. The effective field $\vec{H}_{eff}$ includes crystalline and/or shape anisotropies, and the external and demagnetizing fields. The damping-like (DL) and the field-like (FL) contributions to Slonczewski's STT [145] are character-

ized by efficiencies σ_{DL} and σ_{FL}, respectively, which are proportional to the driving current density J and its spin polarization P. For instance, the DL-STT efficiency is $\sigma_{DL} = -\gamma\hbar JP/4M_s ed$, where $\hbar$ is the Planck's constant, M_s is the saturation magnetization, and d is the thickness of F.

The effects of thermal fluctuations are not included in Eq. (5.1) or in our analysis of magnetization dynamics below. The amplitude of thermal fluctuations is expected to scale inversely with $\sqrt{\alpha}$, similarly to the Einstein relation for the Brownian motion of a particle. Thus, the proposed highly damped magnetic dynamics is not expected to be significantly affected by thermal fluctuations even for the superparamagnetic systems similar to those utilized in p-bits [146].

First, we consider a simple case of negligible magnetocrystalline and shape anisotropies, and $\hat{s}$ normal to the plane. In this geometry, the effective FL-STT field is normal to the plane. Its effect is negligible at practical driving currents due to the large demagnetizing field. The solution of Eq. (5.1) is the out-of-plane precession (OPP) mode driven by DL-STT [147, 148, 149, 150],

$$\begin{aligned} \hat{m}_z &= \sigma_{DL}/\alpha\mu_0\gamma M_S \\ \hat{m}_x + i m_y &= e^{i\sigma_{DL}t/\alpha + i\phi_0}\sqrt{1-m_z^2}. \end{aligned} \tag{5.2}$$

Since the angular velocity $\omega = \sigma_{DL}/\alpha$ of precession is inversely proportional to damping, this dynamics can be described as viscous. The absence of a damping-dependent threshold current demonstrates that efficient STT-driven dynamics can be achieved even at large α.

The angle between $\hat{m}$ and $\hat{s}$ remains constant, and does not produce resistance variations due to precession. To generate magnetoelectronic signals, $\hat{s}$ can be tilted towards the x-axis. We assume that the tilt angle is sufficiently small, so that the effect of tilting on the dynamics can be neglected. Since the TMR is only sensitive to the properties of magnetic layers within essentially atomic thickness from the tunnel

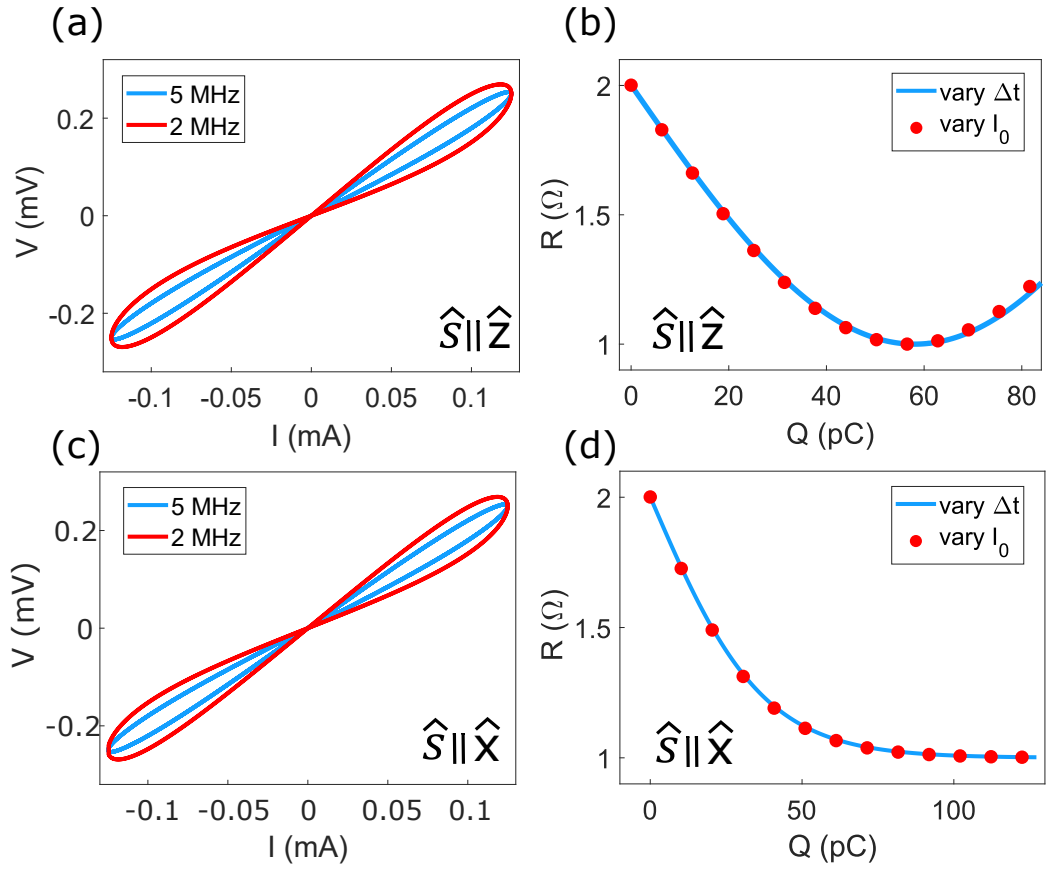

Figure 5.2: Results of simulations using Eq. (5.1) for a 5 nm-thick, 100 nm-diameter circular disk with $M_s = 800\ kA/m$, $P = 0.3$, $\alpha = 10$, and negligible in-plane anisotropy. $R_0 = 2\ \Omega$ and $\Delta R = 1\ \Omega$ were used for magnetoelectronic coefficients. (a),(c) IV hysteresis loop for $\hat{s} \parallel \hat{z}$ (a) and $\hat{s} \parallel \hat{x}$ (c), at two frequencies of sinusoidal driving current. (b),(d) Dependence of resistance variation on the total charge $Q = I_0 * \Delta t$ of the current pulses with varied amplitude I_0 at fixed duration $\Delta t = 100\ ns$ [curves], and varied Δt at fixed $I_0 = 0.24\ mA$ [dots], for $\hat{s} \parallel \hat{z}$ (b) and $\hat{s} \parallel \hat{x}$ (d), with $\varphi = 90°$ at $t = 0$.

junction, it is not expected to be affected by the additional AF interfaced with the F-layer on the side opposite to the tunnel junction. The TMR is determined by the angle φ between the magnetization of the free layer and the projection of the polarizer magnetization on the film plane, aproximately described by $R(\varphi) = R_0 + \Delta R cos(\varphi)$ [Fig. 5.1(b)]. $R(\varphi)$ is almost linear in the approximately 120° range of φ around 90°, as shown by a hatched region in Fig. 5.1(b). In this region, precession of $\hat{m}$ produces a nearly linear variation of R at a rate proportional to the current, i.e., the

resistance change is proportional to the total charge Q that flows through the device, as expected for an ideal memristor [138]. The memristive response, characterized by the slope of $R(Q)$, is tunable by varying α.

Our analysis is supported by numerical integration of Eq. (5.1) for sinusoidal driving current, which is common in the characterization of memristors [7, 151]. The pinched IV hysteresis [Fig. 5.2(a)] confirms memristive functionality. The hysteresis decreases with increasing ac current frequency f, as expected since the charge that flows through the device over any given part of the driving cycle is $\propto 1/f$. Figure 5.2(b) shows the calculated response to square current pulses of varied amplitude I_0 and duration Δt. The dependence $R(Q)$ is linear at small $Q = I_0\Delta t$, and is the same for the varied pulse amplitude as for the varied duration, confirming ideal memristive behaviors. At larger Q, the dependence becomes nonlinear and then non-monotonic due to φ exceeding 180°, resulting in the loss of memristive functionality.

This problem can be overcome by utilizing in-plane polarization $\hat{s}$. To analyze this case, we consider the overdamped limit $\alpha \gg 1$. The left-hand side of Eq. (5.1) is negligible compared to the Gilbert damping term. Taking a cross-product of Eq. (5.1) with $\hat{m}$, we obtain,

$$\alpha\frac{d\hat{m}}{dt} = -\mu_0\gamma\vec{H}_{eff} + \sigma_{DL}\hat{m}\times\hat{s} + \sigma_{FL}\hat{s}. \tag{5.3}$$

This equation describes a rotation of $\hat{m}$ towards the net effective field comprising $\vec{H}_{eff}$, the effective DL-STT field $\vec{H}_{DL} = -\sigma_{DL}\hat{m}\times\hat{s}/\mu_0\gamma$, and the effective FL-STT field $\vec{H}_{FL} = -\sigma_{FL}\hat{s}/\mu_0\gamma$. For in-plane $\hat{s}$, $\vec{H}_{DL}$ slightly tilts $\hat{m}$ out of plane, which can be neglected. Meanwhile, $\vec{H}_{FL}$ rotates $\hat{m}$ towards the orientation parallel or antiparallel to $\hat{s}$, depending on the sign of σ_{FL}.

The magnitude of FL-STT depends on the system's geometry and its electronic properties [27]. However, since only the FL-STT contributes to the dynamics dis-

cussed here, the specific relation between σ_{FL} and σ_{DL} is not important. For concreteness, we use the same value for σ_{FL} as for σ_{DL}. A different value of σ_{FL} is expected to simply rescale the characteristic currents required for the device operation, and does not influence the functionality of the proposed device.

Figure 5.2(c) shows that the IV curves exhibit the same hysteretic features as for $\hat{s} \parallel \hat{z}$. The dependence $R(Q)$ is linear at small Q, confirming ideal memristor functionality [Fig. 5.2(d)]. At large Q, the dependence $R(Q)$ saturates as $\hat{m}$ approaches $\hat{s}$, but does not become non-monotonic [Fig. 5.2(d)]. We note that saturation is expected for all memristors, otherwise their resistance would diverge or become negative. As an additional benefit of this configuration, TMR provides a more efficient readout of the memristor state. This mode of memristor operation can be also accomplished using spin-orbit torques, which can be described by in-plane $\hat{s}$ [152, 153].

5.4 The influence of shape anisotropy

We now analyze the effects of finite in-plane anisotropy, always present in real systems due to imperfections. For $\hat{s} \parallel \hat{z}$, OPP is expected to onset above some critical current density J_C at which STT overcomes the anisotropy. Consider easy y-axis uniaxial anisotropy characterized by anisotropy coefficient K_2. For a given K_2, the corresponding energy scales, such as the energy barrier between easy magnetization directions, scale with the size of the system.At $J < J_C$, STT-driven rotation of $\hat{m}$ is expected to stop at $\varphi_0 = sin^{-1}(2\sigma_{DL}/\mu_0\gamma K_2)/2$, obtained from Eq. (5.1) using $d\hat{m}/dt = 0$. The maximum possible value of $\varphi_0 = 45°$, at $\sigma_{DL} = \mu_0\gamma K_2/2$, corresponds to STT balancing the maximum anisotropy torque [148]. We note that OPP can onset at smaller σ_{DL} than obtained from the static balance, because the trajectory of $\hat{m}$ on the Bloch sphere need not pass through the attractor at $\varphi_0 = 45°$. Indeed, J_C obtained by numeric integration of Eq. (5.1) slightly decreases at small

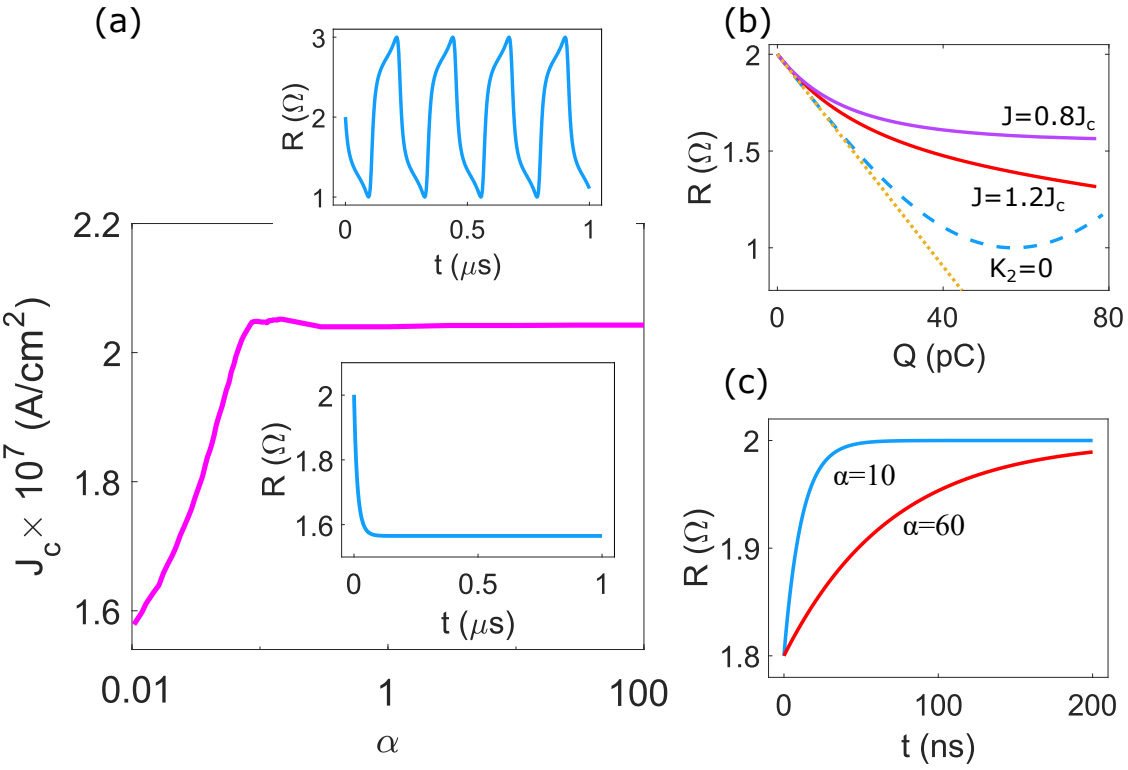

Figure 5.3: Effects of finite in-plane anisotropy. (a) Critical current density J_c for the onset of OPP mode vs α, for $K_2 = 4$ kA/m. Insets: $R(t)$ for $J = 0.8J_C$ (bottom), and $J = 1.2J_C$ (top), at $\alpha = 10$. (b) $R(Q)$ for square current pulses with varied duration, at $J = 0.8J_C$ and $1.2J_C$. The line shows the ideal memristive behavior, the dashed curve shows the result for negligible anisotropy. (d) $R(t)$ for $\varphi_0 = 20°$, at the labeled values of α.

α [Fig. 5.3(a)]. At large α relevant to this work, J_C saturates to a value consistent with the above analysis, and only slightly larger than its $\alpha = 0$ limit, confirming the possibility to efficiently drive viscous magnetization dynamics by STT.

In response to square current pulses, $R(Q)$ deviates from the ideal memristive behaviors more strongly than for the system with negligible anisotropy, due to the dependence of the anisotropy-induced torque on φ [Fig. 5.3(b)]. In the subcritical regime, the magnetization can rotate only up to φ_0, limiting the operational range. However, this regime may be beneficial for avoiding the non-monotonic behaviors that compromise memristive functionality. Another consequence of anisotropy is the relaxation of $\hat{m}$ towards the easy axis, resulting in memory loss at a rate dependent

on damping [Fig. 5.3(c)]. Using a trial solution $m_x = sin(Aexp(-t/t_1))$, $m_y = cos(Aexp(-t/t_1))$, $m_z = const$ of Eq. (5.1) at $I = 0$, with constant relaxation time t_1 and A, we obtain $t_1 = \alpha/K_2\mu_0\gamma$ for small deviations from equilibrium.

Memory loss can be minimized by utilizing a system where damping is very large in the absence of driving, but becomes smaller at finite current. This can be accomplished by interfacing the active F layer with an ultrathin low-anisotropy antiferromagnet (AF). Exchange frustration at the F/AF interface has been shown to result in the formation of a correlated spin glass at low temperature [154]. The energy landscape of this system is expected to span a wide range of scales that rapidly vary with temperature, as is generally observed for glass-forming systems [155]. Above the glass transition temperature $T = T_g$ [156, 154], The AF spin glass melts and forms viscous spin liquid, imparting large damping $\alpha \propto \nu$ to F [157] , which is highly tunable by temperature. The value of ν was shown to exponentially increase as T decreases towards T_g, with the latter determined by the thickness of AF [158].

Thanks to these properties, T can be used as the second memristor control parameter, with T_g tuned to achieve a large α in the absence of driving. Driving current increases the nanodevice temperature due to Joule heating, decreasing α and enabling STT-driven rotation of $\hat{m}$. The variation of α is affected by the temporal profile of the driving current, on the timescale of the thermal relaxation time τ. Below, we show that this dependence enables additional second-order memristive functionality beneficial for neuromorphic applications [159, 160].

5.5 Neuromorphic functionality of the device: STDP of non-overlapping pulses

To model these effects, we use the relaxation time approximation for the device temperature, $dT/dt = I^2R/C - (T - T_0)/\tau$, where C is the heat capacity, τ is the

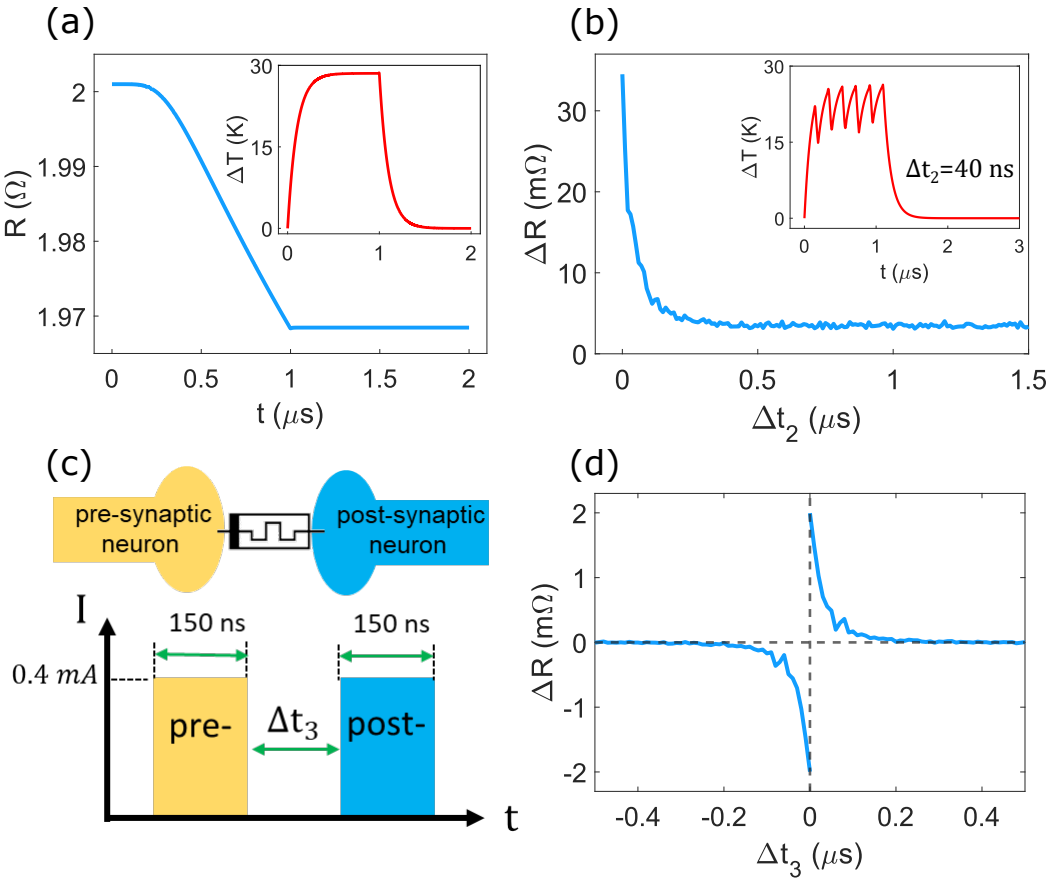

Figure 5.4: Effects of temperature-dependent damping in a spin glass-forming heterostructure. (a) R vs t for a 1 μs-long pulse of current $I_0 = 0.4$ mA. Inset: $\Delta T = T - T_0$ vs t. (b) Dependence of the resistance change driven by five 150 ns-long pulses of current $I_0 = 0.4$ mA with the interval Δt_2 between the pulses. Inset: T vs t for $\Delta t_2 = 40$ ns. (c) Schematic of the pre- and post- synaptic excitation pulses applied to the memristor. (d) Variation of resistance induced by the sequence of two pulses as a function of delay Δt_3.

thermal relaxation time, and T_0 is the temperature of the environment, and $\alpha(T) = \alpha(T_0)e^{a(T-T_0)}$ for the temperature dependence of damping, with $a = -0.46$ [157].

Figure 5.4(a) shows the time dependence of resistance in response to a square pulse of current. The pulse increases T by 30 K, as shown in the inset. The resulting decrease of damping enables STT-driven rotation of $\hat{m}$ by the pulse. The temperature decreases back to T_0 after the end of the pulse, resulting in negligible relaxation of $\hat{m}$ towards the easy axis. Because of the finite thermal relaxation time, the response to multiple current pulses depends on their relative timing, as illustrated in Fig. 5.4(b)

for sequential pulses. For small delay between the pulses, the temperature increase driven by a pulse remains significant at the onset of the subsequent pulse [inset in Fig. 5.4(b)], resulting in a larger response to the latter. Thus, current-driven temperature variation serves as an additional state control variable, which provides second-order memristive functionality - dependence of the final device state on the timing of the driving current pulses.

This feature can be particularly beneficial for synaptic functions. In real neural systems, the synaptic plasticity is controlled by the relative timing of the voltage spikes, which is realized by the sensitivity modulation mediated by the spike-driven Ca^{2+} ion concentration [161, 162]. The release and the spontaneous decay of Ca^{2+} results in the effective summation of closely timed pulses, leading to spike timing-dependent plasticity (STDP), which plays an important role in the neural network's functionality. The relaxation of temperature in the proposed memristive devices closely emulates the decay of Ca^{2+} concentration in neural networks, providing a simple and efficient implementation of STDP with non-overlapping pulses.

As a proof-of-principle demonstration of second-order memristive functionality, we simulate the response of the proposed memristor to non-overlapping pre- and post- synaptic pulses. For simplicity, only square pulses are considered. Pre- and post- synaptic pulses, with 0.4 mA amplitude and 150 ns length, are applied to the memristor with a varied delay Δt_3 between the pulses [Fig. 5.4(c)]. The variation of resistance after both pulses is plotted in Fig. 5.4(d) as a function of Δt_3.

Depending on the sign of Δt_3, the synapse experiences potentiation or depression. To analyze the physical mechanism accounting for this STDP functionality, we note that the pre- and post- synapse pulses rotate the magnetization of the free layer in opposite directions. However, the temperature of the system is low at the onset of the first pulse, so the damping is large. Thus, the first pulse does not induce a significant rotation of the free layer, and only acts as a "heating pulse". If the second pulse comes

within the thermal relaxation time, the temperature of the system is still elevated, and the damping is reduced. The efficiency of rotation of magnetization by the second pulse is then significantly enhanced. Thus, the total variation of resistance is only determined by the second pulse. Depending on whether the second pulse is pre- or post- synapse, the variation of resistance can be positive (potentiation) or negative (depression).

Chapter 6

Summary

In this thesis, we mainly focus on the nonequilibrium phenomena in electronic and magnetic nano-scale systems. To be specific, in the chapter about "Nonequilibrium phonon distribution in current-driven nano- and micro-structures", our measurements and analysis have demonstrated that the phonons generated by electric current in conducting microstructures characterized by efficient thermal dissipation, generally form a strongly nonequilibrium distribution that cannot be described by a temperature. The nonequilibirum distribution is manifested by the linear dependence of resistance on current qualitatively inconsistent with the expected effects of Joule heating. The linear dependence is observed at sufficiently high currents at temperatures as high as 200 K. The dependence of the observed phenomena on the structure, geometry, substrate and interface properties, and temperature can provide unique information about the electron-phonon scattering, phonon relaxation rates and mechanisms, and thermal effects.

The most important message of our work is that on the microscopic level, scattering of electrons driven by electric bias generates phonons with a non-thermal distribution, whose contribution to resistance and other material properties can be qualitatively different from those expected for Joule heating. This result is expected to

have broad implications for the optimization of thermal properties of electronic devices and nanostructures, and for the studies of current-induced phenomena. For instance, at high current densities, the linear dependence $R(I)$ associated with the non-equilibrium phonon distribution can fall significantly below the approximately quadratic dependence expected for Joule heating. In this regime, the average energy of phonons generated by current is larger than that of thermal phonons described by Joule heating, but their population is smaller than the thermalized population with the same total energy. This regime may be advantageous for the optimization of thermal management in nanoscale devices, for several reasons. First, additional energy dissipation due to electron scattering on the generated phonons can be significantly smaller than in the Joule heating limit, reducing the possibility of thermal runaway [52]. Second, the escape of the generated nonequilibrium phonons from the system can be more efficient than for Joule heating, due to the smaller rates of phonon-phonon scattering. Finally, the generated high-frequency phonons are less likely to contribute to current-induced physical degradation associated with the slow metastable mechanical degrees of freedom.

Current-induced phenomena have been extensively studied in the context of spin Hall effect, in thin Pt films similar to those discussed in our work [56, 57, 58, 38, 59, 60]. Our results may warrant re-examination of the Joule heating effects in these experiments. Similarly, low-temperature thermoelectric measurements at nanoscale commonly employ resistive heating of wires similar to those analyzed in our study.

As a follow up, in the chapter about "Transport and relaxation of current-generated nonequilibrium phonons from nonlocal electronic measurements", a nonlocal measurement is applied, which enables the investigation of the propagation and relaxation of the highly nonequilibrium phonons. Here, we studied non-equilibrium phonons generated by current in a "source" Pt nanowire, by measuring the resistance of a "sensing" nanowire insulated from the source by a SiO_2 spacer. At cryogenic temperatures,

the dependence of resistance on current can be precisely fitted by the sum of a linear and a quadratic function. The linear contribution exponentially decreases, while the quadratic one similarly increases with increasing spacer thickness. We interpret these results as evidence for a highly non-thermal distribution of current-generated phonons, which relax by inelastic scattering mediated by strongly anharmonic defects that alleviate the constraints imposed by the quasiparticle momentum and energy conservation. Our results suggest a new route for the characterization of nonequilibrium current-generated phonons, and for optimizing Joule heat management in electronic nanodevices.

In the fourth chapter, the nonequilibrium (glassy like), behavior of magnetization in FM/AF hetero-structure is investigated. Here, due to the complicated energy landscape induced by the random interfacial coupling, our experiment suggests that the magnetization in FM layer is likely in frustrated Heisenberg domain state, where magnetization is twisted through out the film. To summarize our findings, we have developed a new method for studying random effective exchange fields at magnetic interfaces. Our method utilizes measurements of deviations from saturation characterized by $\langle \varphi^2 \rangle$ - the average of the square of the angle between the magnetization and the external field - which follows a power-law dependence on the applied field with the exponent dependent on the characteristics of the exchange field. For the random effective exchange field correlated on the length scales exceeding the magnetic correlation length, the exponent is different from that for the uncorrelated random field, allowing one to distinguish between these two limiting cases. Moreover, the power-law exponent varies as a function of the film thickness, due to the correlations associated with averaging of the effective random field through the magnetic film thickness. By extension, we expect that the specific value of the power-law exponent for a given film thickness, if known precisely, can be utilized to determine the correlation length of random field.

Our results are expected to have broader impact on the studies and applications of thin magnetic film systems. First, the effective exchange field in F/AF bilayers, which is the focus of our study, is just one specific case of many magnetic interfacial effects extensively researched and commonly utilized in the existing and emerging technologies. Those include the Ruderman–Kittel–Kasuya–Yosida (RKKY) interaction commonly employed in magnetic multilayer sensors and in artificial antiferromagnets, interfacial magnetic anisotropies commonly utilized to induce perpendicular magnetic anisotropy in magnetic heterostructures, and the interfacial Dzyaloshinski-Moriya interaction [94, 97, 131]. Understanding the spatial characteristics of these effects is crucial for the development of efficient and reproducible nanodevices. We note that the magnetic anisotropy is equivalent to effective fields for small-angle variations of magnetization, and therefore can be analyzed using the same approach as introduced above.

Finally, we mention some of the projected fundamental insights that can become facilitated by our work. Our demonstration of uncorrelated effective random field effects in F/AF heterostructures opens the possibility to explore important fundamental consequences of these effects, such as topologically nontrivial magnetization states [125, 124]. Such states can profoundly affect the magnetic properties, but to the best of our knowledge, their effects in F/AF heterostructures have not yet been explored. Another potentially profound consequence of magnetic frustration associated with uncorrelated effective random fields is the possibility to engineer magnetic energy landscapes whose energy scale is determined by the exchange interaction, rather than the magnetic anisotropy as in unfrustrated magnetic systems. The former is three to four orders of magnitude larger than the latter, providing a unique opportunity to develop ultrasmall thermally stable nanomagnetic devices.

As a follow up, in the next chapter, based on our new understanding of the random interaction at FM/AF interface, we proposed a magnetic realization of ideal

memristor. In this work, we have demonstrated the possibility to implement nearly ideal memristive behaviors characterized by a linear dependence of a two-terminal device resistance on the charge that flows through it, by utilizing spin torque-driven viscous magnetization dynamics. The latter property can be achieved by utilizing a spin glass-forming hybrid heterostructure with frustrated exchange interactions, which also enables non-volatile operation and the implementation of spike timing-dependent plasticity with non-overlapping pulses, due to Joule heating and the strong dependence of damping on temperature. Together with the expected high-endurance of magnetism-based memristor implementation, these characteristics make the proposed devices particularly attractive for the hardware implementation of synaptic functions in artificial neural networks.

Bibliography

[1] Roman Anufriev, Aymeric Ramiere, Jeremie Maire, and Masahiro Nomura. Heat guiding and focusing using ballistic phonon transport in phononic nanostructures. *Nature communications*, 8(1):1–8, 2017.

[2] Anil Prabhakar and Daniel D Stancil. *Spin waves*. Springer US, 2009.

[3] Ralph Skomski. Nanomagnetics. *Journal of Physics: Condensed Matter*, 15(20):R841, 2003.

[4] Li-Cong Peng, Ying Zhang, Shu-Lan Zuo, Min He, Jian-Wang Cai, Shou-Guo Wang, Hong-Xiang Wei, Jian-qi Li, Tong-yun Zhao, and Bao-gen Shen. Lorentz transmission electron microscopy studies on topological magnetic domains. *Chinese Physics B*, 27(6):066802, 2018.

[5] Pauline Dufour. Moke microscope measurements ofmagnetic domains in microstructuresof fe80zr10b10, 2018.

[6] Yu Chen, Gang Liu, Cheng Wang, Wenbin Zhang, Run-Wei Li, and Luxing Wang. Polymer memristor for information storage and neuromorphic applications. *Materials Horizons*, 1(5):489–506, 2014.

[7] Dmitri B Strukov, Gregory S Snider, Duncan R Stewart, and R Stanley Williams. The missing memristor found. *nature*, 453(7191):80–83, 2008.

[8] M Asheghi, MN Touzelbaev, KE Goodson, YK Leung, and SS Wong. Temperature-Dependent Thermal Conductivity of Single-Crystal Silicon Layers in SOI Substrates. *Journal of Heat Transfer*, 120(1):30–36, 1998.

[9] Elena R Dobrovinskaya, Leonid A Lytvynov, and Valerian Pishchik. *Sapphire: Material, Manufacturing, Applications*. Springer Science & Business Media, 2009.

[10] CJ Glassbrenner and Glen A Slack. Thermal Conductivity of Silicon and Germanium from 3 K to the Melting Point. *Phys. Rev.*, 134(4A):A1058, 1964.

[11] L. D. Landau and E. M. Lifshitz. *Mechanics, Third Edition: Volume 1 (Course of Theoretical Physics)*. Butterworth-Heinemann, 3 edition, 1976.

[12] Neil W Ashcroft, N David Mermin, et al. Solid state physics, 1976.

[13] Lin Yang, Qian Zhang, Zhiguang Cui, Matthew Gerboth, Yang Zhao, Terry T Xu, D Greg Walker, and Deyu Li. Ballistic phonon penetration depth in amorphous silicon dioxide. *Nano letters*, 17(12):7218–7225, 2017.

[14] Tianli Feng and Xiulin Ruan. Prediction of spectral phonon mean free path and thermal conductivity with applications to thermoelectrics and thermal management: a review. *Journal of Nanomaterials*, 2014, 2014.

[15] Keith T Regner, Daniel P Sellan, Zonghui Su, Cristina H Amon, Alan JH McGaughey, and Jonathan A Malen. Broadband phonon mean free path contributions to thermal conductivity measured using frequency domain thermoreflectance. *Nature communications*, 4(1):1–7, 2013.

[16] Rodrigo A Escobar, Sartaj S Ghai, Myung S Jhon, and Cristina H Amon. Multi-length and time scale thermal transport using the lattice boltzmann method

with application to electronics cooling. *International Journal of Heat and Mass Transfer*, 49(1-2):97–107, 2006.

[17] Sreekant VJ Narumanchi, Jayathi Y Murthy, and Cristina H Amon. Simulation of unsteady small heat source effects in sub-micron heat conduction. *J. Heat Transfer*, 125(5):896–903, 2003.

[18] Per G Sverdrup, Y Sungtaek Ju, and Kenneth E Goodson. Sub-continuum simulations of heat conduction in silicon-on-insulator transistors. *J. Heat Transfer*, 123(1):130–137, 2001.

[19] Robert C O'handley. *Modern magnetic materials: principles and applications*. Springer US, 1999.

[20] Masamitsu Hayashi, Luc Thomas, Charles Rettner, Rai Moriya, Xin Jiang, and Stuart SP Parkin. Dependence of current and field driven depinning of domain walls on their structure and chirality in permalloy nanowires. *Physical review letters*, 97(20):207205, 2006.

[21] Börge Göbel, Ingrid Mertig, and Oleg A Tretiakov. Beyond skyrmions: Review and perspectives of alternative magnetic quasiparticles. *Physics Reports*, 895:1–28, 2021.

[22] Alberto P Guimarães and Alberto Passos Guimaraes. *Principles of nanomagnetism*, volume 7. Springer, 2009.

[23] S Imada, S Suga, W Kuch, and J Kirschner. Magnetic microspectroscopy by a combination of xmcd and peem. *Surface Review and Letters*, 9(02):877–881, 2002.

[24] D Rugar, HJ Mamin, P Guethner, SE Lambert, JE Stern, I McFadyen, and

T Yogi. Magnetic force microscopy: General principles and application to longitudinal recording media. *Journal of Applied Physics*, 68(3):1169–1183, 1990.

[25] Shan X Wang and Guanxiong Li. Advances in giant magnetoresistance biosensors with magnetic nanoparticle tags: Review and outlook. *IEEE transactions on Magnetics*, 44(7):1687–1702, 2008.

[26] Arne Vansteenkiste, Jonathan Leliaert, Mykola Dvornik, Mathias Helsen, Felipe Garcia-Sanchez, and Bartel Van Waeyenberge. The design and verification of mumax3. *AIP advances*, 4(10):107133, 2014.

[27] Daniel C Ralph and Mark D Stiles. Spin transfer torques. *Journal of Magnetism and Magnetic Materials*, 320(7):1190–1216, 2008.

[28] Andrew Adamatzky and Leon Chua. *Memristor networks*. Springer Science & Business Media, 2013.

[29] Miroslav Grajcar, Andrej Plecenik, Paul Seidel, Viktor Vojtanik, and Kai-Uwe Barholz. Asymmetry and quasilinear background of differential conductance characteristics of high-T_c-superconductor/metal tunnel junctions. *Phys. Rev. B*, 55:11738–11744, May 1997.

[30] Alan B Kaiser, Cristina Gómez-Navarro, Ravi S Sundaram, Marko Burghard, and Klaus Kern. Electrical Conduction Mechanism in Chemically Derived Graphene Monolayers. *Nano Letters*, 9(5):1787–1792, 2009.

[31] C. Canali, G. Majni, R. Minder, and G. Ottaviani. Electron and hole drift velocity measurements in silicon and their empirical relation to electric field and temperature. *IEEE Transactions on Electron Devices*, 22(11):1045–1047, Nov 1975.

[32] M Battiato, V Zlatic, and K Held. Boltzmann approach to high-order transport: The nonlinear and nonlocal responses. *Phys. Rev. B*, 95(23):235137, 2017.

[33] Andrew Zangwill. *Modern Electrodynamics*. Cambridge University Press, 2013.

[34] Herbert P Neff. *Introductory Electromagnetics*. Wiley, 1991.

[35] Jean-Philippe Ansermet and Sylvain D Bréchet. *Principles of Thermodynamics*. Cambridge University Press, 2019.

[36] Zhe Cheng, Longju Liu, Shen Xu, Meng Lu, and Xinwei Wang. Temperature Dependence of Electrical and Thermal Conduction in Single Silver Nanowire. *Scientific Reports*, 5:10718, 2015.

[37] I. N. Krivorotov, N. C. Emley, A. G. F. Garcia, J. C. Sankey, S. I. Kiselev, D. C. Ralph, and R. A. Buhrman. Temperature Dependence of Spin-Transfer-Induced Switching of Nanomagnets. *Phys. Rev. Lett.*, 93:166603, Oct 2004.

[38] R. H. Liu, W. L. Lim, and S. Urazhdin. Spectral Characteristics of the Microwave Emission by the Spin Hall Nano-Oscillator. *Phys. Rev. Lett.*, 110:147601, Apr 2013.

[39] Eric Pop, Sanjiv Sinha, and Kenneth E Goodson. Heat Generation and Transport in Nanometer-Scale Transistors. *Proceedings of the IEEE*, 94(8):1587–1601, 2006.

[40] Eric Pop. Energy dissipation and transport in nanoscale devices. *Nano Research*, 3(3):147–169, 2010.

[41] Ashutosh Giri, John T Gaskins, Brian F Donovan, Chester Szwejkowski, Ronald J Warzoha, Mark A Rodriguez, Jon Ihlefeld, and Patrick E Hopkins. Mechanisms of nonequilibrium electron-phonon coupling and thermal conductance at interfaces. *Journal of Applied Physics*, 117(10):105105, 2015.

[42] Shota Ono. Thermalization in simple metals: Role of electron-phonon and phonon-phonon scattering. *Phys. Rev. B*, 97(5):054310, 2018.

[43] M. L. Roukes, M. R. Freeman, R. S. Germain, R. C. Richardson, and M. B. Ketchen. Hot electrons and energy transport in metals at millikelvin temperatures. *Phys. Rev. Lett.*, 55:422–425, Jul 1985.

[44] F. C. Wellstood, C. Urbina, and John Clarke. Hot-electron effects in metals. *Phys. Rev. B*, 49:5942–5955, Mar 1994.

[45] Andrew H. Steinbach, John M. Martinis, and Michel H. Devoret. Observation of Hot-Electron Shot Noise in a Metallic Resistor. *Phys. Rev. Lett.*, 76:3806–3809, May 1996.

[46] Suvranta K Tripathy, Guibao Xu, Xiaodong Mu, Yujie J Ding, Kejia Wang, Yu Cao, Debdeep Jena, and Jacob B Khurgin. Evidence of hot electrons generated from an Al N/ Ga N high electron mobility transistor. *Applied Physics Letters*, 92(1):013513, 2008.

[47] Isabel Klett and Baerbel Rethfeld. Relaxation of a nonequilibrium phonon distribution induced by femtosecond laser irradiation. *Phys. Rev. B*, 98(14):144306, 2018.

[48] J.A. Kash, J.C. Tsang, and J.M. Hvam. Subpicosecond Time-Resolved Raman Spectroscopy of LO Phonons in GaAs. *Phys. Rev. Lett.*, 54(19):2151, 1985.

[49] N Del Fatti, C Voisin, M Achermann, S Tzortzakis, D Christofilos, and F Vallée. Nonequilibrium electron dynamics in noble metals. *Phys. Rev. B*, 61(24):16956, 2000.

[50] Pamela M Norris, Andrew P Caffrey, Robert J Stevens, J Michael Klopf, James T McLeskey Jr, and Andrew N Smith. Femtosecond pump–probe nonde-

structive examination of materials. *Review of scientific instruments*, 74(1):400–406, 2003.

[51] Jiajun Li and Jong E. Han. Nonequilibrium excitations and transport of Dirac electrons in electric-field-driven graphene. *Phys. Rev. B*, 97:205412, May 2018.

[52] L. Siddiqui, A. W. Ghosh, and S. Datta. Phonon runaway in carbon nanotube quantum dots. *Phys. Rev. B*, 76:085433, Aug 2007.

[53] T Chase, M Trigo, AH Reid, R Li, T Vecchione, X Shen, S Weathersby, R Coffee, N Hartmann, DA Reis, et al. Ultrafast electron diffraction from non-equilibrium phonons in femtosecond laser heated au films. *Applied Physics Letters*, 108(4):041909, 2016.

[54] A. X. Gray, M. C. Hoffmann, J. Jeong, N. P. Aetukuri, D. Zhu, H. Y. Hwang, N. C. Brandt, H. Wen, A. J. Sternbach, S. Bonetti, et al. Ultrafast terahertz field control of electronic and structural interactions in vanadium dioxide. *Phys. Rev. B*, 98:045104, Jul 2018.

[55] S. Huberman, R. A. Duncan, K. Chen, B. Song, V. Chiloyan, Z. Ding, A. A. Maznev, G. Chen, and K. A. Nelson. Observation of second sound in graphite at temperatures above 100 K. *Science*, 364(6438):375–379, 2019.

[56] Luqiao Liu, Takahiro Moriyama, D. C. Ralph, and R. A. Buhrman. Spin-Torque Ferromagnetic Resonance Induced by the Spin Hall Effect. *Phys. Rev. Lett.*, 106:036601, Jan 2011.

[57] Tomas Jungwirth, Jörg Wunderlich, and Kamil Olejník. Spin Hall effect devices. *Nature Materials*, 11(5):382, 2012.

[58] K. Ando, S. Takahashi, K. Harii, K. Sasage, J. Ieda, S. Maekawa, and E. Saitoh.

Electric Manipulation of Spin Relaxation Using the Spin Hall Effect. *Phys. Rev. Lett.*, 101:036601, Jul 2008.

[59] VE Demidov, S Urazhdin, A Zholud, AV Sadovnikov, and SO Demokritov. Nanoconstriction-based spin-Hall nano-oscillator. *Applied Physics Letters*, 105(17):172410, 2014.

[60] Meiyin Yang, Kaiming Cai, Hailang Ju, Kevin William Edmonds, Guang Yang, Shuai Liu, Baohe Li, Bao Zhang, Yu Sheng, Shouguo Wang, et al. Spin-orbit torque in Pt/CoNiCo/Pt symmetric devices. *Scientific Reports*, 6:20778, 2016.

[61] Jun-gu Kang, Joon-Shik Park, Kwang-Bum Park, Junho Shin, Eung-An Lee, Sangsoo Noh, and Hoo-Jeong Lee. Temperature control of micro heater using Pt thin film temperature sensor embedded in micro gas sensor. *Micro and Nano Systems Letters*, 5(1):26, Sep 2017.

[62] Shibesh Dutta, Kiroubanand Sankaran, Kristof Moors, Geoffrey Pourtois, Sven Van Elshocht, Jürgen Bömmels, Wilfried Vandervorst, Zsolt Tőkei, and Christoph Adelmann. Thickness dependence of the resistivity of platinum-group metal thin films. *Journal of Applied Physics*, 122(2):025107, July 2017.

[63] H. Pothier, S. Guéron, Norman O. Birge, and D. Esteve. Energy distribution of electrons in an out-of-equilibrium metallic wire. *Zeitschrift für Physik B Condensed Matter*, 103(2):313–318, June 1996.

[64] Roland Wiesendanger. *Scanning Probe Microscopy and Spectroscopy.* Cambridge University Press, 1994.

[65] R Gereth and K Hubner. Phonon Mean Free Path in Silicon Between 77 and 250 K. *Phys. Rev.*, 134(1A):A235, 1964.

[66] Nevill Francis Mott and Harry Jones. *The Theory of the Properties of Metals and Alloys*. Courier Corporation, 1958.

[67] Charles Kittel. *Introduction to Solid State Physics*. John Wiley & Sons, New York, 8 edition, 2005.

[68] J. B. Ketterson and L. R. Windmiller. de Haas-van Alphen Effect in Platinum. *Phys. Rev. B*, 2:4813–4838, Dec 1970.

[69] Andrei Zholud, Ryan Freeman, Rongxing Cao, Ajit Srivastava, and Sergei Urazhdin. Spin Transfer due to Quantum Magnetization Fluctuations. *Phys. Rev. Lett.*, 119:257201, Dec 2017.

[70] WA Little. The Transport of Heat Between Dissimilar Solids at Low Temperatures. *Canadian Journal of Physics*, 37(3):334–349, 1959.

[71] Keith T Regner, Daniel P Sellan, Zonghui Su, Cristina H Amon, Alan JH McGaughey, and Jonathan A Malen. Broadband phonon mean free path contributions to thermal conductivity measured using frequency domain thermoreflectance. *Nature communications*, 4(1):1–7, 2013.

[72] Olivier Bourgeois, Dimitri Tainoff, Adib Tavakoli, Yanqing Liu, Christophe Blanc, Mustapha Boukhari, André Barski, and Emmanuel Hadji. Reduction of phonon mean free path: From low-temperature physics to room temperature applications in thermoelectricity. *Comptes Rendus Physique*, 17(10):1154–1160, 2016.

[73] Yongjie Hu, Lingping Zeng, Austin J Minnich, Mildred S Dresselhaus, and Gang Chen. Spectral mapping of thermal conductivity through nanoscale ballistic transport. *Nature nanotechnology*, 10(8):701, 2015.

[74] Charles Kittel. Introduction to solid state physics. 1976.

[75] Guanxiong Chen, Ryan Freeman, Andrei Zholud, and Sergei Urazhdin. Observation of anomalous non-ohmic transport in current-driven nanostructures. *Physical Review X*, 10(1):011064, 2020.

[76] Charles Kittel. Interpretation of the thermal conductivity of glasses. *Physical Review*, 75(6):972, 1949.

[77] John M Ziman. *Electrons and phonons: the theory of transport phenomena in solids*. Oxford university press, 2001.

[78] Yangyu Guo, Marc Bescond, Zhongwei Zhang, Mathieu Luisier, Masahiro Nomura, and Sebastian Volz. Quantum mechanical modeling of anharmonic phonon-phonon scattering in nanostructures. *Phys. Rev. B*, 102:195412, Nov 2020.

[79] Runqing Yang, Shengying Yue, Yujie Quan, and Bolin Liao. Crystal-symmetry-based selection rules for anharmonic phonon-phonon scattering from a group theory formalism. *arXiv preprint arXiv:2103.02769*, 2021.

[80] A. Akhiezer. On the absorption of sound in solids. *J. Phys. USSR*, 1:277, 1939.

[81] L. Zhang, Y. Wang, Y. Chen, J. Shang, A. Sun, X. Sun, S. Yu, J. Zheng, Y. Wang, W. Schirmacher, and J. Zhang. Disorder-induced vibrational anomalies from crystalline to amorphous solids. *arXiv preprint arXiv:2104.13142*, 2021.

[82] Shivam Mahajan and Massimo Pica Ciamarra. Unifying description of the vibrational anomalies of amorphous materials. *arXiv preprint arXiv:2106.04868*, 2021.

[83] Zeng-Yu Yang, Yun-Jiang Wang, and Alessio Zaccone. Giant anharmonicity

controls terahertz vibrations and the boson peak anomaly in disordered materials. *arXiv preprint arXiv:2104.13740*, 2021.

[84] Joseph L. Feldman, Mark D. Kluge, Philip B. Allen, and Frederick Wooten. Thermal conductivity and localization in glasses: Numerical study of a model of amorphous silicon. *Phys. Rev. B*, 48:12589–12602, Nov 1993.

[85] Philip B. Allen, Joseph L. Feldman, Jaroslav Fabian, and Frederick Wooten. Diffusons, locons and propagons: Character of atomic vibrations in amorphous si. *Philosophical Magazine B*, 79(11-12):1715–1731, November 1999.

[86] Robert O Pohl, Xiao Liu, and EunJoo Thompson. Low-temperature thermal conductivity and acoustic attenuation in amorphous solids. *Reviews of Modern Physics*, 74(4):991, 2002.

[87] M Molina-Ruiz, HC Jacks, DR Queen, TH Metcalf, X Liu, and F Hellman. Decoupling between propagating acoustic waves and two-level systems in hydrogenated amorphous silicon. *arXiv preprint arXiv:2105.02513*, 2021.

[88] Jaeyun Moon. Examining normal modes as fundamental heat carriers in amorphous solids: the case of amorphous silicon. *arXiv preprint arXiv:2106.08459*, 2021.

[89] Shinji Yuasa, Taro Nagahama, Akio Fukushima, Yoshishige Suzuki, and Koji Ando. Giant room-temperature magnetoresistance in single-crystal fe/MgO/fe magnetic tunnel junctions. *Nature Materials*, 3(12):868–871, October 2004.

[90] Stuart S. P. Parkin, Christian Kaiser, Alex Panchula, Philip M. Rice, Brian Hughes, Mahesh Samant, and See-Hun Yang. Giant tunnelling magnetoresistance at room temperature with MgO (100) tunnel barriers. *Nature Materials*, 3(12):862–867, October 2004.

[91] Sankha S Mukherjee, Feiming Bai, David MacMahon, Chih-Ling Lee, Surendra K Gupta, and Santosh K Kurinec. Crystallization and grain growth behavior of cofeb and mgo layers in multilayer magnetic tunnel junctions. *Journal of Applied Physics*, 106(3):033906, 2009.

[92] Jun Hayakawa, Shoji Ikeda, Fumihiro Matsukura, Hiromasa Takahashi, and Hideo Ohno. Dependence of giant tunnel magnetoresistance of sputtered cofeb/mgo/cofeb magnetic tunnel junctions on mgo barrier thickness and annealing temperature. *Japanese Journal of Applied Physics*, 44(4L):L587, 2005.

[93] W. H. Meiklejohn and C. P. Bean. New magnetic anisotropy. *Phys. Rev.*, 105:904–913, Feb 1957.

[94] Carl Heck. *Magnetic materials and their applications*. Elsevier, 2013.

[95] Johan Åkerman. Toward a universal memory. *Science*, 308(5721):508–510, 2005.

[96] Jia-Mian Hu, Zheng Li, Long-Qing Chen, and Ce-Wen Nan. High-density magnetoresistive random access memory operating at ultralow voltage at room temperature. *Nature communications*, 2:553, 2011.

[97] Claude Chappert, Albert Fert, and Frédéric Nguyen Van Dau. The emergence of spin electronics in data storage. In *Nanoscience And Technology: A Collection of Reviews from Nature Journals*, pages 147–157. World Scientific, 2010.

[98] T. Jungwirth, X. Marti, P. Wadley, and J. Wunderlich. Antiferromagnetic spintronics. *Nature Nanotechnology*, 11(3):231–241, mar 2016.

[99] Jairo Sinova and Igor Žutić. New moves of the spintronics tango. *Nature materials.*, 11(5):368–371, 2012.

[100] Junichi Nishitani, Kohei Kozuki, Takeshi Nagashima, and Masanori Hangyo.

Terahertz radiation from coherent antiferromagnetic magnons excited by femtosecond laser pulses. *Applied Physics Letters*, 96(22):221906, may 2010.

[101] S. Ghosh and A. Manchon. Spin-orbit torque in two-dimensional antiferromagnetic topological insulators. *Phys. Rev. B*, 95:035422, Jan 2017.

[102] A. Scholl, M. Liberati, E. Arenholz, H. Ohldag, and J. Stöhr. Creation of an antiferromagnetic exchange spring. *Phys. Rev. Lett.*, 92:247201, Jun 2004.

[103] H. Reichlová, D. Kriegner, V. Holý, K. Olejník, V. Novák, M. Yamada, K. Miura, S. Ogawa, H. Takahashi, T. Jungwirth, and J. Wunderlich. Current-induced torques in structures with ultrathin irmn antiferromagnets. *Phys. Rev. B*, 92:165424, Oct 2015.

[104] Wei Zhang, Matthias B. Jungfleisch, Wanjun Jiang, John E. Pearson, Axel Hoffmann, Frank Freimuth, and Yuriy Mokrousov. Spin hall effects in metallic antiferromagnets. *Phys. Rev. Lett.*, 113:196602, Nov 2014.

[105] Shunsuke Fukami, Chaoliang Zhang, Samik DuttaGupta, Aleksandr Kurenkov, and Hideo Ohno. Magnetization switching by spin–orbit torque in an antiferromagnet–ferromagnet bilayer system. *Nature Materials*, 15(5):535–541, February 2016.

[106] Weiwei Lin and C. L. Chien. Electrical detection of spin backflow from an antiferromagnetic insulator/$y_3fe_5o_{12}$ interface. *Phys. Rev. Lett.*, 118:067202, Feb 2017.

[107] Arati Prakash, Jack Brangham, Fengyuan Yang, and Joseph P. Heremans. Spin seebeck effect through antiferromagnetic nio. *Phys. Rev. B*, 94:014427, Jul 2016.

[108] Roman Khymyn, Ivan Lisenkov, Vasyl Tiberkevich, Boris A. Ivanov, and Andrei

Slavin. Antiferromagnetic THz-frequency josephson-like oscillator driven by spin current. *Scientific Reports*, 7:43705, mar 2017.

[109] J Nogués and Ivan K Schuller. Exchange bias. *Journal of Magnetism and Magnetic Materials*, 192(2):203–232, February 1999.

[110] D. Mauri, H. C. Siegmann, P. S. Bagus, and E. Kay. Simple model for thin ferromagnetic films exchange coupled to an antiferromagnetic substrate. *Journal of Applied Physics*, 62(7):3047–3049, October 1987.

[111] U. Nowak, K. D. Usadel, J. Keller, P. Miltényi, B. Beschoten, and G. Güntherodt. Domain state model for exchange bias. i. theory. *Phys. Rev. B*, 66:014430, Jul 2002.

[112] C. Schlenker, S.S.P. Parkin, J.C. Scott, and K. Howard. Magnetic disorder in the exchange bias bilayered FeNi-FeMn system. *Journal of Magnetism and Magnetic Materials*, 54-57:801–802, February 1986.

[113] T K Yamada, E Martínez, A Vega, R Robles, D Stoeffler, A L Vázquez de Parga, T Mizoguchi, and H van Kempen. Spin configuration in a frustrated ferromagnetic/antiferromagnetic thin-film system. *Nanotechnology*, 18(23):235702, May 2007.

[114] JF Ding, OI Lebedev, S Turner, YF Tian, WJ Hu, JW Seo, C Panagopoulos, Wilfrid Prellier, G Van Tendeloo, and T Wu. Interfacial spin glass state and exchange bias in manganite bilayers with competing magnetic orders. *Physical Review B*, 87(5):054428, 2013.

[115] AP Malozemoff. Random-field model of exchange anisotropy at rough ferromagnetic-antiferromagnetic interfaces. *Physical review B*, 35(7):3679, 1987.

[116] Yoseph Imry and Shang-keng Ma. Random-field instability of the ordered state of continuous symmetry. *Phys. Rev. Lett.*, 35:1399–1401, Nov 1975.

[117] A. P. Malozemoff. Heisenberg-to-ising crossover in a random-field model with uniaxial anisotropy. *Phys. Rev. B*, 37:7673–7679, May 1988.

[118] A. E. P. de Araújo, F. L. A. Machado, A. R. Rodrigues, A. Azevedo, F. M. de Aguiar, J. R. L. de Almeida, S. M. Rezende, and W. F. Egelhoff. Spin-glass and random-field effects in exchange-biased nife film on a nio single-crystal substrate. *Journal of Applied Physics*, 91(10):7754–7756, 2002.

[119] E Jiménez, Julio Camarero, J Sort, J Nogués, N Mikuszeit, José Miguel García-Martín, A Hoffmann, B Dieny, and R Miranda. Emergence of noncollinear anisotropies from interfacial magnetic frustration in exchange-bias systems. *Physical Review B*, 80(1):014415, 2009.

[120] Sergei Urazhdin and U Danilenko. Cooperative multiscale aging in a ferromagnet/antiferromagnet bilayer. *Physical Review B*, 92(17):174416, 2015.

[121] Tianyu Ma, Xiang Cheng, Stefan Boettcher, Sergei Urazhdin, and Lydia Novozhilova. Thickness-dependent cooperative aging in polycrystalline films of antiferromagnet coo. *Phys. Rev. B*, 94:024422, Jul 2016.

[122] Tianyu Ma and Sergei Urazhdin. Spin glass transition in a thin-film nio/permalloy bilayer. *Phys. Rev. B*, 97:054402, Feb 2018.

[123] Sergei Urazhdin, Weijie Li, and Lydia Novozhilova. Magnetic freezing transition in a coo/permalloy bilayer revealed by transverse ac susceptibility. *Journal of Magnetism and Magnetic Materials*, 476:75–85, 2019.

[124] D. A. Garanin, E. M. Chudnovsky, and T. Proctor. Random field xy model in three dimensions. *Phys. Rev. B*, 88:224418, Dec 2013.

[125] Thomas C. Proctor, Dmitry A. Garanin, and Eugene M. Chudnovsky. Random fields, topology, and the imry-ma argument. *Phys. Rev. Lett.*, 112:097201, Mar 2014.

[126] Dmitry A Garanin and Eugene M Chudnovsky. Ordered vs. disordered states of the random-field model in three dimensions. *The European Physical Journal B*, 88(4):81, 2015.

[127] N. C. Koon. Calculations of exchange bias in thin films with ferromagnetic/antiferromagnetic interfaces. *Phys. Rev. Lett.*, 78:4865–4868, Jun 1997.

[128] T. C. Schulthess and W. H. Butler. Consequences of spin-flop coupling in exchange biased films. *Phys. Rev. Lett.*, 81:4516–4519, Nov 1998.

[129] M. D. Stiles and R. D. McMichael. Model for exchange bias in polycrystalline ferromagnet-antiferromagnet bilayers. *Phys. Rev. B*, 59:3722–3733, Feb 1999.

[130] Sergei Urazhdin, Phillip Tabor, and Weng-Lee Lim. Relationship between granularity of an antiferromagnet and exchange bias: Measurements of coo doped with pt. *Phys. Rev. B*, 78:052403, Aug 2008.

[131] Robert C. O'Handley. *Modern magnetic materials:principles and applications*. Wiley, New York, 2000.

[132] Mohamad H Hassoun. *Fundamentals of artificial neural networks*. MIT press, 1995.

[133] P. Dayan and L. Abbott. *Theoretical Neuroscience: Computational and Mathematical Modeling of Neural Systems*. MIT Press, Cambridge, MA, 2005.

[134] E. Kandel, J.H. Schwartz, T. Jessell, S. Siegelbaum, and A. Hudspeth. *Principles of Neural Science, Fifth edition*. McGraw-Hill, New York, 2012.

[135] LF Abbott and Wade G Regehr. Synaptic computation. *Nature*, 431(7010):796–803, 2004.

[136] Henry Markram, P Johannes Helm, and Bert Sakmann. Dendritic calcium transients evoked by single back-propagating action potentials in rat neocortical pyramidal neurons. *The Journal of physiology*, 485(1):1–20, 1995.

[137] Henry Markram, Joachim Lübke, Michael Frotscher, and Bert Sakmann. Regulation of synaptic efficacy by coincidence of postsynaptic aps and epsps. *Science*, 275(5297):213–215, 1997.

[138] Leon Chua. Memristor-the missing circuit element. *IEEE Transactions on circuit theory*, 18(5):507–519, 1971.

[139] Leon Chua. Resistance switching memories are memristors. *Applied Physics A*, 102(4):765–783, 2011.

[140] Zhongrui Wang, Saumil Joshi, Sergey E Savel'ev, Hao Jiang, Rivu Midya, Peng Lin, Miao Hu, Ning Ge, John Paul Strachan, Zhiyong Li, et al. Memristors with diffusive dynamics as synaptic emulators for neuromorphic computing. *Nature materials*, 16(1):101–108, 2017.

[141] Lei Wang, CiHui Yang, Jing Wen, Shan Gai, and YuanXiu Peng. Overview of emerging memristor families from resistive memristor to spintronic memristor. *Journal of Materials Science: Materials in Electronics*, 26(7):4618–4628, 2015.

[142] Qi Liu, Jun Sun, Hangbing Lv, Shibing Long, Kuibo Yin, Neng Wan, Yingtao Li, Litao Sun, and Ming Liu. Real-time observation on dynamic growth/dissolution of conductive filaments in oxide-electrolyte-based reram. *Advanced Materials*, 24(14):1844–1849, 2012.

[143] Stuart SP Parkin, Masamitsu Hayashi, and Luc Thomas. Magnetic domain-wall racetrack memory. *Science*, 320(5873):190–194, 2008.

[144] Jagan Singh Meena, Simon Min Sze, Umesh Chand, and Tseung-Yuen Tseng. Overview of emerging nonvolatile memory technologies. *Nanoscale research letters*, 9(1):526, 2014.

[145] John C Slonczewski. Current-driven excitation of magnetic multilayers. *Journal of Magnetism and Magnetic Materials*, 159(1):L1, 1996.

[146] William A Borders, Ahmed Z Pervaiz, Shunsuke Fukami, Kerem Y Camsari, Hideo Ohno, and Supriyo Datta. Integer factorization using stochastic magnetic tunnel junctions. *Nature*, 573(7774):390–393, 2019.

[147] Kyoung Jin Lee, Olivier Redon, and Bernard Dieny. Analytical investigation of spin-transfer dynamics using a perpendicular-to-plane polarizer. *Applied Physics Letters*, 86(2):022505, 2005.

[148] U Ebels, D Houssameddine, I Firastrau, D Gusakova, C Thirion, B Dieny, and LD Buda-Prejbeanu. Macrospin description of the perpendicular polarizer-planar free-layer spin-torque oscillator. *Physical Review B*, 78(2):024436, 2008.

[149] D Houssameddine, U Ebels, B Delaët, B Rodmacq, I Firastrau, F Ponthenier, M Brunet, C Thirion, J-P Michel, L Prejbeanu-Buda, et al. Spin-torque oscillator using a perpendicular polarizer and a planar free layer. *Nature materials*, 6(6):447–453, 2007.

[150] Weng Lee Lim, Andrew Higgins, and Sergei Urazhdin. Measurements of out-of-plane dynamics induced in magnetic nanopillars by spin transfer. *Physical Review B*, 80(10):104408, 2009.

[151] Shimeng Yu, Yi Wu, Rakesh Jeyasingh, Duygu Kuzum, and H-S Philip Wong. An electronic synapse device based on metal oxide resistive switching memory for neuromorphic computation. *IEEE Transactions on Electron Devices*, 58(8):2729–2737, 2011.

[152] Chi-Feng Pai, Minh-Hai Nguyen, Carina Belvin, Luis Henrique Vilela-Leão, DC Ralph, and RA Buhrman. Enhancement of perpendicular magnetic anisotropy and transmission of spin-hall-effect-induced spin currents by a hf spacer layer in w/hf/cofeb/mgo layer structures. *Applied Physics Letters*, 104(8):082407, 2014.

[153] Jairo Sinova, Sergio O Valenzuela, J Wunderlich, CH Back, and T Jungwirth. Spin hall effects. *Reviews of Modern Physics*, 87(4):1213, 2015.

[154] Tianyu Ma and Sergei Urazhdin. Spin glass transition in a thin-film nio/permalloy bilayer. *Physical Review B*, 97(5):054402, 2018.

[155] Pablo G Debenedetti and Frank H Stillinger. Supercooled liquids and the glass transition. *Nature*, 410(6825):259–267, 2001.

[156] Kurt Binder and A Peter Young. Spin glasses: Experimental facts, theoretical concepts, and open questions. *Reviews of Modern physics*, 58(4):801, 1986.

[157] Sergei Urazhdin, Weijie Li, and Lydia Novozhilova. Magnetic freezing transition in a coo/permalloy bilayer revealed by transverse ac susceptibility. *Journal of Magnetism and Magnetic Materials*, 476:75–85, 2019.

[158] Tianyu Ma, Xiang Cheng, Stefan Boettcher, Sergei Urazhdin, and Lydia Novozhilova. Thickness-dependent cooperative aging in polycrystalline films of antiferromagnet coo. *Physical Review B*, 94(2):024422, 2016.

[159] Sungho Kim, Chao Du, Patrick Sheridan, Wen Ma, ShinHyun Choi, and Wei D Lu. Experimental demonstration of a second-order memristor and its ability to biorealistically implement synaptic plasticity. *Nano letters*, 15(3):2203–2211, 2015.

[160] Zhong Qiang Wang, Hai Yang Xu, Xing Hua Li, Hao Yu, Yi Chun Liu, and Xiao Juan Zhu. Synaptic learning and memory functions achieved using oxygen ion migration/diffusion in an amorphous ingazno memristor. *Advanced Functional Materials*, 22(13):2759–2765, 2012.

[161] Harel Z. Shouval, Mark F. Bear, and Leon N Cooper. A unified model of nmda receptor-dependent bidirectional synaptic plasticity. *Proceedings of the National Academy of Sciences*, 99(16):10831–10836, 2002.

[162] Robert S Zucker. Calcium-and activity-dependent synaptic plasticity. *Current opinion in neurobiology*, 9(3):305–313, 1999.